Subarcsecond mid-infrared view of local active galactic nuclei: IV. The L- and M-band imaging Atlas

Isbell, J.W.; Burtscher, L.H.; Asmus, D.; Pott, J.U.; Couzy, P.; Stalevski, M.; ... ; Meisenheimer, K.

DRAFT VERSION OCTOBER 15, 2021
Typeset using LaTeX **twocolumn** style in AASTeX63

The Subarcsecond Mid-Infrared View of Local Active Galactic Nuclei. IV. The L- and M-band Imaging Atlas *

JACOB W. ISBELL [1], LEONARD BURTSCHER [2], DANIEL ASMUS [3,4], JÖRG-UWE POTT [1], PAUL COUZY [2], MARKO STALEVSKI [5,6], VIOLETA GÁMEZ ROSAS [2], AND KLAUS MEISENHEIMER [1]

[1] *Max-Planck-Insitut für Astronomie, Königstuhl 17, 69117 Heidelberg, Germany*
[2] *Sterrewacht Leiden, Niels Bohrweg 2, 2333 CA Leiden, The Netherlands*
[3] *School of Physics & Astronomy, University of Southampton, Southampton SO17 1BJ, UK*
[4] *Gymnasium Schwarzenbek, Buschkoppel 7, 21493 Schwarzenbek, Germany*
[5] *Astronomical Observatory, Volgina 7, 11060 Belgrade, Serbia*
[6] *Sterrenkundig Observatorium, Universiteit Gent, Krijgslaan 281-S9, Gent, 9000, Belgium*

(Received 18 September 2020; Accepted 14 January 2021)

Submitted to ApJ

ABSTRACT

We present the largest currently existing subarcsecond 3-5 μm atlas of 119 local ($z < 0.3$) active galactic nuclei (AGN). This atlas includes AGN of 5 subtypes: 22 are Seyfert 1; 5 are intermediate Seyferts; 46 are Seyfert 2; 26 are LINERs; and 20 are composites/starbursts. Each AGN was observed with VLT ISAAC in the *L*- and/or *M*-bands between 2000 and 2013. We detect at 3σ confidence 92 sources in the *L*-band and 83 sources in the *M*-band. We separate the flux into unresolved nuclear flux and resolved flux through two-Gaussian fitting. We report the nuclear flux, extended flux, apparent size, and position angle of each source, giving 3σ upper-limits for sources which are undetected. Using *WISE W1*- and *W2*-band photometry we derive relations predicting the nuclear *L* and *M* fluxes for Sy1 and Sy2 AGN based on their *W1*-*W2* color and *WISE* fluxes. Lastly, we compare the measured mid-infrared colors to those predicted by dusty torus models SKIRTOR, CLUMPY, CAT3D, and CAT3D-WIND, finding best agreement with the latter. We find that models including polar winds best reproduce the 3-5μm colors, indicating that winds are an important component of dusty torus models. We find that several AGN are bluer than models predict. We discuss several explanations for this and find that it is most plausibly stellar light contamination within the ISAAC *L*-band nuclear fluxes.

Keywords: Active Galactic Nuclei; AGN Host Galaxies; Infrared Galaxies; Infrared Photometry

1. INTRODUCTION

Understanding the dust in the vicinity of central supermassive black holes is instrumental to understanding how active galactic nuclei (AGN) are fed and powered. Large, obscuring dusty structures are held responsible for both funneling material toward the central engine, and for distinguishing between Type 1 and Type 2 AGN. In the Unified Model of AGN (Antonucci 1993; Urry & Padovani 1995; Netzer 2015), a central obscuring torus of dust is oriented such that the broad-line region of the AGN is directly visible (Type 1) or such that its observation is blocked by the torus (Type 2). The dust making up the sublimation ring (the dust closest to the AGN) is $\sim$ 1500K and is best observed in the near-infrared (NIR). The extended dust of the torus, on the other hand, is most readily observable in the thermal infrared (3-25 μm). Interferometric observations of AGN in the *H*-band (Weigelt et al. 2004), in the *K*-band (Wittkowski et al. 1998; Kishimoto et al. 2011; Gravity Collaboration et al. 2020), and in the *N*-band (e.g., López-Gonzaga et al. 2014; Tristram et al. 2014; Leftley et al. 2019) conclusively show hot ($\gtrsim$ 100K) dust in the vicinity of AGN (0.1pc - 100 pc) and provide strong evidence that the torus is clumpy. Clumpy media have moreover been argued in theory as necessary to prevent the destruction of dust grains by the surrounding hot gas (Krolik & Begelman 1988). Following Nenkova et al. (2002), a clumpy formalism has been used in many radiative transfer models of tori (e.g., Nenkova et al. 2008a; Schartmann et al. 2008; Hönig &

Corresponding author: J. W. Isbell
isbell@mpia.de

* This atlas makes use of European Southern Observatory (ESO) observing programs 65.P-0519, 67.B-0332, 70.B-0393, 71.B-0379, 71.B-0404, 072.B-0397, 074.B-0166, 085.B-0639, and 290.B-5133.

Kishimoto 2010; Stalevski et al. 2016), reproducing the spectral energy distributions (SEDs) and spectral features of the *N*-band particularly well. The 3-5μm bump (see e.g., Edelson & Malkan 1986; Kishimoto et al. 2011; Mor & Netzer 2012; Hönig et al. 2013), however, has remained difficult to properly model. Recent modeling suggests that this feature can be explained by the inclusion of a wind-driven outflow originating at the sublimation ring and propagating orthogonal to the disk (the disk+wind model; Hönig & Kishimoto 2017).

A large body of work using spectral energy distribution fits to local AGN (e.g., Ramos Almeida et al. 2009; Alonso-Herrero et al. 2011; Lira et al. 2013; García-González et al. 2016; García-Bernete et al. 2019; Martínez-Paredes et al. 2020) suggests that *L* and *M* observations at high sensitivity and angular resolution are required to study the physical properties of the 3-5 μm radiation bump. In fact, Lira et al. (2013) emphasize that spectral information at 5μm is necessary to properly constrain their SED fits. This mid-infrared (MIR) bump is expected to originate from dust radiating at intermediate spatial scales: outside of the accretion disk and the hot dust sublimation zone, but still inside of any extended polar dust emission further out. In the near future, those spatial scales will be directly resolved in detail in the *L*- and *M*-bands with the new instrument Very Large Telescope Interferometer (VLTI) MATISSE, which allows for simultaneous *L*-, *M*-, and *N*-band interferometric observations, but which also requires accurate estimates of nuclear target fluxes (Lopez et al. 2014).

A primary goal of this paper is to anticipate such future interferometric investigations of dusty AGN in the thermal infrared. We build on the SubArcSecond MidInfraRed Atlas of Local AGN (SASMIRALA; Asmus et al. 2014, hereafter A14), which presented an *N*- and *Q*-band imaging atlas of nearby AGN at subarcsecond resolution. In this work, we extend this atlas to the *L*- and *M*- bands for 119 nearby ($z < 0.3$) AGN, at a threefold increase in angular resolution compared to the *N*-band. We derive new spatial flux information at the seeing limit of the excellent Cerro Paranal site, and systematically explore how these fluxes relate to those measured in space with the *WISE W1* and *W2* bands. We then investigate how our measurements compare to the expectations derived from existing clumpy torus models.

The examination herein of *L*- and *M*-band fluxes in local AGN in a statistically relevant sample fulfills two goals: (*i*) direct observational evidence of the fact that *LM*-flux in excess of the classical hot torus radiation is a typical feature of nearby AGN; and furthermore, (*ii*) the presentation of an atlas and systematic characterization of the spatially resolved radiation properties to aide the sample selection for future, detailed interferometric imaging of that excess radiation to further understand its origin.

This paper is structured as follows: in §2 we present the sample, discussing its selection and observation. In §3 we discuss the data reduction and present the measured fluxes. In §4 we present and describe the *L* and *M* flux catalogs. In §5 we compare the MIR colors of our sample to those predicted from various clumpy torus models. In §6 we compare the *L* and *M* fluxes to those measured with *WISE* bands *W1* and *W2* respectively. We summarize and conclude the paper in §7. Additionally, we present the observing dates and conditions of each source in Appendix A, we further explain the flux calibration procedure in Appendix B, and we present cutouts of all 119 sources in Appendix C.

2. SAMPLE SELECTION AND OBSERVATIONS

The program from which the majority of sources were observed (ESO ID 290.B-5133(A); PI: Asmus) was a survey of AGN designed to complement the subarcsecond *N*– and *Q*–band AGN sample of A14 with 3 and 5μm images. Out of the original sample of 253 objects, 59 were observed in June and July 2013 with the ISAAC (Infrared Spectrometer and Array Camera; Moorwood et al. 1999) instrument on the Very Large Telescope (VLT) before it was decommissioned. Two stars were observed as flux calibrators during each night of the observing program: HD 106965 and HD 130163.

To supplement this sample, we searched the ESO archive for all *L*- and/or *M*-band ISAAC observations of local ($z < 0.3$) active galaxies contained in A14. We focus on 8m class telescopes in the Southern Hemisphere because we need to resolve as much of the central region as possible to properly separate the AGN itself from its host galaxy. We did not include archival observations taken with VLT NaCo because they include only 9 AGN which are not part of this sample, providing a small statistical gain for a large data reduction overhead. The ISAAC archival programs contain 60 of the individual targets and were proposed with a variety of goals, but they each contain nearby, optically-classified active galaxies observed in at least one of the *L*- and *M*-bands. We include 20 AGN observed from the archival programs which were not in the A14 sample. As these are archival data, the selection of calibration stars and the frequency of their observation is inconsistent. Whenever possible, we gather the calibration sources taken with the same instrumental setup on the same night as the AGN. Several sources were repeated in different programs.

Each AGN was observed with the L′-filter ($\lambda_c = 3.78\mu$m; hereafter referred to as the *L*-band), with the narrow M_{nb}-filter ($\lambda_c = 4.66\mu$m; hereafter referred to as the *M*-band), or with both. We list the ISAAC programs included in this work in Table 1, with the principle investigator and number of targets observed in each filter.

Prog. ID	PI	$N_{\mathrm{Obs.,L}}$	$N_{\mathrm{Obs.,M}}$
65.P-0519	Krabbe	15	38
67.B-0332	Marco	20	12
70.B-0393	Lira	40	38
71.B-0379	Lira	30	36
71.B-0404	Brooks	3	4
072.B-0397	Galliano	2	2
074.B-0166	Galliano	14	0
085.B-0639	Asmus	14	9
290.B-5133	Asmus	69	69

Table 1. ESO ISAAC observing programs entering into this analysis. The sum of the $N_{\mathrm{obs,X}}$ columns can be larger than 119 because several sources were observed in multiple epochs.

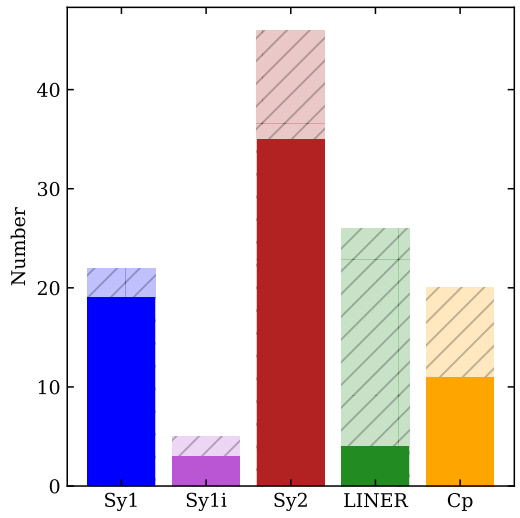

Figure 1. Histogram of the AGN optical classifications in this sample. Darkened regions indicate the number of sources detected with SNR≥2 with both the *L* and *M* filters.

The final sample includes 119 AGN of four broad classes, which we group based on their optical classifications as in A14:

- Seyfert 1 (Sy1): contains 1, 1.2, 1.5, 1n
- Intermediate Seyferts (Int. Sy): contains 1.8, 1.9, 1.5/2
- Seyfert 2 (Sy2): contains 1.8/2, 1.9/2, 2
- Low-ionization nuclear emission region galaxies (LINERs): contains L, L:, L/H, S3
- Composites/Starbursts (Cp): contains Cp, Cp:, H.

Optical classifications for each of the AGN come from Asmus et al. (2014) when available and are listed with the individual sources otherwise. As A14 compiled all optical classifications from the literature, there are multiple classifications for some objects (e.g., Sy 1.5/2). In Fig. 1 we show the distribution of AGN classes in the sample.

The final sample is then as follows: 21 are Seyfert 1; 5 are Intermediate Seyferts; 46 are Seyfert 2; 29 are LINERs; and 16 are so-called 'Cp' or Composites/Starbursts. Throughout the paper we color-code these types consistently as blue, purple, red, orange, and green, respectively. While there are 119 total AGN, not all of them were observed in both bands; instead there are 95 *L*-band observations and 107 *M*-band observations. The final sample thus includes 87 AGN with measurements in both bands. There are 20 AGN included in this work which were not part of the original A14 *N*- and *Q*-band sample. Their optical classifications (from the literature) are given in Table 2.

3. DATA REDUCTION

The data were reduced using the custom Python tool, VISIR and ISAAC Pipeline Environment* (VIPE; Asmus et al., in prep.). This pipeline applies the following algorithm:

1. Combine the data at each individual chop (and nod) position
2. Combine the individual exposures of each nodding cycle into pairs
3. Combine the nodding pairs into a single exposure, taking the jitter offsets into account
4. Find the brightest source beam in the total combined image
5. Extract the positive and negative beams from the different chop/nod positions by attempting to fit every beam in every nodding pair. If this is not possible, e.g., because the source is too faint, extract and combine beams at calculated chop/nod positions instead.

In comparison to the default pipeline, this method does a better job removing the sky background in especially the M-band, resulting in several novel $\geq 2\sigma$ NIR detections (e.g., of NGC 5278). In the exemplary case of the faintest *L*-band source we detected, 3C321, the signal-to-noise ratio of the detection increases from $\mathrm{SNR_{DRS}} = 1.01$ with the default pipeline to $\mathrm{SNR_{VIPE}} = 6.71$ with VIPE.

3.1. *Two-Gaussian Fitting*

Our primary interest is the unresolved, nuclear flux capturing the emission of the central engine. While for the nearest AGN, we may detect extended thermal dust emission, for more distant AGN it is likely the nuclear emission also contains significant contribution of stellar light from the host.

* https://github.com/danielasmus/vipe

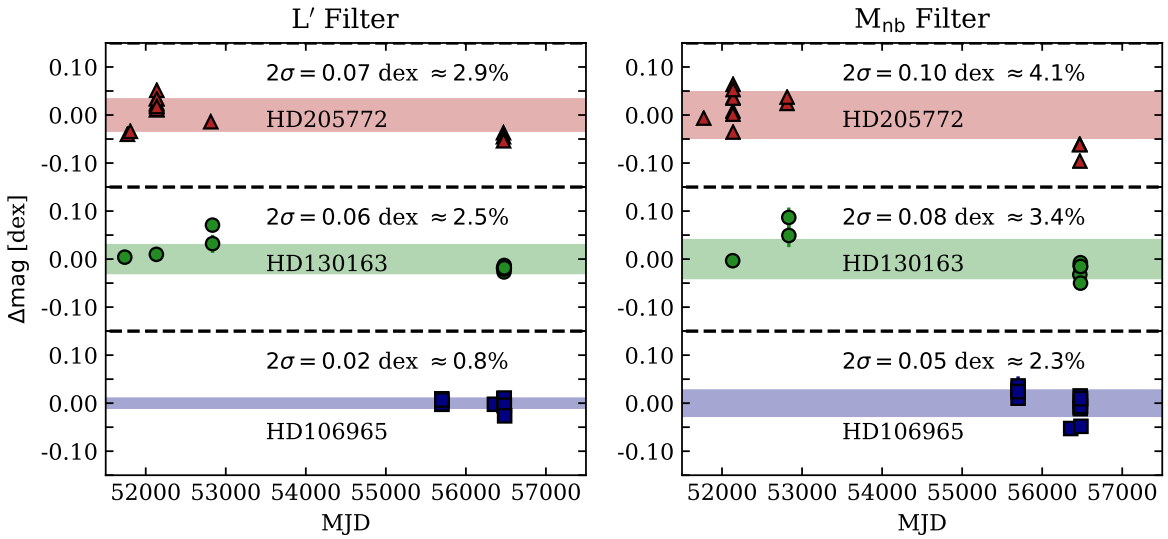

Figure 2. Stability of the 3 most often observed calibrators.

We aim to separate these two disparate components by fitting two elliptical Gaussians to each reduced image: one to represent the unresolved emission, and one to represent the extended emission. This method is quite commonly used in MIR interferometric data (e.g., Burtscher et al. 2013) to disentangle extended emission and the central engine.

As we were primarily interested in the unresolved component of each AGN, we needed to have an estimate of the point spread function (PSF) of each observation. For this, we did an initial round of fitting only the calibrators with single elliptical Gaussians. We found that the PSF size can vary by up to $\sim 10\%$ within an individual night. We can then set limits on the double-Gaussian fit; one component is set to have the major and minor axes ($\pm 10\%$) of the calibrator measured closest in time, while the second, larger component is required to have axes at least 10% larger than the central component. This accomplishes two things: 1) it effectively ignores the small amount of non-Gaussian central flux in the PSF, and 2) it wholly separates the extended and unresolved components, reducing the number of fit degeneracies and prevents the extended component from mistakenly fitting any PSF residuals. To reduce the number of total parameters, we assumed that the Gaussians are concentric.

Both the fitted Gaussians' parameters and the error estimates are obtained through Markov-Chain Monte Carlo likelihood maximization. We sample the parameter space using the package `emcee` (Foreman-Mackey et al. 2013). The log-probability function to be maximized is given by the typical formulation

$$p(\vec{\theta}, c|\vec{x}, y, \sigma) \propto p(\vec{\theta}) p(y|\vec{x}, \sigma, \vec{\theta}, c). \quad (1)$$

with measurements y at positions x, parameters $\vec{\theta}$ and error estimates σ scaled by some constant c. For maximum likelihood estimation, the log likelihood function for an arbitrary model $f(x, \vec{\theta})$ can be represented as

$$\ln p(y|\vec{x}, \sigma, \vec{\theta}, c) = -\frac{1}{2} \sum_n \left[\frac{(y_n - f(x_n, \vec{\theta}))^2}{s_n^2} + \ln(2\pi s_n^2) \right], \quad (2)$$

where $s_n^2 = \sigma_n^2 + c^2 f(x_n, \vec{\theta})^2$, and c represents the underestimation of the variance by some fractional amount. We estimate the best-fit value as the median of each marginalized posterior distribution and the 1σ errors from the values at 16$^{\text{th}}$ and 84$^{\text{th}}$ percentiles.

Finally, we define the nuclear Gaussian flux ($F_{\text{nuc.gauss}}$) as the integrated flux of the PSF-sized, so-called "unresolved" component, and the extended Gaussian flux ($F_{\text{ext.gauss}}$) as the integrated flux of the second, larger component. In the remainder of this paper, AGN "nuclear flux" refers to $F_{\text{nuc.gauss}}$, emphasizing that for sources closer than the median distance of 45.6 Mpc, at the average fitted calibrator size of ≈ 425 mas, this area covers the central ≤ 100 pc region of the AGN.

3.2. *Flux Calibration*

We flux-calibrate each AGN flux measurement ($F_{\text{nuc.gauss}}$, and $F_{\text{ext.gauss}}$) with the equivalent measurement of the calibration star observed which

1. was observed closest in time to the target, to minimize changes in atmospheric transmission and seeing

2. has *either* both L- and M-band flux in van der Bliek et al. (1996) or has spectral type $\in \{O, B, A, F\}$.

The spectral type selection is explained in detail in Appendix A, but in short we choose stars which have an effective temperature high enough such that the NIR color $L-M \approx 0$. This

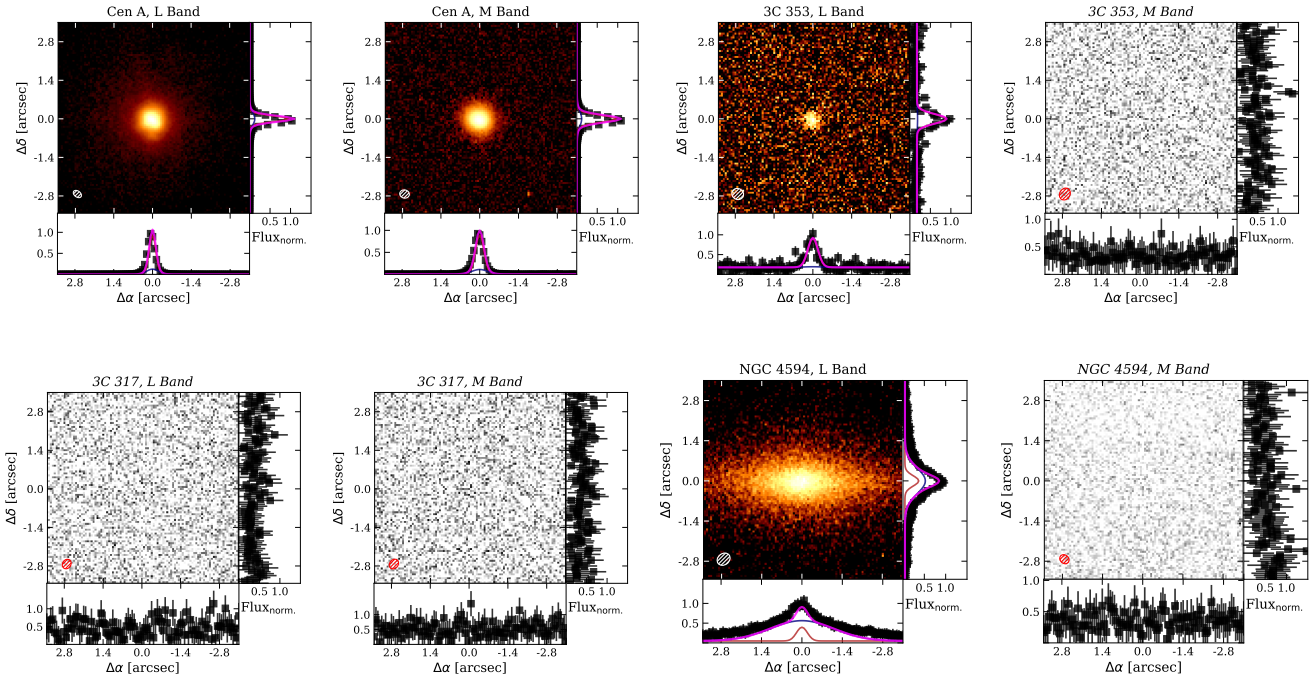

Figure 3. Cutouts for 4 representative sources: Cen A (top left) has clear detections in both bands; 3C353 (top right) is detected in only the *L*-band; 3C317 (bottom left) is detected in neither band; and NGC 4594 (bottom right) shows extended emission. Panels in greyscale (with titles in *italic*) are classified as non-detections, while those in color have $\mathrm{SNR}_{\mathrm{gauss}} \geq 3$ in either Gaussian component and are classified as detections. With each cutout we present 1-D slices across the center of the image in both the x- and y-directions. Data in these slices are shown in black, and the profiles of the fitted elliptical Gaussians are plotted in red (nuclear), blue (extended), and magenta (sum). All images are presented with log-scaling. The ellipse in the bottom left of each cutout represents the fitted FWHM of the PSF calibrator. The rest of the cutouts can be found in Appendix C.

means that even when the catalog is missing a measurement in one of the two bands, the other can be reliably estimated.

In the majority of cases, calibrators were observed within 6hr of the target but there are several nights in which no calibration source was observed. For these nights we estimate the long-term stability of the transfer function, by examining the flux stability of a few calibrators over many nights Three calibrators were observed often between 2000 and 2013: HD 130163, HD 106965, and HD 205772. These three calibrators allow us to examine the stability of the measured flux over time. In Fig. 2, we show the flux variations of these sources in the *L*- and M-bands. From this, we see that in the *L*-band the 2σ flux variation is less than 3% for all sources, and is as small as 0.8% for HD 106965. We also find that the M-band 2σ flux variations are slightly larger, but all smaller than 5%.

For the AGN which were calibrated with these "primary" stars, we add the 2σ flux variation directly to the flux uncertainty. For those calibrated with other stars, which were often observed only once, we cannot derive a similar 2σ value. Therefore, we add 3% and 5% for the *L*- and M-bands, respectively; values which are slightly larger than the mean standard deviations of the 3 "primary" calibrators. Finally, for those sources which have no calibration star observed in the same night, we use whichever of the three often-observed calibrators was observed closest in time and add the 3σ uncertainty to the flux error estimate. The 3σ uncertainties are roughly 4% and 6% in the *L*- and M-bands, respectively. The presented flux errors combine the fitting uncertainties from both the AGN and the calibration star as well as the flux variations of the calibrators.

When sources were observed on more than one epoch, we report only the "best" measurement. We typically select the epoch with smallest seeing. The sample is quite heterogeneous, however, so a simple definition of "best" is not satisfactory. We therefore report each source with its observation date, seeing, and any VIPE reduction flags in Appendix A. We opt not to use the mean of the measurements, as sources were often re-observed only because of poor weather or instrumental errors. There are, however, 16 total (13 in *L*, 9 in *M* with some overlap) sources which were observed multiple times under "good" conditions (i.e., no instrumental errors, no clouds, seeing $< 0.7''$). For these we find the measured fluxes to be quite stable: mean variations of 10.23% are found in the *L* band total fluxes; and mean variations of 15.63% are found in the *M*-band total fluxes. These values

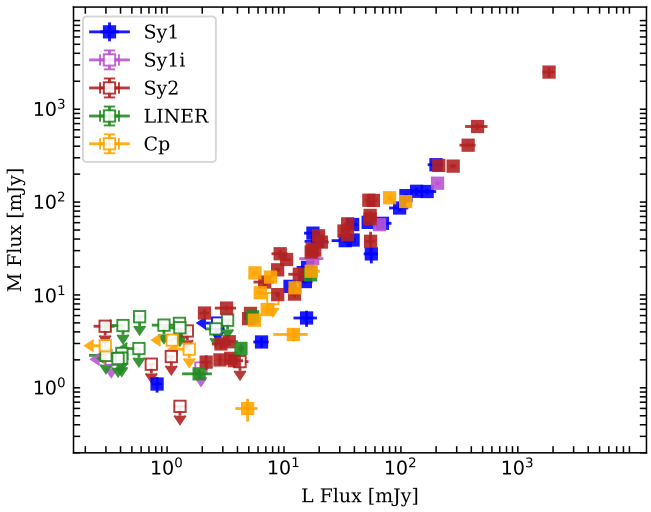

Figure 4. *L*-flux vs *M*-flux for all sources, with non-detections given as upper limits. The colors are the same as in Fig 1. Sources with measured fluxes exhibiting $SNR_{gauss} \geq 3$ in both bands are filled.

are comparable to the statistical errors derived from the calibrators and the fitting errors. In none of these sources do we see signs of significant brightening nor dimming over a 10 year span.

Additionally, we fit several targets with special conditions to extract double nuclei (e.g., Arp 220) or to locate the AGN at the center of a much brighter stellar disk (e.g., NGC 7552). We list all of these exceptional sources and the approach used to measure each in Appendix A.

3.2.1. *Extended Emission*

The ISAAC PSF is slightly non-Gaussian, so not all of the flux is recovered by a Gaussian fit, not even for the spatially unresolved calibrators. We find that on average $87 \pm 6\%$ of the flux measured in a 1" circular aperture is recovered in the *L*-band by such a Gaussian fit. Comparable point-source fitting in the *M*-band gives a similar value, $88 \pm 5\%$. This post-fit PSF residual does not ultimately affect nuclear flux calibration, however, because both the unresolved AGN flux component and the calibrators experience this in the same way.

However, the small difference between the true PSF and the Gaussian PSF approximation can be ignored when flux calibrating the extended source, since the PSF fine-structure is lost when convolving with a larger source. . We therefore calibrate only the Gaussian "unresolved" fluxes with the fitted fluxes of the calibrators, while we calibrate the extended fluxes with the Jy/cts conversion derived from circular aperture (1") measurements of the calibrators.

4. THE FLUX CATALOGS

We define a detection for at least one of the fitted flux components ($F_{nuc.gauss}$ or $F_{ext.gauss}$) as having a calibrated SNR ≥ 3. For non-detections we report only an upper limit of $3\sigma_{gauss}$. We report fluxes with SNR ≥ 2 only when the accompanying flux component has SNR ≥ 3; this most often affects the extended flux components.

4.1. *L- and M-band Nuclear Flux Table*

We present the measured nuclear *L*- and *M*-band fluxes and flux upper-limits of 119 active galaxies in Table 2. We include the *N*-band parent sample fluxes from Asmus et al. (2014) for reference. Our reported fluxes are the nuclear, unresolved component of our two-Gaussian fit. We present these fluxes separately, because the unresolved flux is most relevant for study of the AGN and interferometric follow-up observations (such as with VLTI/MATISSE).

We detect 92/95 sources in the *L*-band and 83/119 in the *M*-band. For all AGN with both *L*- and *M*-band measurements, there exist no cases where the AGN was detected in *M* but not in *L*. We show cutouts and their fitted Gaussians for a representative sample of sources in Fig. 3, and present all of the cutouts in Appendix C. Fig. 4 shows the measured *L*-band flux versus the *M*-band flux for all sources and/or their upper limits. Here we do not see any significant difference between the different AGN classes, but rather a tight linear relation between the two bands. We detect 19/20 Sy1, 4/5 Int. Sy, 36/46 Sy2, 5/29 LINERs, and 11/16 Cp in both bands.

Table 2. *L*- and *M*-band AGN Nuclear Flux Catalog

Target Name	RA (J2000)	Dec. (J2000)	AGN	*L* $Flux_{nuc}$	*M* $Flux_{nuc}$	*N* Flux
	[hh:mm:ss]	[dd:mm:ss]	Type	[mJy]	[mJy]	[mJy]
3C 273	12:29:06.70	+02:03:09.00	1	91.67 ± 7.34	77.81 ± 7.09	289.5 ± 51.1
3C 317	15:16:44.50	+07:01:18.00	2[1]	≤ 0.41	≤ 2.35	≤ 2.7
3C 321	15:31:43.50	+24:04:19.00	2	0.47 ± 0.07	≤ 4.63	≤ 50.30

Table 2 *continued*

Table 2 *(continued)*

Target Name	RA (J2000)	Dec. (J2000)	AGN	L Flux$_{nuc}$	M Flux$_{nuc}$	N Flux
	[hh:mm:ss]	[dd:mm:ss]	Type	[mJy]	[mJy]	[mJy]
3C 327	16:02:27.40	+01:57:56.00	1	0.92 ± 0.05	1.27 ± 0.20	70.8 ± 21.3
3C 353	17:20:28.20	-00:58:47.00	2[1]	1.26 ± 0.10	≤ 4.94	8.0 ± 2.3
3C 403	19:52:15.80	+02:30:24.00	2	5.00 ± 0.19	5.21 ± 0.43	94.2 ± 12.8
3C 424	20:48:12.00	+07:01:17.00	2	≤ 0.43	≤ 2.16	≤ 1.6
Arp 220	15:34:57.07	+23:30:14.74	L[2]	≤ 0.29	3.27 ± 0.18	-
Arp 220	15:34:57.07	+23:30:14.74	L[2]	13.02 ± 1.03	3.80 ± 0.48	-
Cen A	13:25:27.60	-43:01:08.99	2	261.69 ± 19.58	305.82 ± 18.28	1524.2 ± 152.4
CGCG381-051	23:48:43.90	+02:14:42.58	H	≤ 0.29	≤ 2.85	-
Circinus	14:13:09.90	-65:20:20.99	2	458.16 ± 39.18	676.41 ± 44.58	8326.9 ± 1049.2
ESO 103-35	18:38:20.30	-65:25:38.99	2	18.06 ± 1.97	40.67 ± 4.73	≤ 258.70
ESO 138-1	16:51:20.10	-59:14:05.00	2	50.90 ± 3.45	94.10 ± 4.80	759.9 ± 35.7
ESO 141-55	19:21:14.10	-58:40:13.00	1.2	46.85 ± 2.53	53.51 ± 4.11	148.7 ± 35.9
ESO 286-19	20:58:26.80	-42:39:00.01	Cp:	5.23 ± 0.33	16.33 ± 0.61	411.9 ± 41.2
ESO 323-32	12:53:20.30	-41:38:08.00	1.9	3.47 ± 0.12	2.04 ± 0.35	56.7 ± 7.4
ESO 323-77	13:06:26.10	-40:24:53.00	1.2	159.61 ± 9.27	119.07 ± 10.12	346.7 ± 79.4
ESO 506-27	12:38:54.60	-27:18:28.00	2	10.56 ± 0.87	23.32 ± 0.89	179.5 ± 17.9
ESO 511-30	14:19:22.40	-26:38:41.00	1	14.23 ± 0.57	13.65 ± 0.66	52.2 ± 5.2
Fairall 49	18:36:58.30	-59:24:09.00	2	52.25 ± 5.24	62.60 ± 7.74	≤ 213.20
Fairall 51	18:44:54.00	-62:21:53.00	1.5	36.03 ± 4.05	49.31 ± 5.57	391.4 ± 39.1
IC 3639	12:40:52.90	-36:45:21.00	2	15.39 ± 0.66	25.73 ± 1.39	386.1 ± 38.6
IC 4329A	13:49:19.30	-30:18:34.00	1.2	186.10 ± 7.07	231.37 ± 9.78	1157.7 ± 99.3
IC 4518W	14:57:41.20	-43:07:56.00	2	18.81 ± 1.41	35.44 ± 1.28	199.4 ± 31.7
IC 5063	20:52:02.30	-57:04:08.00	2	-	-	820.6 ± 57.8
IC 5179	22:16:09.04	-36:50:36.48	H[2]	-	≤ 2.19	-
IRAS 13349+2438	13:37:18.70	+24:23:03.00	1n	133.40 ± 11.12	120.27 ± 12.80	476.4 ± 63.3
IRASF00198-7926	00:21:54.21	-79:10:09.55	2	11.10 ± 1.93	25.74 ± 2.99	-
LEDA 170194	12:39:06.28	-16:10:47.09	2	3.09 ± 0.22	3.09 ± 0.25	42.4 ± 8.2
M87	12:30:49.40	+12:23:28.00	L	6.41 ± 0.24	2.69 ± 0.24	20.8 ± 2.9
MCG+2-4-25	01:20:02.66	+14:21:42.21	H[2]	-	7.34 ± 1.92	-
MCG-0-29-23	11:21:12.44	-02:59:04.40	2[4]	4.87 ± 0.17	6.00 ± 0.48	-
MCG-3-34-64	13:22:24.50	-16:43:42.00	2[1]	23.62 ± 1.67	39.81 ± 5.47	530.6 ± 65.4
MCG-6-30-15	13:35:53.70	-34:17:44.00	1.5	65.24 ± 4.07	56.78 ± 6.75	340.8 ± 62.9
Mrk 331	23:51:26.73	+20:35:12.51	Cp[1]	-	≤ 2.41	-
Mrk 463	13:56:02.97	+18:22:16.84	1.5[1]	68.53 ± 9.56	35.56 ± 7.95	-
Mrk 509	20:44:09.70	-10:43:25.00	1.5	108.46 ± 4.81	117.10 ± 5.40	256.4 ± 29.0
Mrk 841	15:04:01.20	+10:26:16.00	1.5	14.58 ± 1.48	23.03 ± 1.46	163.3 ± 47.6
Mrk 897	21:07:45.80	+03:52:40.00	Cp	7.42 ± 0.47	≤ 9.10	8.2 ± 2.7
NGC 63	00:17:45.51	+11:27:02.73	H[3]	-	0.71 ± 0.10	-
NGC 253	00:47:33.10	-25:17:18.00	Cp:	78.76 ± 2.68	121.74 ± 4.86	≤ 1038.5
NGC 424	01:11:27.60	-38:05:00.00	2	203.46 ± 7.91	225.63 ± 8.14	736.2 ± 222.9

Table 2 *continued*

Table 2 *(continued)*

Target Name	RA (J2000)	Dec. (J2000)	AGN	L Flux$_{nuc}$	M Flux$_{nuc}$	N Flux
	[hh:mm:ss]	[dd:mm:ss]	Type	[mJy]	[mJy]	[mJy]
NGC 520	01:24:34.65	+03:47:32.23	Cp[1]	-	≤ 2.32	-
NGC 660	01:43:02.25	+13:38:48.11	L[1]	-	≤ 2.09	-
NGC 986	02:33:34.13	-39:02:42.14	H[5]	-	4.72 ± 0.53	-
NGC 1008	02:37:57.11	+02:04:12.59	L/H[1]	≤ 0.05	≤ 2.94	-
NGC 1068	02:42:40.70	-00:00:48.00	2[1]	1940.88 ± 241.52	2687.53 ± 374.86	≤ 3567.20
NGC 1097	02:46:19.00	-30:16:30.00	L	5.55 ± 0.24	5.63 ± 0.51	16.8 ± 2.3
NGC 1125	02:51:40.48	-16:39:05.55	2[1]	3.51 ± 0.23	6.76 ± 0.46	-
NGC 1368	03:33:39.77	-05:05:24.29	2[1]	0.67 ± 0.06	-	-
NGC 1365	03:33:36.40	-36:08:25.00	1.8	196.43 ± 6.59	152.32 ± 6.74	360.7 ± 36.1
NGC 1386	03:36:46.20	-35:59:57.01	2	18.65 ± 0.98	29.31 ± 2.29	299.3 ± 62.3
NGC 1511	03:59:32.73	-67:38:00.00	H[2]	-	2.44 ± 0.17	-
NGC 1566	04:20:00.40	-54:56:16.00	1.5	10.55 ± 0.38	-	≤ 30.00
NGC 1614	04:33:59.90	-08:34:44.00	Cp:	-	7.13 ± 0.64	≤ 345.6
NGC 1667	04:48:37.10	-06:19:12.00	2	1.48 ± 0.08	-	≤ 2.60
NGC 1808	05:07:42.30	-37:30:47.01	Cp:	6.30 ± 0.51	10.46 ± 0.56	328.8 ± 34.2
NGC 3125	10:06:33.34	-29:56:06.31	L/H[2]	≤ 0.75	≤ 3.47	-
NGC 3281	10:31:52.10	-34:51:13.00	2	-	116.64 ± 5.26	486.4 ± 50.5
NGC 3660	11:23:32.30	-08:39:31.00	1.8[1]	2.99 ± 0.13	1.46 ± 0.15	≤ 15.30
NGC 4038/9	12:01:54.88	-18:53:05.95	1[1]	-	2.43 ± 0.26	-
NGC 4074	12:04:29.70	+20:18:58.00	2	12.53 ± 0.84	10.04 ± 0.72	68.3 ± 19.2
NGC 4235	12:17:09.90	+07:11:30.00	1.2	14.49 ± 0.97	5.71 ± 1.15	36.0 ± 6.5
NGC 4253	12:18:26.80	+29:48:45.39	1n[1]	23.99 ± 6.38	39.53 ± 2.28	-
NGC 4261	12:19:23.20	+05:49:31.00	L	0.64 ± 0.06	≤ 5.84	13.2 ± 3.0
NGC 4278	12:20:06.80	+29:16:51.00	L	≤ 0.57	≤ 2.66	2.5 ± 0.6
NGC 4303	12:21:54.90	+04:28:25.00	2	-	≤ 1.89	6.1 ± 0.8
NGC 4303	12:21:54.90	+04:28:25.00	2	1.65 ± 0.13	≤ 4.07	6.1 ± 0.8
NGC 4374	12:25:03.70	+12:53:13.00	2[1]	0.32 ± 0.04	≤ 2.21	≤ 8.0
NGC 4388	12:25:46.70	+12:39:44.00	2	34.11 ± 1.23	44.11 ± 2.10	187.8 ± 32.8
NGC 4418	12:26:54.60	-00:52:39.00	2	2.03 ± 0.20	6.26 ± 0.61	1426.8 ± 167.5
NGC 4438	12:27:45.60	+13:00:32.00	L/H	4.04 ± 0.26	2.20 ± 0.43	10.3 ± 2.8
NGC 4457	12:28:59.00	+03:34:14.00	L	3.01 ± 0.22	≤ 4.30	6.2 ± 1.7
NGC 4472	12:29:46.80	+08:00:02.00	2/L	≤ 0.41	≤ 2.09	≤ 8.6
NGC 4501	12:31:59.20	+14:25:13.00	2	1.50 ± 0.16	≤ 0.31	3.7 ± 0.5
NGC 4507	12:35:36.60	-39:54:33.01	2	59.67 ± 5.96	62.07 ± 12.71	622.8 ± 64.3
NGC 4579	12:37:43.50	+11:49:05.00	L	16.91 ± 0.66	14.99 ± 1.02	74.6 ± 4.5
NGC 4593	12:39:39.40	-05:20:39.00	1	32.31 ± 2.40	36.15 ± 2.54	227.4 ± 37.6
NGC 4594	12:39:59.40	-11:37:23.00	L	2.74 ± 0.32	≤ 4.42	4.4 ± 1.4
NGC 4746	12:51:55.40	+12:04:59.00	L/H	≤ 0.42	≤ 4.66	≤ 10.9
NGC 4785	12:53:27.30	-48:44:57.01	2	1.11 ± 0.08	≤ 2.17	≤ 17.4
NGC 4941	13:04:13.10	-05:33:06.00	2	4.54 ± 0.29	2.01 ± 0.34	76.1 ± 8.7

Table 2 *continued*

Table 2 *(continued)*

Target Name	RA (J2000)	Dec. (J2000)	AGN	L Flux$_{nuc}$	M Flux$_{nuc}$	N Flux
	[hh:mm:ss]	[dd:mm:ss]	Type	[mJy]	[mJy]	[mJy]
NGC 4945	13:05:27.50	-49:28:06.00	Cp	≤ 0.86	≤ 2.58	22.1 ± 6.9
NGC 5135	13:25:44.10	-29:50:01.00	2	12.63 ± 0.70	19.31 ± 2.75	132.0 ± 25.8
NGC 5252	13:38:16.00	+04:32:33.00	1.9	16.17 ± 1.20	25.19 ± 1.31	68.7 ± 6.9
NGC 5363	13:56:07.20	+05:15:17.00	L	0.98 ± 0.12	≤ 4.72	≤ 1.30
NGC 5427	14:03:26.10	-06:01:51.00	2	2.95 ± 0.10	2.09 ± 0.26	≤ 20.0
NGC 5506	14:13:14.90	-03:12:27.00	2	343.79 ± 12.95	359.44 ± 26.41	870.8 ± 65.6
NGC 5548	14:17:59.50	+25:08:12.00	1.5	3.29 ± 0.89	≤ 4.99	≤ 77.50
NGC 5643	14:32:40.70	-44:10:27.99	2	8.56 ± 0.45	14.11 ± 1.55	254.1 ± 68.7
NGC 5728	14:42:23.90	-17:15:11.00	1.9[1]	2.89 ± 0.22	2.76 ± 0.32	49.1 ± 7.1
NGC 5813	15:01:11.20	+01:42:07.00	L:	≤ 0.38	≤ 2.06	≤ 6.7
NGC 5953	15:34:32.40	+15:11:38.00	Cp	6.01 ± 0.63	≤ 2.29	≤ 29.5
NGC 5995	15:48:25.00	-13:45:28.00	1.9	60.09 ± 3.02	54.06 ± 4.99	332.4 ± 46.8
NGC 6000	15:49:49.69	-29:23:14.20	H[1]	-	2.72 ± 0.46	-
NGC 6221	16:52:46.33	-59:13:00.99	Cp	12.53 ± 0.47	11.30 ± 0.62	103.8 ± 21.1
NGC 6240N	16:52:58.92	+02:24:04.78	Cp	16.65 ± 0.56	18.47 ± 0.68	≤ 7.40
NGC 6300	17:16:59.50	-62:49:14.00	2	31.34 ± 1.73	49.80 ± 2.54	553.6 ± 162.1
NGC 6810	19:43:34.20	-58:39:20.00	Cp	7.10 ± 0.56	4.85 ± 0.51	44.4 ± 13.2
NGC 6814	19:42:40.60	-10:19:25.00	1.5	10.57 ± 0.40	12.04 ± 0.69	95.6 ± 23.5
NGC 6860	20:08:46.90	-61:06:01.00	1.5	35.24 ± 1.50	39.72 ± 2.47	206.1 ± 24.1
NGC 6890	20:18:18.10	-44:48:24.00	1.9[1]	8.12 ± 0.35	9.45 ± 0.66	116.6 ± 25.6
NGC 7130	21:48:19.50	-34:57:04.00	Cp	6.91 ± 0.30	14.39 ± 0.75	104.5 ± 21.1
NGC 7172	22:02:01.90	-31:52:11.00	2	48.96 ± 1.92	61.82 ± 3.30	185.0 ± 18.6
NGC 7213	22:09:18.16	-47:07:59.05	L/H[1]	-	≤ 3.39	-
NGC 7314	22:35:46.20	-26:03:02.00	2[1]	7.94 ± 0.43	18.47 ± 0.83	61.5 ± 11.8
NGC 7479	23:04:56.70	+12:19:22.00	2	12.84 ± 0.58	-	695.1 ± 95.1
NGC 7496	23:09:47.30	-43:25:41.00	Cp	6.59 ± 0.26	6.89 ± 0.64	169.5 ± 10.7
NGC 7552	23:16:10.80	-42:35:04.99	L/H	-	≤ 2.13	≤ 63.3
NGC 7582	23:18:23.50	-42:22:14.00	Cp	196.65 ± 7.49	91.64 ± 5.07	443.2 ± 79.3
NGC 7590	23:18:54.80	-42:14:21.00	2:	0.68 ± 0.05	≤ 1.79	≤ 10.6
PG 2130+099	21:32:27.80	+10:08:19.00	1.5	17.64 ± 3.15	44.28 ± 1.44	187.8 ± 20.9
PKS 1417-19	14:19:49.70	-19:28:25.00	1.5	6.20 ± 0.22	3.04 ± 0.40	≤ 10.10
PKS 1814-63	18:19:35.00	-63:45:48.00	2	3.71 ± 0.12	2.09 ± 0.19	27.7 ± 5.3
PKS 1932-46	19:35:56.60	-46:20:41.00	1.9	≤ 0.33	≤ 2.02	≤ 2.0
Superantennae S	19:31:21.47	-72:39:21.21	2	16.72 ± 0.81	26.91 ± 1.52	221.5 ± 62.8
UGC 2369 S	02:54:01.91	+14:58:17.54	Cp[2]	-	1.18 ± 0.11	-
Z 41-20	12:00:57.90	+06:48:23.00	2	2.87 ± 0.13	2.18 ± 0.34	29.3 ± 2.9

NOTE—Here Flux$_{nuc}$ indicates the flux from the fitted unresolved component. N-band fluxes and most AGN classifications come from Asmus et al. (2014) except where otherwise noted. [1] Véron-Cetty & Véron (2010); [2] Yuan et al. (2010); [3] Ho et al. (1997); [4] Hernán-Caballero & Hatziminaoglou (2011); [5] Hameed & Devereux (1999)

4.2. *L- and M-band Extended Flux Table*

We present the measured *extended* L- and M-band fluxes of the active galaxies in Table 3. In the table we also display the physical extent of the emission (from the fitted Gaussian

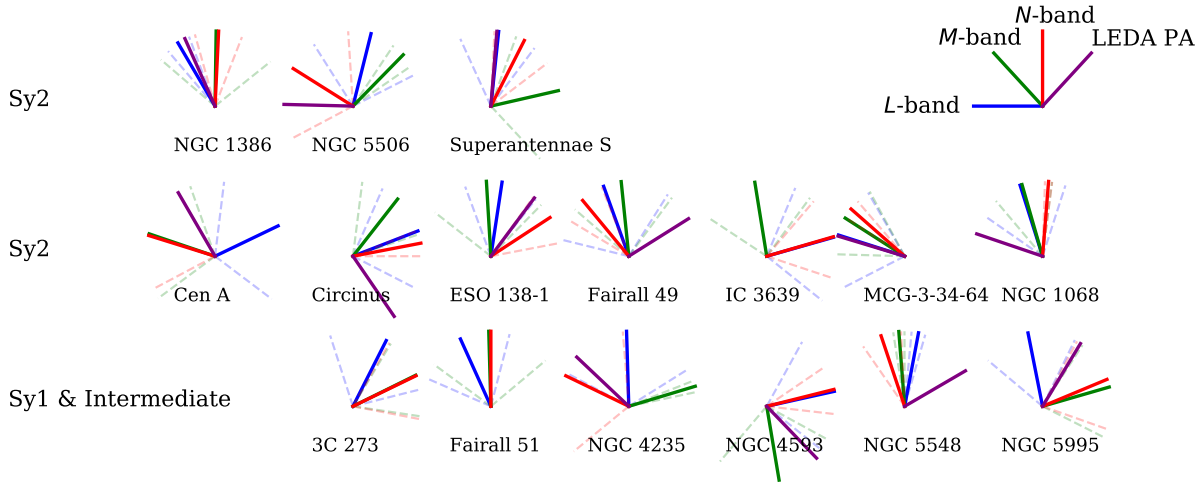

Figure 5. The measured infrared position angles (PAs) of sources with 1) SNR$\geq$ 2 extended emission in the *L*- and *M*-bands, and 2) a reported PA in Asmus et al. (2016). We include the optical position angle from HyperLEDA (Makarov et al. 2014) in purple for reference. The *L*, *M*, and *N* position angles are shown in blue, green, and red, respectively. 1σ errors are given as faint dashed lines in the same color as the reported angle.

axes), the minor/major axis ratio, and position angle (PA) of the source. We also include *N*-band extended emission PAs from Asmus et al. (2016) for reference. In the final column we give the unresolved flux to total flux ratio, $f_{\rm nuc}$.

In total we find significant resolved emission accompanying 73 and 42 AGN in the L' and *M* bands, respectively. In the L'-band, we find that 15 Sy1, 3 Syi, 32 Sy2, 14 LINERs, and 9 Cps exhibit extended emission. In the *M*-band 9 Sy1, 1 Syi, 14 Sy2, 6 LINERs, and 11 Cps had extended emission. Of the detected AGN, Sy2 were the most likely to show extended emission, with 32/36 resolved.

4.2.1. *A Note on Position Angles*

We note that the errors on the fitted PAs are quite large, and we caution the reader that even bright AGN showed large changes in fitted PA despite having consistent fitted flux and fitted FWHM values across epochs. NGC 1068, for example, exhibited PAs of -28 ± 38 deg and 19 ± 9.1 deg in the 2001 and 2004 epochs, respectively. The PSF PA varied by a similar amount. The unstable PSF of ISAAC leads us to suggest that the reader uses these PAs cautiously. We show *L*, *M*, and *N* PAs of the AGN with significant extended emission and PAs reported in Asmus et al. (2016) in Fig. 5. We include therein the optical PAs from HyperLEDA (Makarov et al. 2014) for comparison. In a few objects (3C 273, MCG-6-30-15, Circinus, Fairall 49, MGC-3-34-64, NGC 1068, and NGC 1386) there is relatively good agreement between the *L*, *M*, and *N* PAs. In only NGC 1386 and Superantennae S do the HyperLEDA angles match the *L* angle. The variation per source, however, is so great that we cannot draw any definite conclusions about the PA relations. AO-aided observations with ERIS or with ELT-METIS will be necessary to make progress in this line of inquiry.

Table 3. *L*-band and *M*-band AGN Extended Flux Catalog

Target Name	L Flux$_{\rm ext}$	$\Theta_{L,\rm ext}$	PA$_{L,\rm ext}$	r_L	M Flux$_{\rm ext}$	$\Theta_{M,\rm ext}$	PA$_{M,\rm ext}$	r_M	PA$_N$	$f_{\rm nuc}$
	[mJy]	[pc]	[deg]	$\equiv\theta/\Theta$	[mJy]	[pc]	[deg]	$\equiv\theta/\Theta$	[deg]	L (M)
3C 273	69.0 ± 28.9	3160.2 ± 419.9	28.8 ± 48.2	0.9	73.6 ± 22.4	3160.2 ± 292.4	65.5 ± 32.2	0.9	114.0 ± 34.0	0.57 (0.51)
3C 317	≤0.4	-	-	-	≤2.1	-	-	-	-	- (-)
3C 321	≤0.7	-	-	-	≤3.9	-	-	-	89.0 ± 0.0	- (-)
3C 327	≤0.4	-	-	-	≤2.8	-	-	-	97.0 ± 0.0	0.68 (-)
3C 353	≤0.7	-	-	-	≤4.7	-	-	-	-	0.66 (-)
3C 403	≤0.7	-	-	-	≤4.0	-	-	-	60.0 ± 0.0	0.88 (0.59)
3C 424	≤0.4	-	-	-	≤2.3	-	-	-	-	- (-)
Arp 220	≤1.5	-	-	-	≤2.4	-	-	-	-	- (0.74)
Arp 220	2.2 ± 0.3	7.4 ± 0.2	83.8 ± 1.6	0.6	≤2.4	-	-	-	-	0.85 (0.77)
Cen A	168.3 ± 80.0	11.6 ± 1.6	66.2 ± 58.6	0.9	182.1 ± 55.1	11.6 ± 1.1	5.0 ± 66.2	0.9	74.0 ± 42.0	0.61 (0.55)
CGCG381-051	≤0.3	-	-	-	≤2.3	-	-	-	-	- (-)
Circinus	≤1.7	-	-	-	591.1 ± 207.2	26.1 ± 3.2	40.4 ± 32.6	0.9	100.0 ± 10.0	1.00 (0.53)
ESO 103-35	22.9 ± 7.2	350.3 ± 29.2	-37.1 ± 42.1	0.9	≤5.3	-	-	-	109.0 ± 12.0	0.44 (0.91)
ESO 138-1	51.2 ± 16.2	180.6 ± 19.6	9.3 ± 31.2	0.9	39.3 ± 17.8	180.6 ± 24.9	-3.7 ± 50.6	0.9	121.0 ± 21.0	0.50 (0.70)
ESO 141-55	37.2 ± 9.1	1062.2 ± 92.8	91.3 ± 62.1	0.9	≤5.9	-	-	-	120.0 ± 47.0	0.56 (0.93)
ESO 286-19	≤0.6	-	-	-	≤4.3	-	-	-	-	0.90 (0.80)
ESO 323-32	3.3 ± 0.8	539.9 ± 54.6	-6.8 ± 9.0	0.7	≤4.1	-	-	-	76.0 ± 33.0	0.38 (-)
ESO 323-77	≤0.8	-	-	-	114.5 ± 39.3	221.1 ± 24.9	85.9 ± 21.2	0.9	95.0 ± 27.0	1.00 (0.51)
ESO 506-27	9.0 ± 4.0	658.8 ± 83.2	-1.3 ± 71.9	0.9	≤4.6	-	-	-	93.0 ± 8.0	0.54 (0.84)
ESO 511-30	≤0.6	-	-	-	≤4.4	-	-	-	82.0 ± 3.0	0.96 (0.77)
Fairall 49	75.8 ± 21.5	587.7 ± 46.2	-21.4 ± 55.9	0.9	87.7 ± 27.7	587.7 ± 47.0	-6.3 ± 45.1	0.9	42.0 ± 19.0	0.41 (0.41)
Fairall 51	53.5 ± 15.9	399.6 ± 33.1	-26.2 ± 42.0	0.9	≤7.4	-	-	-	180.0 ± 0.0	0.40 (0.90)
IC 3639	11.0 ± 2.6	253.0 ± 24.9	75.4 ± 50.9	0.9	9.0 ± 4.3	253.0 ± 31.2	-9.9 ± 48.8	0.9	105.0 ± 32.0	0.58 (0.74)
IC 4329A	60.4 ± 28.6	573.3 ± 92.0	4.0 ± 66.6	0.8	≤9.1	-	-	-	65.0 ± 9.0	0.76 (0.98)
IC 4518W	10.9 ± 4.5	440.9 ± 54.9	78.4 ± 47.5	0.9	≤4.6	-	-	-	-	0.63 (0.89)
IC 5063	-	-	-	-	-	-	-	-	108.0 ± 5.0	- (-)
IC 5179	-	-	-	-	≤2.0	-	-	-	-	- (-)
IRAS 13349+2438	≤0.8	-	-	-	110.7 ± 45.1	2641.6 ± 275.1	59.6 ± 30.7	0.9	16.0 ± 19.0	1.00 (0.52)
IRASF00198-7926	22.9 ± 5.8	4.8 ± 0.4	24.0 ± 9.6	0.8	25.1 ± 11.5	4.8 ± 0.5	15.0 ± 32.1	0.9	-	0.33 (0.50)
LEDA 170194	1.6 ± 0.8	642.1 ± 89.5	2.5 ± 33.2	0.8	≤2.7	-	-	-	44.0 ± 18.0	0.66 (0.54)
M87	3.2 ± 1.4	61.3 ± 8.4	72.1 ± 47.7	0.9	≤4.5	-	-	-	-	0.56 (-)
MCG+2-4-25	-	-	-	-	≤2.0	-	-	-	-	- (0.80)

Table 3 *continued*

Table 3 *(continued)*

Target Name	L Flux$_{\rm ext}$ [mJy]	$\Theta_{L,\rm ext}$ [pc]	PA$_{L,\rm ext}$ [deg]	r_L $\equiv\theta/\Theta$	M Flux$_{\rm ext}$ [mJy]	$\Theta_{M,\rm ext}$ [pc]	PA$_{M,\rm ext}$ [deg]	r_M $\equiv\theta/\Theta$	PA$_N$ [deg]	$f_{\rm nuc}$ L (M)
MCG-0-29-23	13.5 ± 1.4	10.5 ± 0.6	133.6 ± 3.7	0.6	≤ 2.0	-	-	-	-	0.27 (0.77)
MCG-3-34-64	33.9 ± 8.9	442.9 ± 33.4	106.4 ± 41.6	0.9	56.0 ± 22.3	442.9 ± 45.0	120.5 ± 29.0	0.9	51.0 ± 8.0	0.41 (0.43)
MCG-6-30-15	38.0 ± 18.4	115.4 ± 18.1	100.0 ± 44.3	0.9	53.8 ± 25.9	115.4 ± 16.2	83.4 ± 13.1	0.8	106.0 ± 13.0	0.63 (0.52)
Mrk 509	≤ 0.6	-	-	-	≤ 4.3	-	-	-	107.0 ± 24.0	0.99 (0.97)
Mrk 841	9.9 ± 4.4	598.7 ± 71.2	11.0 ± 53.8	0.9	≤ 3.8	-	-	-	155.0 ± 31.0	0.60 (0.87)
Mrk 897	3.5 ± 1.6	677.7 ± 94.8	-7.3 ± 52.1	0.9	-	-	-	-	-	0.68 (-)
Mrk 331	-	-	-	-	≤ 2.1	-	-	-	-	- (-)
Mrk 463	101.4 ± 43.8	5.5 ± 0.7	39.0 ± 27.7	0.9	126.4 ± 27.9	5.5 ± 0.4	47.5 ± 12.5	0.9	-	0.41 (0.21)
NGC 6300	≤ 0.7	-	-	-	≤ 6.4	-	-	-	112.0 ± 4.0	- (-)
NGC 253	82.9 ± 10.7	42.8 ± 3.7	130.4 ± 3.0	0.4	88.9 ± 27.8	42.8 ± 4.6	134.0 ± 5.0	0.4	-	0.49 (0.58)
NGC 424	≤ 0.6	-	-	-	81.0 ± 33.4	439.4 ± 72.7	-0.2 ± 58.0	0.8	80.0 ± 0.0	1.00 (0.74)
NGC 520	-	-	-	-	≤ 1.9	-	-	-	-	- (-)
NGC 660	-	-	-	-	≤ 1.8	-	-	-	-	- (-)
NGC 986	-	-	-	-	≤ 4.0	-	-	-	-	- (-)
NGC 1008	≤ 0.2	-	-	-	≤ 3.2	-	-	-	-	- (-)
NGC 1068	1818.3 ± 874.9	83.1 ± 9.4	-19.0 ± 38.4	0.9	4204.3 ± 1488.6	83.1 ± 8.0	-17.4 ± 25.2	0.9	175.0 ± 3.0	0.53 (0.40)
NGC 1097	8.3 ± 1.3	133.2 ± 9.1	-0.4 ± 68.5	0.9	≤ 1.9	-	-	-	-	0.40 (0.75)
NGC 1125	6.0 ± 1.3	5.3 ± 0.4	130.5 ± 10.0	0.8	≤ 1.6	-	-	-	-	0.37 (0.82)
NGC 1368	4.4 ± 0.3	8.1 ± 0.3	104.9 ± 8.7	0.9	-	-	-	-	-	0.13 (-)
NGC 1365	48.8 ± 24.0	173.4 ± 40.9	2.7 ± 58.1	0.7	≤ 1.7	-	-	-	82.0 ± 25.0	0.80 (0.99)
NGC 1386	20.9 ± 5.0	114.2 ± 8.9	-32.6 ± 10.4	0.8	18.9 ± 8.3	114.2 ± 14.1	0.9 ± 52.7	0.9	177.0 ± 20.0	0.47 (0.61)
NGC 1511	-	-	-	-	≤ 1.5	-	-	-	-	- (0.63)
NGC 1566	11.1 ± 1.8	118.2 ± 9.3	1.5 ± 32.8	0.9	-	-	-	-	157.0 ± 37.0	0.49 (-)
NGC 1614	-	-	-	-	15.6 ± 2.1	-	72.5 ± 9.6	0.8	-	- (0.31)
NGC 1667	2.0 ± 0.4	597.4 ± 51.5	11.4 ± 3.7	0.5	-	-	-	-	54.0 ± 0.0	0.42 (-)
NGC 1808	15.7 ± 2.2	72.6 ± 3.6	29.8 ± 5.2	0.7	9.0 ± 2.1	72.6 ± 7.4	42.6 ± 13.9	0.8	-	0.29 (0.54)
NGC 3125	≤ 0.6	-	-	-	≤ 3.1	-	-	-	-	- (-)
NGC 3281	-	-	-	-	≤ 5.0	-	-	-	176.0 ± 16.0	- (0.96)
NGC 3660	1.8 ± 0.3	324.6 ± 23.7	-8.8 ± 56.8	0.9	≤ 1.4	-	-	-	-	0.49 (-)
NGC 4038/9	-	-	-	-	≤ 1.9	-	-	-	-	- (-)
NGC 4074	≤ 0.7	-	-	-	≤ 4.4	-	-	-	189.0 ± 0.0	0.95 (0.71)
NGC 4235	11.9 ± 4.0	177.3 ± 18.8	-1.9 ± 61.9	0.9	8.7 ± 2.0	177.3 ± 5.8	74.5 ± 4.5	0.5	66.0 ± 61.0	0.55 (0.39)
NGC 4253	33.1 ± 14.4	6.5 ± 0.7	-18.0 ± 29.9	0.9	≤ 4.6	-	-	-	-	0.41 (0.90)
NGC 4261	≤ 0.6	-	-	-	≤ 5.2	-	-	-	-	- (-)

Table 3 *continued*

Table 3 *(continued)*

Target Name	L Flux$_{\rm ext}$	$\Theta_{L,\rm ext}$	PA$_{L,\rm ext}$	r_L	M Flux$_{\rm ext}$	$\Theta_{M,\rm ext}$	PA$_{M,\rm ext}$	r_M	PA$_N$	$f_{\rm nuc}$
	[mJy]	[pc]	[deg]	$\equiv\theta/\Theta$	[mJy]	[pc]	[deg]	$\equiv\theta/\Theta$	[deg]	L (M)
NGC 4278	≤ 0.5	-	-	-	≤ 2.5	-	-	-	-	- (-)
NGC 4303	-	-	-	-	≤ 2.1	-	-	-	-	- (-)
NGC 4303	5.9 ± 0.7	119.5 ± 5.4	-10.4 ± 26.3	0.9	≤ 4.1	-	-	-	-	0.22 (-)
NGC 4374	≤ 0.4	-	-	-	≤ 2.0	-	-	-	-	- (-)
NGC 4388	≤ 0.4	-	-	-	≤ 2.6	-	-	-	28.0 ± 34.0	0.99 (0.95)
NGC 4418	1.7 ± 0.8	207.9 ± 27.8	99.9 ± 9.2	0.7	≤ 4.5	-	-	-	-	0.55 (0.60)
NGC 4438	12.6 ± 1.4	133.5 ± 6.0	-23.2 ± 3.0	0.6	≤ 5.1	-	-	-	-	0.24 (-)
NGC 4457	15.5 ± 1.2	139.6 ± 4.8	112.6 ± 6.7	0.8	≤ 3.7	-	-	-	-	0.16 (-)
NGC 4472	≤ 0.4	-	-	-	≤ 1.9	-	-	-	-	- (-)
NGC 4501	13.7 ± 1.2	144.1 ± 4.9	43.1 ± 5.1	0.8	≤ 2.4	-	-	-	153.0 ± 0.0	0.10 (-)
NGC 4507	51.5 ± 22.9	259.3 ± 35.5	78.1 ± 45.6	0.9	≤ 6.4	-	-	-	111.0 ± 22.0	0.54 (0.92)
NGC 4579	17.1 ± 4.3	82.5 ± 9.4	85.8 ± 48.6	0.9	7.2 ± 3.3	82.5 ± 13.6	87.3 ± 42.7	0.8	-	0.50 (0.67)
NGC 4593	22.8 ± 11.1	155.6 ± 22.4	78.5 ± 47.6	0.9	25.6 ± 7.0	155.6 ± 14.9	-10.3 ± 53.0	0.9	103.0 ± 19.0	0.58 (0.58)
NGC 4594	38.9 ± 2.0	120.0 ± 3.0	90.8 ± 0.9	0.4	≤ 3.8	-	-	-	-	0.07 (-)
NGC 4746	≤ 0.4	-	-	-	-	-	-	-	-	- (-)
NGC 4785	4.0 ± 0.5	436.7 ± 23.5	71.9 ± 6.7	0.8	≤ 2.0	-	-	-	-	0.22 (-)
NGC 4941	4.2 ± 1.4	115.7 ± 13.3	17.2 ± 32.7	0.9	≤ 3.4	-	-	-	116.0 ± 11.0	0.52 (-)
NGC 4945	54.9 ± 3.5	42.6 ± 0.9	133.4 ± 1.0	0.4	≤ 2.3	-	-	-	-	0.04 (-)
NGC 5135	8.0 ± 3.3	202.1 ± 28.0	80.4 ± 46.0	0.9	≤ 3.4	-	-	-	66.0 ± 48.0	0.61 (0.85)
NGC 5252	13.3 ± 4.8	344.6 ± 38.6	69.0 ± 50.8	0.9	≤ 4.8	-	-	-	144.0 ± 24.0	0.55 (0.85)
NGC 5363	8.4 ± 0.7	149.6 ± 5.9	46.1 ± 6.0	0.8	≤ 4.2	-	-	-	-	0.10 (-)
NGC 5427	≤ 0.3	-	-	-	≤ 2.1	-	-	-	-	0.90 (-)
NGC 5506	123.8 ± 49.6	165.1 ± 30.0	15.2 ± 49.8	0.8	152.4 ± 47.4	165.1 ± 8.0	46.8 ± 10.8	0.7	60.0 ± 56.0	0.73 (0.70)
NGC 5548	59.0 ± 3.8	410.8 ± 12.3	11.6 ± 5.8	0.9	≤ 5.0	-	-	-	200.0 ± 17.0	0.05 (-)
NGC 5643	10.9 ± 2.3	91.2 ± 8.4	100.3 ± 49.2	0.9	≤ 3.6	-	-	-	52.0 ± 17.0	0.44 (0.82)
NGC 5728	3.0 ± 1.1	358.3 ± 41.7	97.7 ± 29.8	0.9	≤ 4.5	-	-	-	98.0 ± 25.0	0.49 (-)
NGC 5813	≤ 0.3	-	-	-	≤ 1.9	-	-	-	-	- (-)
NGC 5953	≤ 0.3	-	-	-	≤ 2.0	-	-	-	-	0.96 (-)
NGC 5995	44.7 ± 13.4	613.3 ± 69.7	-12.2 ± 40.1	0.9	53.7 ± 19.0	613.3 ± 69.4	75.1 ± 39.8	0.9	111.0 ± 39.0	0.57 (0.50)
NGC 6000	-	-	-	-	≤ 2.1	-	-	-	-	- (-)
NGC 6221	12.8 ± 2.9	103.5 ± 9.0	-12.5 ± 7.5	0.6	≤ 3.8	-	-	-	-	0.49 (0.75)
NGC 6240N	12.4 ± 1.5	1510.1 ± 52.4	-12.3 ± 3.3	0.5	≤ 1.8	-	-	-	-	0.57 (0.91)
NGC 63	-	-	-	-	1.2 ± 0.5	-	56.4 ± 12.4	0.6	-	- (0.98)
NGC 6810	28.4 ± 2.5	199.4 ± 7.1	10.7 ± 2.4	0.6	10.0 ± 2.0	199.4 ± 12.3	9.3 ± 3.0	0.5	-	0.20 (0.33)

Table 3 *continued*

Table 3 *(continued)*

Target Name	L Flux$_{\rm ext}$	$\Theta_{L,\rm ext}$	PA$_{L,\rm ext}$	r_L	M Flux$_{\rm ext}$	$\Theta_{M,\rm ext}$	PA$_{M,\rm ext}$	r_M	PA$_N$	$f_{\rm nuc}$
	[mJy]	[pc]	[deg]	$\equiv\theta/\Theta$	[mJy]	[pc]	[deg]	$\equiv\theta/\Theta$	[deg]	L (M)
NGC 6814	5.4 ± 1.5	108.3 ± 13.0	84.2 ± 59.7	0.9	≤ 3.6	-	-	-	97.0 ± 10.0	0.66 (0.78)
NGC 6860	15.0 ± 5.1	448.9 ± 56.5	86.1 ± 60.4	0.9	≤ 4.9	-	-	-	53.0 ± 49.0	0.70 (0.91)
NGC 6890	6.9 ± 1.5	164.6 ± 15.8	-16.3 ± 39.3	0.9	≤ 1.3	-	-	-	102.0 ± 0.0	0.54 (0.88)
NGC 7130	7.7 ± 1.2	406.2 ± 28.3	9.7 ± 49.4	0.9	≤ 2.8	-	-	-	-	0.47 (0.89)
NGC 7172	31.5 ± 7.6	215.5 ± 23.0	16.7 ± 50.5	0.9	≤ 3.4	-	-	-	86.0 ± 10.0	0.61 (0.95)
NGC 7213	-	-	-	-	≤ 3.1	-	-	-	-	- (-)
NGC 7314	6.8 ± 1.5	73.4 ± 6.7	91.4 ± 25.7	0.9	≤ 2.5	-	-	-	87.0 ± 43.0	0.54 (0.89)
NGC 7479	10.0 ± 2.5	168.9 ± 17.5	-3.4 ± 37.0	0.9	-	-	-	-	82.0 ± 0.0	0.56 (-)
NGC 7496	4.7 ± 1.2	133.4 ± 13.9	16.6 ± 48.1	0.9	≤ 2.3	-	-	-	-	0.58 (0.77)
NGC 7552	-	-	-	-	≤ 2.3	-	-	-	-	- (-)
NGC 7582	60.2 ± 26.9	246.0 ± 58.0	19.1 ± 42.0	0.7	83.2 ± 22.0	246.0 ± 24.2	100.7 ± 56.8	0.9	-	0.77 (0.52)
NGC 7590	4.0 ± 0.3	226.6 ± 8.2	-29.0 ± 3.7	0.7	≤ 1.7	-	-	-	-	0.14 (-)
PG 2130+099	20.7 ± 9.5	1525.4 ± 180.2	67.8 ± 31.8	0.9	≤ 4.5	-	-	-	158.0 ± 27.0	0.45 (0.92)
PKS 1417-19	≤ 0.7	-	-	-	≤ 4.2	-	-	-	98.0 ± 0.0	0.91 (-)
PKS 1814-63	≤ 0.4	-	-	-	≤ 2.1	-	-	-	25.0 ± 0.0	0.90 (-)
PKS 1932-46	≤ 0.3	-	-	-	≤ 2.1	-	-	-	-	- (-)
Superantennae S	9.4 ± 2.8	1553.8 ± 189.1	6.5 ± 32.8	0.8	17.4 ± 4.9	1553.8 ± 132.7	78.1 ± 56.5	0.9	151.0 ± 26.0	0.64 (0.61)
UGC 2369 S	-	-	-	-	≤ 1.9	-	-	-	-	- (-)
Z 41-20	≤ 0.7	-	-	-	≤ 4.1	-	-	-	172.0 ± 36.0	0.76 (-)

NOTE—Here Flux$_{\rm ext}$ indicates the flux from the fitted resolved emission, and we only include Θ and PA for those sources with $> 2\sigma$ detections. N-band PAs come from Asmus et al. (2016). Here $r_X \equiv \theta_{\rm FWHM,X}/\Theta_{\rm FWHM,X}$.

5. COMPARISON TO DUST EMISSION MODELS

We compare our detected AGN MIR colors to those predicted by various dusty torus models. The SKIRTOR models (Stalevski et al. 2016) are heterogeneous, consisting of high-density clumps and low-density interclump media. The CAT3D models (Hönig & Kishimoto 2010) and the CLUMPY models (Nenkova et al. 2008b) resemble classical clumpy tori made up of spherical clouds, while CAT3D-WIND (Hönig & Kishimoto 2017) includes an additional hollow cone in the polar region, representing a dusty wind driven by radiation pressure. Numerous previous works have performed SED fitting to test various torus models (e.g., Ramos Almeida et al. 2009; Alonso-Herrero et al. 2011; Lira et al. 2013), and they have emphasized the importance of the 5μm flux. We therefore focus on the NIR, utilizing the new *L*- and *M*-band measurements from this work, presenting a spectral slope plot similar to that in e.g., Hönig & Kishimoto (2017).

In addition, we include in comparison a new, unpublished model library consisting of a flared disk and a polar wind[†]. We discuss the model only briefly here, and only in comparison to SKIRTOR (Stalevski et al. 2016). The disk component is defined by its angular width and optical depth and is similar to that in SKIRTOR, but with dust distributed smoothly. The polar wind takes the shape of a hollow cone parametrized by half-opening angle and radial extent. The dust composition is the same as in SKIRTOR (53 % silicates and 47 % graphite), and with the same power-law grain size distribution (Mathis et al. 1977), but with larger grains (between 0.1 and 1 μm), as suggested by flat extinction curves and silicate feature profiles (Gaskell et al. 2004; Shao et al. 2017; Xie et al. 2017). For the hollow cone, we calculated an additional set of models with only graphite grains: if dust in the wind is driven away from the sublimation zone, it might be expected to be silicate-poor. This is a preliminary model library with limited parameter space: the current number of SEDs is an order of magnitude smaller than its precursor, SKIRTOR. However, it is well-motivated by the model of the resolved mid-IR images of Circinus AGN (Stalevski et al. 2017, 2019). Even though this model library is to be developed further and tested against larger datasets, it is useful for our purpose here, since it represents an extension of the SKIRTOR models, thus allowing us to isolate the effect of polar winds on the flux ratios. While at this stage any results obtained with this model are to be taken with caution, it is indicative that, as it will be shown below, even though it is much more limited in terms of parameters and number of SEDs, it provides a significantly better match to the observed color space than its precursor. Also, unlike any other included model library, the color space covered by this model does not extend significantly beyond the observed colors.

For each model SED produced by these setups, we extract the *L*-, *M*-, and *N*-band fluxes. We then compare the flux ratios F_L/F_M and F_M/F_N to those from the *L*- and *M*-band fluxes from this sample and the *N*-band fluxes from Asmus et al. (2014), shown in Fig 6. We compare the models using the χ^2 value, measured from each galaxy to the SED in each model that it matches most closely. We primarily consider Seyfert types 1, intermediate, and 2 in this analysis, as torus orientation aims to explain their differences in AGN Unification. We include the other AGN (e.g., LINERs and Cp) as they may have dusty tori but their mid-infrared emission might not be dominated by them.

Our observations favor torus+wind models such at CAT3D-WIND and the new SKIRTOR+wind. Specifically, CAT3D-WIND has the lowest χ^2 value, $\chi^2_{\rm CAT3D-WIND}$ = 51.68, which is a very sharp improvement from the base CAT3D $\chi^2_{\rm CAT3D}$ = 121.81. Similarly, the agreement with SKIRTOR is greatly improved with the inclusion of the polar wind: $\chi^2_{\rm SKIRTOR}$ = 204.58 $\rightarrow$ $\chi^2_{\rm SKIRTOR+wind}$ = 73.89. CLUMPY exhibits a similar agreement, $\chi^2_{\rm CLUMPY}$ = 65.88, notably *without* the inclusion of winds. The χ^2 values serve here primarily as a means for simple comparison, as the various torus models have vastly different parameter spaces and numbers of SEDs. Our results nonetheless agree with González-Martín et al. (2019) who found that CAT3D-WIND best matched their Swift/BAT-selected sample, with CLUMPY performing second-best. Moreover, similar to González-Martín et al. (2019), we find that the AGN colors are confined to a much smaller region of the parameter space than the torus SEDs. With our simple color-color comparisons, however, we cannot distinguish whether these regions have unphysical parameters or whether the discrepancy is driven by selection effects.

We find 13 of our Seyfert sample are "bluer" than predicted by any model F_L/F_M. We note that none of the torus models produces SEDs wherein $F_L/F_M \gtrsim 1$. We focus on color-color comparisons rather than SED fitting as they utilize the photometric data we have measured in this work, but we note that full SED fitting would be required to fully test the validity of the various torus models. Our comparisons are thus only qualitative, but they do give hints as to a preferred "torus" feature: the polar wind.

There are two explanations for this apparent discrepancy which are discussed in the following subsections: stellar contamination to the nuclear flux and incomplete representation of the 3-5μm bump in the torus models.

On average, we find that Sy1 are bluer than Sy2 in the NIR ($\log(F_{\rm L,Sy1}/F_{\rm M,Sy1}) \equiv \log(f_{\rm LM,Sy1}) = -0.05 \pm 0.18$ vs. $\log(f_{\rm LM,Sy2}) = -0.16 \pm 0.18$ and that they are also

[†] For further information on the SKIRTOR+wind model, please contact M. Stalevski.

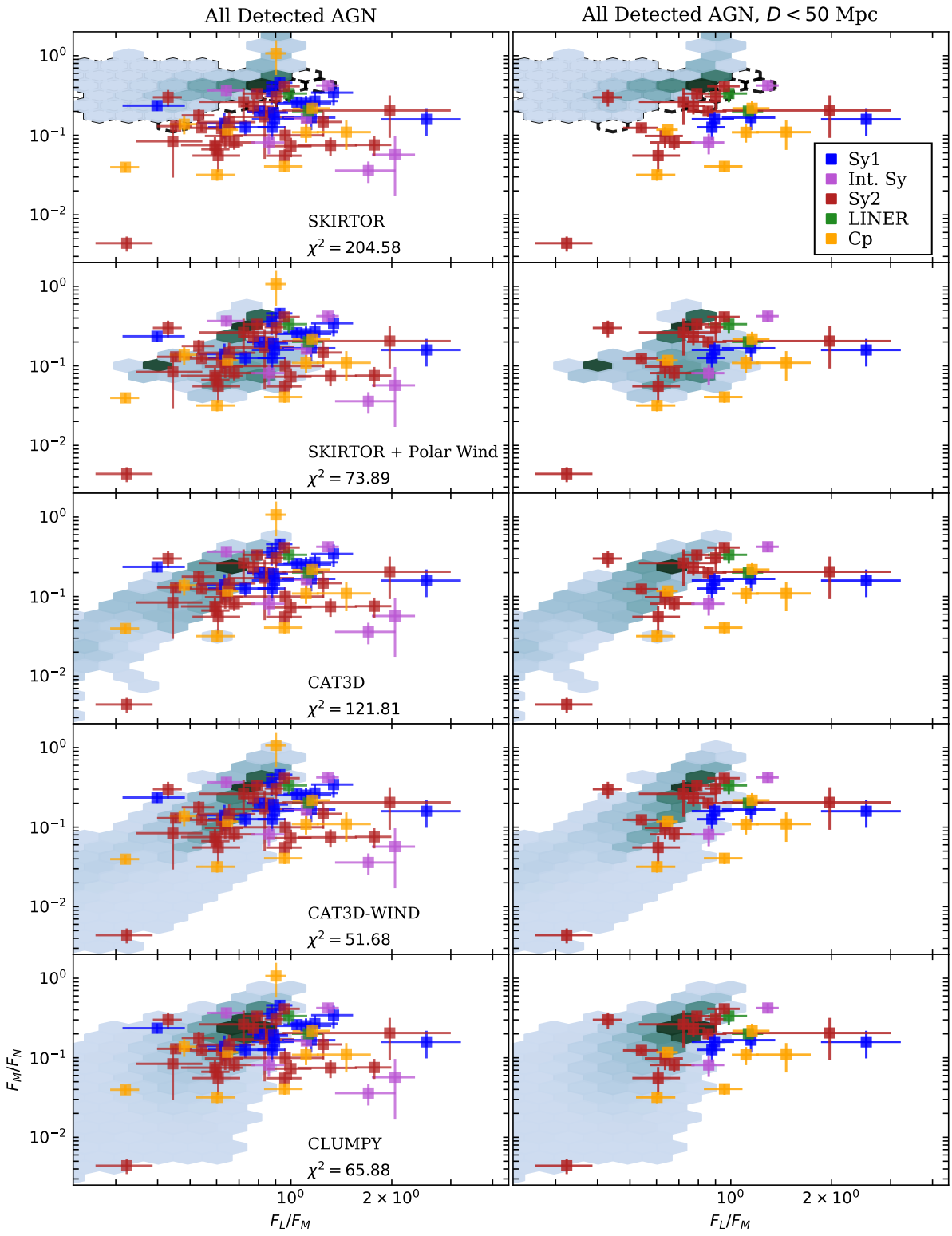

Figure 6. Comparisons of L/M and M/N flux ratios to those predicted by torus models SKIRTOR (Stalevski et al. 2016), SKIRTOR+Polar Wind, CLUMPY (Nenkova et al. 2008b), CAT3D (Hönig & Kishimoto 2010), and CAT3D-WIND (Hönig & Kishimoto 2017). Only includes sources with $\mathrm{SNR}_{gauss} > 3$ in both the L- and M-bands. Colors are the same as in Fig. 1. In the left panels we show all detected sources in our sample. In the right panels we show only AGN closer than 50 Mpc in our sample. The χ^2 value is measured from each data point to the model SED which provides the best fit. For SKIRTOR we show the effects of using the Kishimoto et al. (2008) accretion disk spectrum (described in §5.2) as a dashed contour.

slightly bluer in the MIR ($\log(F_{\rm M,Sy1}/F_{\rm N,Sy1}) \equiv \log(f_{\rm MN,Sy1}) = -0.70 \pm 0.17$ vs. $\log(f_{\rm MN,Sy2}) = -0.91 \pm 0.37$. In fact, Sy1 primarily populate the blue limit of the the torus SED models in F_L/F_M. The Sy2 sample shows much more diversity in both flux ratios, and there are several outliers which are much bluer than models predict. Only two LINERs were significantly detected in both L and M, so we cannot draw any conclusions about this population. The extremely mixed Cp subsample shows a large amount of scatter, but tends to be extremely "blue" compared to the Seyferts and to the models ($\log(f_{\rm LM,Cp}) = 0.05 \pm 0.24$)). It does not seem as if this diagram can be used to reliably separate different AGN types.

5.1. *Stellar Contamination*

The physical scales at which we extract the "nuclear" flux in this sample vary greatly, from $\sim$ 10pc to more that 1.5kpc. For essentially all sources at $D_{\rm AGN} \geq 50$Mpc, corresponding to an unresolved area $\theta_{\rm FWHM} \gtrsim 100$pc, we expect a significant contribution from the "red" tail of the stellar emission to our L-band fluxes. This stellar contribution would serve to make our AGN artificially bluer than the torus models. We therefore perform a simple distance cut, $D \leq 50$ Mpc, in order to focus on the polar dust region. We show this in Fig. 6. We find that after this cut, only two Seyfert galaxies are strictly $\geq 1\sigma$ bluer than the models. They are NGC 4235 (Sy1) and NGC 1365 (Sy1.8). This simple test then indicates qualitatively that increased stellar emission on larger scales could bias the AGN with $D > 50$Mpc to bluer colors.

More quantitatively, in Alonso-Herrero et al. (2001) the stellar contribution to the L-band within a 3″ diameter aperture was estimated to be up to 25% for a sample of 12 Sy2 AGN (except for NGC 5252 which had 65% stellar contribution). In the M-band it was estimated to be $< 10\%$. This indicates a blueward flux-ratio shift of $\log(F_{\rm L}/F_{\rm M}) \lesssim 0.1$. For their Sy1 sample (5 AGN) they assumed that 100% of the L-band flux was non-stellar in origin. We show the effects of stellar contamination in Fig. 7 by plotting the expected flux ratios of the AGN in our sample assuming they have 0%, 25%, and 65% stellar L-flux.

With a 25% L-band correction, 7 of the AGN in the full sample are still bluer than the models predict. If we allow for up to 65% of the L-flux to come from a stellar origin (i.e., the maximum percentage found in Alonso-Herrero et al. 2001), the shift increases to $\log(F_{\rm L}/F_{\rm M}) < 0.5$, which would make all the outliers in Fig. 6 consistent with the models.

We do not include an estimate of the M-band stellar flux because *i*) Alonso-Herrero et al. (2001) found it to be strictly $< 10\%$; *ii*) Assef et al. (2010) show that the AGN flux is steeply rising between the L- and M-bands while the stellar contribution steeply drops, indicating the M-band stellar contribution is $\lesssim 5\%$; and *iii*) subtracting an M-band contribution would actually serve to make AGN in Figs. 6-7 agree even less with the models by shifting them toward bluer colors.

5.1.1. *SINFONI-Estimated Stellar Fluxes*

For a subset of 21 AGN we can estimate the stellar contamination using K-band fluxes and AGN fractions derived by Burtscher et al. (2015). Using SINFONI, these fluxes were measured in the central 1" diameter aperture of each galaxy. Their near-IR AGN fractions ($f_{\rm AGN,K}$) were derived from spectral fitting in this central region and checked using the stellar CO equivalent width. We then used the average color of old stellar populations in stellar bulges, $K-L = 0.09$ mag, as measured from the empirical elliptical galaxy template of Assef et al. (2010), to calculate the expected L-band stellar magnitude as

$$L_{\rm mag,\star} = K_{\rm mag,total} + {\rm AGN}_{\rm mag,correction} - 0.09, \quad (3)$$

where ${\rm AGN}_{\rm mag,correction} = -\log_{10}((100 - f_{\rm AGN,K})/100)$ is a correction for the measured AGN fraction of the galaxy. We converted these magnitudes into ISAAC L fluxes.

We measured the ISAAC L fluxes of these 21 AGN using a central, 1" diameter aperture. We list the 1" aperture fluxes, the Gaussian-fitted nuclear fluxes, the estimated stellar fluxes, and the measured AGN fractions in Table 4. We show a comparison in Fig. 8 to illustrate the AGN fractions. Note that the typical unresolved nuclear flux in our sample has a FWHM of 0.75", so the stellar fractions could be slightly less in the unresolved nuclear fluxes on nights with average or better seeing. Note also that Circinus was measured in the SINFONI sample with a 0.5″ diameter aperture, which we match here; it is marked in Table 4 and Fig. 8.

We find that a rather large fraction of the AGN (13/21) should have $> 10\%$ of their ISAAC L nuclear flux come from stars rather than the unresolved nucleus. Two of these sources, NGC 4303 and NGC 4261, are shown to have $\approx 70\%$ stellar flux in the L-band. This is in rough agreement with the K-band $f_{\rm AGN,K} < 10\%$ estimates found by Burtscher et al. (2015). All but two of the AGN in this subsample agree with the findings of Alonso-Herrero et al. (2001), i.e., stellar contributions $\leq 65\%$.

We finally compare these AGN once more with the torus models in Fig. 7(right panel), but now with their K-band estimated stellar flux subtracted. Following this stellar correction, all of the AGN in this subsample are compatible with the torus SED models of CAT3D-WIND, CLUMPY, and SKIRTOR+wind. The stellar corrections required for CLUMPY are larger than for the torus+wind models as shown in Fig. 7. To correct all of the AGN nuclear fluxes in this sample, we would need similar SINFONI K-band data and stellar CO equivalent width measurements. For the nearest AGN, however, we expect this correction to be on the order of 1%, as exhibited by Circinus and NGC 1068.

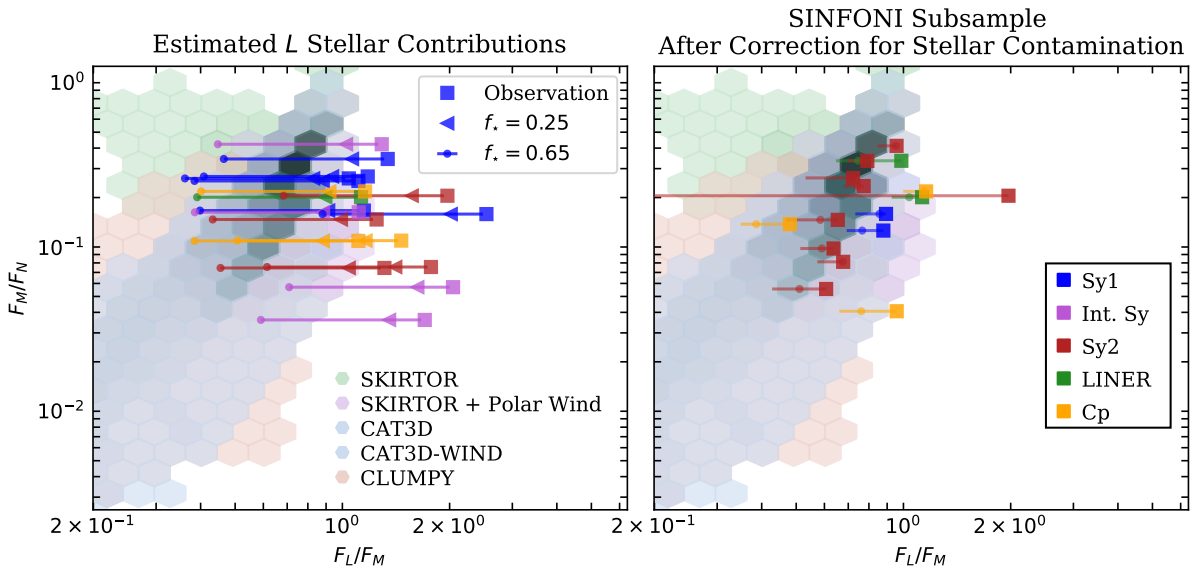

Figure 7. Comparisons of *L*/M and M/N flux ratios to those predicted by torus models SKIRTOR (green and purple; Stalevski et al. 2016), CAT3D (grey; Hönig & Kishimoto 2010), CLUMPY (orange;), and CAT3D-WIND (blue; Hönig & Kishimoto 2017). Only includes sources with $\mathrm{SNR}_{gauss} > 2$ in both the *L*- and M-bands. Colors same as in Fig. 1. In the left panel we show the sources which are bluer than models allow with corrections made for various $f_{\star,L}$. In the right panel we show the 21 AGN which had SINFONI fluxes in Burtscher et al. (2015) which we used to estimate *L*-band stellar contribution using Eq. 3.

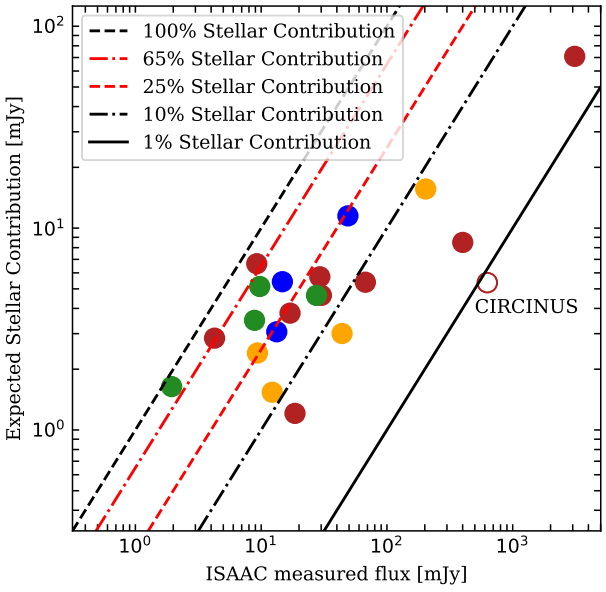

Figure 8. Comparison of SINFONI-estimated *L*-band stellar contributions and our measured 1" aperture fluxes from ISAAC. Overplotted are the lines showing what we expect if 100%, 65%, 25%, 10% and 1% of the flux is stellar in origin. Circinus is marked separately because it was measured with an aperture of 0.5" in both ISAAC and SINFONI observations. AGN are color coded as in Fig. 1.

5.2. *Accretion Disk Spectra*

The assumed spectrum of the accretion disk can play a large role in the final model SED. Traditionally a broken power-law has been assumed, i.e.,

$$\lambda F_\lambda \propto \begin{cases} \lambda^{1.2} & 0.001 \leq \lambda \leq 0.01\mu\mathrm{m} \\ \lambda^{0} & 0.01 < \lambda \leq 0.1\mu\mathrm{m} \\ \lambda^{-0.5} & 0.1 < \lambda \leq 5\mu\mathrm{m} \\ \lambda^{-3} & 5 < \lambda \leq 50\mu\mathrm{m} \end{cases} \quad (4)$$

(see e.g., Sanders et al. 1989; Kishimoto et al. 2008, and references therein). The spectrum produced by Eq. 4 was used in the models CLUMPY (Nenkova et al. 2008b) and SKIRTOR (Stalevski et al. 2016). More recently, however, a bluer accretion SED has been adopted which is strongly supported by QSO observations (e.g., Zheng et al. 1997; Manske et al. 1998; Vanden Berk et al. 2001; Scott et al. 2004; Kishimoto et al. 2008). This SED is relatively blue as it has a shallower power-law falloff $\nu F_\nu \propto \nu^{4/3}$ between 0.3 and 3μm:

$$\lambda F_\lambda \propto \begin{cases} \lambda^{1} & \lambda < 0.03 \\ \lambda^{0} & 0.03 < \lambda \leq .3 \\ \lambda^{-4/3} & 0.3 < \lambda \leq 3 \\ \lambda^{-3} & 3 < \lambda, \end{cases} \quad (5)$$

and it was used in both CAT3D and CAT3D-WIND (Hönig & Kishimoto 2010, 2017, respectively).

Target	L Flux$_{1as}$ [mJy]	L Flux$_{nuc.gauss}$ [mJy]	Est. L Flux$_{\star}$ [mJy]	f_{AGN}
Circinus	628.0 ± 6.5	459.3 ± 42.5	5.4	0.99
IC 5063	57.0 ± 0.1	57.0 ± 2.2	1.4	0.98
NGC 1068	3111.7 ± 6.2	2012.8 ± 238.8	70.9	0.98
NGC 1097	8.9 ± 0.1	5.6 ± 0.2	3.5	0.61
NGC 1386	30.1 ± 0.2	18.8 ± 1.0	4.6	0.85
NGC 1566	14.7 ± 0.1	10.6 ± 0.4	5.4	0.63
NGC 4261	1.9 ± 0.1	0.6 ± 0.1	1.6	0.16
NGC 4303	4.3 ± 0.1	1.6 ± 0.1	2.8	0.33
NGC 4303	4.3 ± 0.1	3.8 ± 0.2	2.2	0.50
NGC 4388	29.3 ± 0.1	33.9 ± 1.3	5.7	0.80
NGC 4501	9.2 ± 0.3	1.5 ± 0.2	5.1	0.44
NGC 4579	27.5 ± 0.2	16.9 ± 0.6	6.7	0.76
NGC 4593	49.0 ± 0.2	32.3 ± 2.5	4.6	0.91
NGC 5135	18.6 ± 0.2	12.6 ± 0.7	11.5	0.38
NGC 5506	400.6 ± 0.3	343.8 ± 12.5	1.2	1.00
NGC 5643	17.0 ± 0.1	8.5 ± 0.5	8.5	0.50
NGC 6814	13.3 ± 0.1	10.6 ± 0.4	3.0	0.77
NGC 7130	12.3 ± 0.1	6.9 ± 0.3	3.1	0.75
NGC 7172	67.4 ± 0.2	49.1 ± 2.0	1.5	0.98
NGC 7496	9.3 ± 0.1	6.6 ± 0.3	5.4	0.42
NGC 7582	150.8 ± 0.6	86.1 ± 5.3	2.4	0.98

Table 4. Measured 1" diameter aperture flux, measured nuclear Gaussian flux, estimated stellar flux using SINFONI K-band measurements and Eq. 3, and measured AGN fraction for 21 cross-matched AGN.

In order to test the role the model accretion disk spectrum plays in the L- and M-bands, we replaced Eq. 4 with Eq. 5 in the SKIRTOR models using the method outlined in Yang et al. (2020). The results of this replacement are shown in Fig.6. The overall effect of this replacement is to shift the models' flux ratios F_L/F_M "blueward", i.e., to the right in our plots. After this replacement, the SKIRTOR models with the bluer accretion disk are a better match to the data $\chi^2_{\rm SKIRTOR} = 204.58 \rightarrow \chi^2_{\rm Bluer\ AD} = 174.17$, but this shift is not enough to explain observations with $F_L/F_M > 1$. We show the effects of changing the accretion disk spectrum in Fig. 6 as a dashed contour in the SKIRTOR panels. The CLUMPY library provides two sets of models: one with only dust emission from the torus, and another which includes the accretion disk. However, the accretion disk emission is not traced in the radiative transfer calculations. Rather, it is up to the user to decide which one to use, e.g. based on the probability to have a clear line of sight to the central source for the given model. While this is not fully consistent treatment, we tested both versions and found the difference to be very small ($\Delta\chi^2_{\rm CLUMPY} < 1$). We conclude that including the accretion disk flux in CLUMPY models has an insignificant effect on the model predictions. In both cases, only a radically different accretion disk spectrum could explain these data, so stellar contamination is still favored.

5.3. *Polar Elongation and the 3-5 Micron Bump*

It is also possible that the MIR flux is underestimated in modern torus models. It has been well documented that many QSOs and Sy1 galaxies exhibit what is called the 3-5 μm bump (e.g., Edelson & Malkan 1986; Kishimoto et al. 2011; Mor & Netzer 2012; Hönig et al. 2013). This feature was thought to be caused by the presence of inter-clump dust, but recent work by Hönig & Kishimoto (2017) claims that the addition of wind orthogonal to the accretion disk can explain it. In CAT3D-WIND, Hönig & Kishimoto (2017) this feature is apparently caused by a large amount of dust in a "puffed-up" region in the vicinity of the sublimation ring or by winds which remove clouds from the central few pc and cause the SED to be split into the hot dust emission from the center and the cold dust emission from a region elongated in the polar direction. A similar conclusion is valid for the models based on SKIRTOR with polar winds: the additional dust of low optical depth at the base of the wind is responsible for additional 3-5 μm emission and "bluer" colors.

It appears that within our sample, the differences between observations and the models are sufficiently explained by stellar contamination in the L-band. The AGN in our sample agree best with CAT3D-WIND(Hönig & Kishimoto 2017), indicating that the inclusion of the polar wind describes AGN at this resolution quite well. Moreover, the SKIRTOR (Stalevski et al. 2016) models fit the data much better after the inclusion of a polar wind. On the other hand, we find that CLUMPY (Nenkova et al. 2008b) provides good fits to the data without polar winds. It will be interesting to further investigate the nuclear regions of NGC 1365 and NGC 4235 with MATISSE, testing whether these "too blue" Seyferts are sufficiently explained by stellar contamination.

6. ESTIMATING VLT FLUXES FROM *WISE*

The Wide-field Infrared Survey Explorer (*WISE*) space telescope (Wright et al. 2010) has observed a large number of AGN in the MIR at high sensitivity but limited spatial resolution. Moreover, the ALLWISE AGN catalog contains 1.4 million AGN selected using 3 *WISE* bands (Secrest et al. 2015). This catalog and others like it present a rich source from which to draw AGN for further study in the MIR. The median point-spread-function in the *W1*-band has a FWHM of 6", making it nearly impossible to spatially distinguish thermal torus emission from star formation in the foreground or even the central few hundred parsecs of even nearby AGN. The large spatial areas probed by *WISE* in each AGN will bias the flux to be comparatively larger than seen from the

8-10m class telescopes used in MIR interferometry. In order to select AGN from a much larger parent sample for MATISSE followup from *WISE*, we study the relationships between *WISE* colors, *WISE* fluxes, and the fraction of nuclear flux observable at the VLT(I).

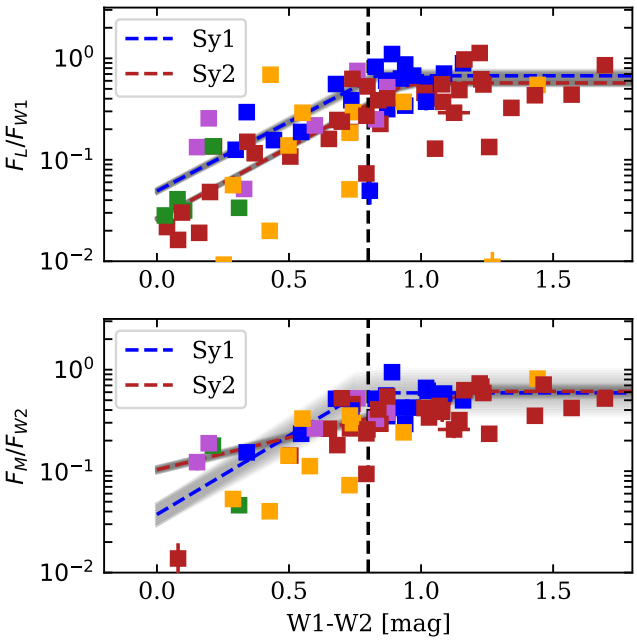

Figure 9. *Top) L/W1* flux ratio vs. *W1-W2*. *Bottom) M/W2* flux ratio vs. *W1-W2*. For each panel only detected ($SNR_{gauss} > 2$ in each band) sources are included. Colors same as Fig 1. The black line at *W1-W2*= 0.8 indicates the AGN selection cutoff of Stern et al. (2012), which is also the point after which $F_L/F_{W1} \approx 1$ in our Sy1 sample. Blue and red dashed lines are fitted piece-wise functions (Eq. 5-8) for the Sy1 and Sy2 samples, respectively. Grey shaded regions are the 1σ fit errors.

We explore the relationships between the measured ISAAC fluxes and the existing *WISE* fluxes for each source in order to determine a scaling between the space-based MIR measurements and nuclear fluxes measured at the VLTI. By providing an estimate for the fluxes observed at the VLT, we can select AGN for follow-up observations directly from the *WISE* catalog. This is not straightforward because the *WISE* telescope has a lower resolution than the VLT and because the filters *W1* and *W2* are both wider than and offset from either L' or M_{nb}. The resolution in the *W1* band is $6.1''$ and is $6.4''$ in the *W2* band (Wright et al. 2010), while these ISAAC observations are seeing limited at $\lesssim 1''$. This means that in general we expect $F_{ISAAC}/F_{WISE} \leq 1$, as there will be a contribution from non-nuclear flux, especially at shorter wavelengths wherein the stellar contribution is higher. In Fig. 9 we show the ratios F_L/F_{W1} and F_M/F_{W2} for each detected ($SNR_{gauss} > 2$) AGN in our sample. Note that F_L/F_{W1} and F_M/F_{W2} are occasionally > 1. This is due to the offset in the filters: *L* is redder than *W1*, and it therefore measures a larger relative flux from the nuclear dust emission in the same AGN. Nevertheless, for both the Sy1 and the Sy2 subsamples we see a linearly increasing trend in F_{ISAAC}/F_{WISE} for blue *W1-W2* colors until a "saturation" point at *W1-W2*≈ 0.8 mag. This point occurs at roughly the same *W1-W2* color in both subsamples in both bands. To further quantify this, we fit a linear piece-wise function to each subsample of the form

$$f(W1-W2) = \begin{cases} ap+b, & \text{if } (W1-W2) \geq p \\ a(W1-W2)+b, & \text{else} \end{cases} \quad (6)$$

where p is the fitted point at which $F_{ISAAC}/F_{WISE} \approx 1$. The fitted lines are shown in Fig. 9 with 1σ errors shaded in gray. Fitting was done using `curve_fit` from `scipy.optimize`, employing the Levenberg-Marquardt algorithm. Errors are estimated from the diagonal of the covariance matrix, with the implicit assumption that they are uncorrelated. We find that for the Sy1 sample, the *L* flux matches the *W1* flux for $W1-W2 \geq 1.05 \pm 0.03$ mag. For the Sy2 sample this cutoff is $W1-W2 \geq 0.90 \pm 0.01$ mag, much redder than for the Sy1 sample. For Sy1 and Sy2 galaxies we can estimate the *L* nuclear flux from the *W1* flux as

$$\log_{10} F_{L,Sy1} = \quad (7)$$
$$\begin{cases} \log_{10} F_{W1} - 0.05 \pm 0.002, \text{ if } (W1-W2) \geq 1.05 \pm 0.03 \\ \log_{10} F_{W1} + (1.12 \pm 0.03)(W1-W2) - (1.23 \pm 0.02), \text{ else} \end{cases}$$
$$\log_{10} F_{L,Sy2} = \quad (8)$$
$$\begin{cases} \log_{10} F_{W1} - 0.23 \pm 0.004, \text{ if } (W1-W2) \geq 0.90 \pm 0.01 \\ \log_{10} F_{W1} + (1.51 \pm 0.03)(W1-W2) - (1.61 \pm 0.01), \text{ else.} \end{cases}$$

The WISE *W1-W2* color at which the ISAAC and *WISE* fluxes match is similar to *W1-W2* color used to select AGN in WISE. Stern et al. (2012) define an AGN selection color cut of W1-W2≥ 0.8 mag. We plot the Stern et al. (2012) criterion in Fig. 9 as a black dashed line for comparison. This cut was motivated by the desire to find high-redshift AGN ($z < 3$), so it is unsurprising that local AGN may exhibit much bluer *W1-W2* colors. Indeed, Mateos et al. (2012) show that *W1-W2* is redder for high-redshift AGN.

In the *M*-band we find similar trends, albeit with significantly more scatter. The Sy1 sample shows a match between M and *W2* when $W1-W2 \geq 0.78 \pm 0.02$ mag; while the Sy2 sample does the same at the much redder $W1-W2 \geq 1.19 \pm 0.02$ mag. For Sy1 and Sy2 galaxies we estimate the M-band nuclear flux from the *W2* flux as

$$\log_{10} F_{\mathrm{M,Sy1}} = \quad (9)$$
$$\begin{cases} \log_{10} F_{W2} - 0.23 \pm 0.03, \text{ if } (W1-W2) \geq 0.78 \pm 0.02 \\ \log_{10} F_{W2} + (1.48 \pm 0.15)(W1-W2) - (1.38 \pm 0.10), \text{ else} \end{cases}$$
$$\log_{10} F_{\mathrm{M,Sy2}} = \quad (10)$$
$$\begin{cases} \log_{10} F_{W2} - 0.16 \pm 0.01, \text{ if } (W1-W2) \geq 1.19 \pm 0.02 \\ \log_{10} F_{W2} + (0.73 \pm 0.03)(W1-W2) - (1.03 \pm 0.03), \text{ else.} \end{cases}$$

We find that in both bands, Circinus is "underluminous" relative to the general trend. It is likely here that we are over-resolving emission that *WISE* cannot spatially distinguish, as it is at a distance of only 4 Mpc. Another of the outliers, NGC 4355 (a.k.a. NGC 4418), is a compact obscured nucleus (CON) known to exhibit an SED unusual for Sy2 galaxies (e.g., Costagliola et al. 2011; Ohyama et al. 2019). We also note that NGC 5953 (the extremely "blue" galaxy above) is underluminous for either the Sy1 or Sy2 trends, but roughly agrees with other Cp AGN in our sample.

In summary, for Sy1 with WISE colors *W1-W2*$\geq$ 1.05 mag the *WISE W1* flux is a good proxy for the *L* flux at the VLT. For Sy2 with *WISE* colors *W1-W2*$\geq$ 0.90 mag the *WISE W1* flux is a good proxy for the *L* flux at the VLT. We present functions which use the *W1-W2* color and the *W1* (or *W2*) flux to reliably estimate the *L*-band (or M-band) fluxes observable at the VLT with instruments such as VLTI MATISSE, ERIS, and CRIRES.

6.1. *Potential VLTI/MATISSE Targets*

The short atmospheric coherence times in the *L*, *M*, and *N* bands severely limit the sensitivity of self-tracked interferometric observations in these bands with VLTI/MATISSE. This necessitates bright targets for detailed study. The recommended limits for *L*-band target flux are 75 mJy when using the UTs and 1 Jy when using the ATs. Using these limits, we can identify 13 potential MATISSE targets in our sample, 2 of which are observable with the ATs. Most of these (10/13) have been previously observed either with MIDI or already with MATISSE as part of commissioning and/or guaranteed time observations. Fortunately, we can use the above formulae to estimate *L*-band fluxes from various *WISE* catalogs and identify potential targets. Here a potential target means *L*-band fluxes greater than those listed above and declination $\delta < 20$ deg.

Using the mid-IR photometrically-selected *WISE* AGN Candidates Catalogs(Assef et al. 2018), we apply Eq. 7 to esimate the *L*-flux. We use the Assef et al. (2018) R90 catalog ($\sim$ 4 million AGN), which has 90% reliability, to identify 57 potential targets, 2 of which can be observed with the ATs.

In addition to using photometrically selected catalogs, we cross-matched the Véron-Cetty & Véron (2010) AGN catalog with the ALLWISE catalog to create a sample of optically classified AGN that had been detected using *WISE*. Using then the *W1* and *W2* fluxes, we computed the *L*-band fluxes using Eq. 7. In this way, we identify 44 AGN suitable for follow-up, 4 of which can be observed with the ATs. Many of the AGN in the Véron-Cetty & Véron (2010) catalog are not included in color-selected *WISE* AGN catalogs (e.g., Assef et al. 2018; Secrest et al. 2015) because the color cuts employed focus on high-redshift sources (e.g., Mateos et al. 2012). Thus this second approach is helpful if one wishes to focus on nearby AGN.

7. SUMMARY AND CONCLUSIONS

In this work we present a MIR flux catalog of 119 AGN, extending the work done by Asmus et al. (2014) from the *N*- and *Q*-bands to the *L*- and *M*-bands. This is the largest existing subarcsecond catalog of AGN in these bands. Each AGN was observed using VLT ISAAC in at least one of the *L*- and *M*-bands between 2000 and 2013. We include local ($z < 0.3$) AGN of 5 optical classifications: 21 are Seyfert 1; 5 are Intermediate Seyferts; 46 are Seyfert 2; 29 are LINERs; and 16 are so-called 'Cp' or Composites. We report two tables: one with nuclear fluxes in the *L*- and *M*-bands, and one with resolved emission fluxes, sizes, and PAs in both bands. The nuclear and resolved emission were separated by fitting one Gaussian to the PSF and one to the flux on scales larger than the PSF. We detect 98 sources in the *L*-band and 81 sources in the *M*-band. We found resolved *L*-band emission in 73 of the AGN.

We compared the flux ratios $F_{\mathrm{L}}/F_{\mathrm{M}}$ and $F_{\mathrm{M}}/F_{\mathrm{N}}$ to those predicted by several suites of AGN torus models: CAT3D (Hönig & Kishimoto 2010), CAT3D-WIND (Hönig & Kishimoto 2017), CLUMPY (Nenkova et al. 2008b), SKIRTOR (Stalevski et al. 2016), and SKIRTOR models with polar winds. We find that the inclusion of a polar wind component significantly improves the agreement between our measurements and model predictions. CAT3D-WIND provides the best overall match to our measurements. The SKIRTOR (Stalevski et al. 2016) models fit the data much better after the inclusion of a polar wind. Notably, we find that CLUMPY (Nenkova et al. 2008b) provides good fits to the data without polar winds. No set of models, however, produces values of $F_{\mathrm{L}}/F_{\mathrm{M}} \gtrsim 1$, which we measure in 10 Seyfert galaxies. We discuss two possible explanations of this: stellar contamination in the relatively large physical scales probed; and underestimation of *L*-band accretion disk flux in torus models.

We favor the stellar contamination hypothesis, as several of the AGN in this sample (e.g., NGC5252) were shown in Alonso-Herrero et al. (2001) to have up to 65% of their *L*-band emission come from stellar sources rather than the AGN. We also use *K*-band flux measurements of 21 cross-

matched AGN from Burtscher et al. (2015) to estimate the L-flux contribution from stars using the Assef et al. (2010) $K-L$ colors for old stellar populations. After removing this estimated stellar contribution, all of the AGN become consistent with CAT3D-WIND, CLUMPY, and SKIRTOR+wind. We find that the stellar corrections necessary to match CLUMPY are $\approx 10\%$ larger than for the torus+wind models.

We measured the effect of changing the accretion disk spectrum in the SKIRTOR models to a QSO-motivated and relatively bluer spectrum. We find that while it does improve the agreement between these models and the observations, it does not fully reproduce the observed F_L/F_M. Nonetheless, follow-up observations of these NIR "blue" AGN may provide insight into the mechanisms driving the 3-5μm bump and the formation of these dusty tori.

We lastly derived relations between the reported WISE *W1* and *W2* fluxes and the *L* and *M* fluxes observable at the VLT. These relations (Eq. 7-10) can be used to estimate the NIR fluxes for sources not included in this survey, using only the WISE *W1* and *W2* bands. This is especially useful for potential VLTI/MATISSE targets, allowing one to determine their observability and the possibility of resolving nuclear extended dusty structures.

This MIR AGN atlas holds a significant portion of local AGN of all optical classifications. It represents a statistically relevant sample suitable for AGN unification studies and interferometric follow-up. The need for such interferometric follow-up with VLTI/MATISSE is evinced by the fact that even our high-resolution 8m telescope data has a significant fraction of sources with unresolved MIR dust emission.

ACKNOWLEDGEMENTS

L.B. acknowledges discussions with Dieter Lutz. D.A. acknowledges funding through the European Union's Horizon 2020 and Innovation program under the Marie Sklodowska-Curie grant agreement no. 793499 (DUSTDEVILS). M.S. acknowledges support by the Ministry of Education, Science and Technological Development of the Republic of Serbia through the contract no. 451-03-68/2020-14/200002 and the Science Fund of the Republic of Serbia, PROMIS 6060916, BOWIE. J.I. and L.B. acknowledge *Astronomers for Planet Earth* and other efforts to raise awareness of the impact of astronomy on global CO_2 emissions. J.I. and L.B. pledge to not travel via airplane to promote this paper. This research has made use of the services of the ESO Science Archive Facility.

Facilities: VLT:Melipal (ISAAC), WISE

Software: astropy (Astropy Collaboration et al. 2018), matplotlib (Hunter 2007), Scipy (Jones et al. 2001), emcee (Foreman-Mackey et al. 2013), and VIPE (https://github.com/danielasmus/vipe) .

REFERENCES

Aalto, S., Wilner, D., Spaans, M., et al. 2009, Astronomy and Astrophysics, 493, 481, doi: 10.1051/0004-6361:200810394

Alonso-Herrero, A., Quillen, A. C., Simpson, C., Efstathiou, A., & Ward, M. J. 2001, The Astronomical Journal, 121, 1369, doi: 10.1086/319410

Alonso-Herrero, A., Ramos Almeida, C., Mason, R., et al. 2011, The Astrophysical Journal, 736, 82, doi: 10.1088/0004-637X/736/2/82

Antonucci, R. 1993, Annual Review of Astronomy and Astrophysics, 31, 473, doi: 10.1146/annurev.aa.31.090193.002353

Asmus, D., Hönig, S. F., & Gandhi, P. 2016, The Astrophysical Journal, 822, 109, doi: 10.3847/0004-637X/822/2/109

Asmus, D., Hönig, S. F., Gandhi, P., Smette, A., & Duschl, W. J. 2014, Monthly Notices of the Royal Astronomical Society, 439, 1648, doi: 10.1093/mnras/stu041

Assef, R. J., Stern, D., Noirot, G., et al. 2018, The Astrophysical Journal Supplement Series, 234, 23, doi: 10.3847/1538-4365/aaa00a

Assef, R. J., Kochanek, C. S., Brodwin, M., et al. 2010, The Astrophysical Journal, 713, 970, doi: 10.1088/0004-637X/713/2/970

Astropy Collaboration, Price-Whelan, A. M., Sipőcz, B. M., et al. 2018, The Astronomical Journal, 156, 123, doi: 10.3847/1538-3881/aabc4f

Burtscher, L., Meisenheimer, K., Tristram, K. R. W., et al. 2013, Astronomy and Astrophysics, 558, A149, doi: 10.1051/0004-6361/201321890

Burtscher, L., Orban de Xivry, G., Davies, R. I., et al. 2015, Astronomy and Astrophysics, 578, A47, doi: 10.1051/0004-6361/201525817

Costagliola, F., Aalto, S., Rodriguez, M. I., et al. 2011, Astronomy and Astrophysics, 528, A30, doi: 10.1051/0004-6361/201015628

Edelson, R. A., & Malkan, M. A. 1986, The Astrophysical Journal, 308, 59, doi: 10.1086/164479

Forbes, D. A., Norris, R. P., Williger, G. M., & Smith, R. C. 1994, The Astronomical Journal, 107, 984, doi: 10.1086/116911

Foreman-Mackey, D., Hogg, D. W., Lang, D., & Goodman, J. 2013, Publications of the Astronomical Society of the Pacific, 125, 306, doi: 10.1086/670067

García-Bernete, I., Ramos Almeida, C., Alonso-Herrero, A., et al. 2019, Monthly Notices of the Royal Astronomical Society, 486, 4917, doi: 10.1093/mnras/stz1003

García-González, J., Alonso-Herrero, A., Hernán-Caballero, A., et al. 2016, Monthly Notices of the Royal Astronomical Society, 458, 4512, doi: 10.1093/mnras/stw626

Gaskell, C. M., Goosmann, R. W., Antonucci, R. R. J., & Whysong, D. H. 2004, ApJ, 616, 147, doi: 10.1086/423885

González-Martín, O., Masegosa, J., García-Bernete, I., et al. 2019, ApJ, 884, 11, doi: 10.3847/1538-4357/ab3e4f

Gravity Collaboration, Dexter, J., Shangguan, J., et al. 2020, Astronomy and Astrophysics, 635, A92, doi: 10.1051/0004-6361/201936767

Hameed, S., & Devereux, N. 1999, The Astronomical Journal, 118, 730, doi: 10.1086/300956

Hernán-Caballero, A., & Hatziminaoglou, E. 2011, Monthly Notices of the Royal Astronomical Society, 414, 500, doi: 10.1111/j.1365-2966.2011.18413.x

Ho, L. C., Filippenko, A. V., & Sargent, W. L. W. 1997, The Astrophysical Journal Supplement Series, 112, 315, doi: 10.1086/313041

Hönig, S. F., & Kishimoto, M. 2010, Astronomy and Astrophysics, 523, A27, doi: 10.1051/0004-6361/200912676

—. 2017, The Astrophysical Journal Letters, 838, L20, doi: 10.3847/2041-8213/aa6838

Hönig, S. F., Kishimoto, M., Tristram, K. R. W., et al. 2013, The Astrophysical Journal, 771, 87, doi: 10.1088/0004-637X/771/2/87

Kishimoto, M., Antonucci, R., Blaes, O., et al. 2008, Nature, 454, 492, doi: 10.1038/nature07114

Kishimoto, M., Hönig, S. F., Antonucci, R., et al. 2011, Astronomy and Astrophysics, 536, A78, doi: 10.1051/0004-6361/201117367

Krolik, J. H., & Begelman, M. C. 1988, The Astrophysical Journal, 329, 702, doi: 10.1086/166414

Leftley, J. H., Hönig, S. F., Asmus, D., et al. 2019, The Astrophysical Journal, 886, 55, doi: 10.3847/1538-4357/ab4a0b

Lira, P., Videla, L., Wu, Y., et al. 2013, The Astrophysical Journal, 764, 159, doi: 10.1088/0004-637X/764/2/159

Lopez, B., Lagarde, S., Jaffe, W., et al. 2014, The Messenger, 157, 5. http://adsabs.harvard.edu/abs/2014Msngr.157....5L

López-Gonzaga, N., Jaffe, W., Burtscher, L., Tristram, K. R. W., & Meisenheimer, K. 2014, Astronomy and Astrophysics, 565, A71, doi: 10.1051/0004-6361/201323002

Makarov, D., Prugniel, P., Terekhova, N., Courtois, H., & Vauglin, I. 2014, Astronomy and Astrophysics, 570, A13, doi: 10.1051/0004-6361/201423496

Manske, V., Henning, T., & Men'shchikov, A. B. 1998, Astronomy and Astrophysics, 331, 52. http://adsabs.harvard.edu/abs/1998A%26A...331...52M

Martínez-Paredes, M., González-Martín, O., Esparza-Arredondo, D., et al. 2020, The Astrophysical Journal, 890, 152, doi: 10.3847/1538-4357/ab6732

Mateos, S., Alonso-Herrero, A., Carrera, F. J., et al. 2012, Monthly Notices of the Royal Astronomical Society, 426, 3271, doi: 10.1111/j.1365-2966.2012.21843.x

Mathis, J. S., Rumpl, W., & Nordsieck, K. H. 1977, ApJ, 217, 425, doi: 10.1086/155591

Moorwood, A., Cuby, J.-G., Ballester, P., et al. 1999, The Messenger, 95, 1. https://ui.adsabs.harvard.edu/abs/1999Msngr..95....1M/abstract

Mor, R., & Netzer, H. 2012, Monthly Notices of the Royal Astronomical Society, 420, 526, doi: 10.1111/j.1365-2966.2011.20060.x

Nenkova, M., Ivezić, Ž., & Elitzur, M. 2002, The Astrophysical Journal Letters, 570, L9, doi: 10.1086/340857

Nenkova, M., Sirocky, M. M., Ivezić, Ž., & Elitzur, M. 2008a, The Astrophysical Journal, 685, 147, doi: 10.1086/590482

Nenkova, M., Sirocky, M. M., Nikutta, R., Ivezić, Ž., & Elitzur, M. 2008b, The Astrophysical Journal, 685, 160, doi: 10.1086/590483

Netzer, H. 2015, Annual Review of Astronomy and Astrophysics, 53, 365, doi: 10.1146/annurev-astro-082214-122302

Ohyama, Y., Sakamoto, K., Aalto, S., & Gallagher, III, J. S. 2019, The Astrophysical Journal, 871, 191, doi: 10.3847/1538-4357/aaf9a5

Ramos Almeida, C., Levenson, N. A., Rodríguez Espinosa, J. M., et al. 2009, The Astrophysical Journal, 702, 1127, doi: 10.1088/0004-637X/702/2/1127

Sanders, D. B., Phinney, E. S., Neugebauer, G., Soifer, B. T., & Matthews, K. 1989, ApJ, 347, 29, doi: 10.1086/168094

Schartmann, M., Meisenheimer, K., Camenzind, M., et al. 2008, Astronomy and Astrophysics, 482, 67, doi: 10.1051/0004-6361:20078907

Scott, J. E., Kriss, G. A., Brotherton, M., et al. 2004, The Astrophysical Journal, 615, 135, doi: 10.1086/422336

Secrest, N. J., Dudik, R. P., Dorland, B. N., et al. 2015, The Astrophysical Journal Supplement Series, 221, 12, doi: 10.1088/0067-0049/221/1/12

Shao, Z., Jiang, B. W., & Li, A. 2017, ApJ, 840, 27, doi: 10.3847/1538-4357/aa6ba4

Soifer, B. T., Neugebauer, G., Matthews, K., et al. 1999, The Astrophysical Journal, 513, 207, doi: 10.1086/306855

Stalevski, M., Asmus, D., & Tristram, K. R. W. 2017, MNRAS, 472, 3854, doi: 10.1093/mnras/stx2227

Stalevski, M., Ricci, C., Ueda, Y., et al. 2016, Monthly Notices of the Royal Astronomical Society, 458, 2288, doi: 10.1093/mnras/stw444

Stalevski, M., Tristram, K. R. W., & Asmus, D. 2019, MNRAS, 484, 3334, doi: 10.1093/mnras/stz220

Stern, D., Assef, R. J., Benford, D. J., et al. 2012, The Astrophysical Journal, 753, 30, doi: 10.1088/0004-637X/753/1/30

Tristram, K. R. W., Burtscher, L., Jaffe, W., et al. 2014, Astronomy and Astrophysics, 563, A82, doi: 10.1051/0004-6361/201322698

Urry, C. M., & Padovani, P. 1995, Publications of the Astronomical Society of the Pacific, 107, 803, doi: 10.1086/133630

van der Bliek, N. S., Manfroid, J., & Bouchet, P. 1996, Astronomy and Astrophysics Supplement Series, 119, 547. http://adsabs.harvard.edu/abs/1996A%26AS..119..547V

Vanden Berk, D. E., Richards, G. T., Bauer, A., et al. 2001, The Astronomical Journal, 122, 549, doi: 10.1086/321167

Véron-Cetty, M.-P., & Véron, P. 2010, Astronomy and Astrophysics, 518, A10, doi: 10.1051/0004-6361/201014188

Weigelt, G., Wittkowski, M., Balega, Y. Y., et al. 2004, Astronomy and Astrophysics, 425, 77, doi: 10.1051/0004-6361:20040362

Wittkowski, M., Balega, Y., Beckert, T., et al. 1998, Astronomy and Astrophysics, 329, L45. http://adsabs.harvard.edu/abs/1998A%26A...329L..45W

Wright, E. L., Eisenhardt, P. R. M., Mainzer, A. K., et al. 2010, The Astronomical Journal, 140, 1868, doi: 10.1088/0004-6256/140/6/1868

Xie, Y., Li, A., & Hao, L. 2017, ApJS, 228, 6, doi: 10.3847/1538-4365/228/1/6

Yang, G., Boquien, M., Buat, V., et al. 2020, Monthly Notices of the Royal Astronomical Society, 491, 740, doi: 10.1093/mnras/stz3001

Yuan, T.-T., Kewley, L. J., & Sanders, D. B. 2010, The Astrophysical Journal, 709, 884, doi: 10.1088/0004-637X/709/2/884

Zheng, W., Kriss, G. A., Telfer, R. C., Grimes, J. P., & Davidsen, A. F. 1997, The Astrophysical Journal, 475, 469, doi: 10.1086/303560

APPENDIX

A. SELECTED EPOCHS AND OBSERVING CONDITIONS

Table 5. Observational Data for all Sources and Epochs

Target Name	Obs. Date	Obs. Program	Filter	Exp. Time	PSF FWHM	Nuc. Flux	Ext. Flux	Flag
				sec	"	[mJy]	[mJy]	
3C 273	2013-07-07T00:46:53	290.B-5113(A)	L'	118	0.46	91.67 ± 7.34	69.71 ± 30.55	0
3C 273	2013-07-07T00:51:00	290.B-5113(A)	$M_{\rm nb}$	118	0.42	77.81 ± 7.09	74.14 ± 22.28	0
3C 317	2013-07-03T02:16:39	290.B-5113(A)	L'	472	0.41	≤ 0.41	≤ 0.33	1
3C 317	2013-07-03T02:29:07	290.B-5113(A)	$M_{\rm nb}$	944	0.42	≤ 2.35	≤ 2.05	1
3C 321	2013-06-27T03:06:14	290.B-5113(A)	L'	118	0.47	0.37 ± 0.06	≤ 0.69	2
3C 321	2013-06-27T03:10:22	290.B-5113(A)	$M_{\rm nb}$	236	0.36	≤ 4.95	≤ 4.30	3
3C 321	2013-07-04T02:02:53	290.B-5113(A)	L'	118	0.32	0.47 ± 0.07	≤ 0.66	1
3C 321	2013-07-04T02:07:02	290.B-5113(A)	$M_{\rm nb}$	236	0.30	≤ 4.63	≤ 3.83	3
3C 327	2013-07-04T02:32:55	290.B-5113(A)	L'	236	0.34	0.92 ± 0.05	≤ 0.42	0
3C 327	2013-07-04T02:39:44	290.B-5113(A)	$M_{\rm nb}$	472	0.37	1.27 ± 0.20	≤ 2.69	1
3C 353	2013-07-02T05:08:55	290.B-5113(A)	L'	118	0.54	1.26 ± 0.10	≤ 0.67	0
3C 353	2013-07-02T05:13:02	290.B-5113(A)	$M_{\rm nb}$	236	0.52	≤ 4.94	≤ 4.54	3
3C 403	2013-07-02T06:03:52	290.B-5113(A)	L'	118	0.54	5.00 ± 0.19	≤ 0.69	0
3C 403	2013-07-02T06:07:58	290.B-5113(A)	$M_{\rm nb}$	236	0.52	5.21 ± 0.43	≤ 3.72	0
3C 424	2013-06-27T08:52:04	290.B-5113(A)	L'	472	0.68	0.17 ± 0.04	≤ 0.32	3
3C 424	2013-06-27T09:04:25	290.B-5113(A)	$M_{\rm nb}$	944	0.66	≤ 5.48	≤ 5.27	3
3C 424	2013-07-03T05:41:24	290.B-5113(A)	L'	472	0.41	≤ 0.43	≤ 0.34	1
3C 424	2013-07-03T05:53:51	290.B-5113(A)	$M_{\rm nb}$	944	0.42	≤ 2.16	≤ 1.88	3
Arp 220	2000-07-13T01:26:21	65.P-0519(A)	L'	720	0.46	≤ 0.29	12.41 ± 0.49	0
Arp 220	2000-07-13T01:49:23	65.P-0519(A)	$M_{\rm nb}$	2340	0.56	≤ 1.16	6.13 ± 0.50	0
Arp 220	2001-06-11T03:33:02	67.B-0332(A)	L'	90	0.64	≤ 3.91	9.96 ± 1.21	2
Arp 220	2001-06-11T03:38:27	67.B-0332(A)	L'	600	0.64	3.95 ± 0.44	4.28 ± 0.92	0
Arp 220	2001-06-11T03:54:05	67.B-0332(A)	$M_{\rm nb}$	120	0.56	15.24 ± 1.69	≤ 26.05	3
Arp 220	2001-06-12T03:07:40	67.B-0332(A)	L'	570	0.64	3.75 ± 0.30	≤ 1.55	0
Arp 220	2001-08-11T23:16:52	67.B-0332(A)	L'	600	0.45	≤ 0.52	7.06 ± 0.41	3
Arp 220	2001-08-11T23:36:03	67.B-0332(A)	L'	600	0.45	≤ 0.36	12.43 ± 0.52	0
Arp 220	2001-08-11T23:51:35	67.B-0332(A)	$M_{\rm nb}$	480	0.45	≤ 2.99	≤ 2.55	3
Arp 220	2001-08-12T00:04:32	67.B-0332(A)	$M_{\rm nb}$	480	0.45	2.40 ± 0.33	≤ 3.05	0
CGCG381-051	2003-06-20T10:04:01	71.B-0379(A)	L'	600	0.61	≤ 0.29	≤ 0.25	1
Cen A	2000-07-13T00:50:45	65.P-0519(A)	$M_{\rm nb}$	720	0.56	224.41 ± 13.50	182.84 ± 51.80	0
Cen A	2010-04-09T05:05:29	085.B-0639(A)	L'	118	0.36	261.69 ± 19.58	171.32 ± 74.21	0
Cen A	2013-07-03T02:06:00	290.B-5113(A)	L'	118	0.41	263.97 ± 16.50	≤ 0.82	0
Cen A	2013-07-03T02:10:07	290.B-5113(A)	$M_{\rm nb}$	118	0.42	305.82 ± 18.28	214.63 ± 82.72	0
Circinus	2000-06-22T01:01:03	65.P-0519(A)	$M_{\rm nb}$	1200	0.50	676.41 ± 44.58	594.97 ± 211.14	0
Circinus	2001-06-09T01:23:22	67.B-0332(A)	L'	600	0.63	458.16 ± 39.18	345.07 ± 158.43	0
Circinus	2001-06-09T01:38:47	67.B-0332(A)	$M_{\rm nb}$	480	0.56	811.51 ± 109.62	≤ 4.49	0
ESO 103-35	2013-06-26T07:59:58	290.B-5113(A)	L'	118	0.78	18.06 ± 1.97	22.66 ± 6.85	0
ESO 103-35	2013-06-26T08:04:05	290.B-5113(A)	$M_{\rm nb}$	236	0.72	40.67 ± 4.73	≤ 4.06	0

Table 5 *continued*

Table 5 *(continued)*

Target Name	Obs. Date	Obs. Program	Filter	Exp. Time	PSF FWHM	Nuc. Flux	Ext. Flux	Flag
				sec	"	[mJy]	[mJy]	
ESO 138-1	2013-06-27T03:21:47	290.B-5113(A)	L'	118	0.47	50.90 ± 3.45	51.66 ± 16.89	0
ESO 138-1	2013-06-27T03:25:53	290.B-5113(A)	$M_{\rm nb}$	118	0.36	30.43 ± 6.20	82.40 ± 21.42	0
ESO 138-1	2013-07-03T04:38:50	290.B-5113(A)	L'	118	0.41	64.62 ± 3.23	42.92 ± 12.28	0
ESO 138-1	2013-07-03T04:43:01	290.B-5113(A)	$M_{\rm nb}$	118	0.42	94.10 ± 4.80	39.54 ± 16.81	0
ESO 141-55	2013-06-26T08:25:56	290.B-5113(A)	L'	118	0.78	46.85 ± 2.52	37.00 ± 9.02	0
ESO 141-55	2013-06-26T08:30:05	290.B-5113(A)	$M_{\rm nb}$	236	0.72	53.51 ± 4.11	29.64 ± 13.94	0
ESO 286-19	2013-06-26T09:46:44	290.B-5113(A)	L'	118	0.67	5.23 ± 0.33	≤ 0.57	0
ESO 286-19	2013-06-26T09:50:55	290.B-5113(A)	$M_{\rm nb}$	236	0.65	16.33 ± 0.61	≤ 4.03	0
ESO 323-32	2013-07-03T01:01:33	290.B-5113(A)	L'	118	0.53	3.47 ± 0.12	≤ 0.64	0
ESO 323-32	2013-07-03T01:05:43	290.B-5113(A)	$M_{\rm nb}$	236	0.43	2.04 ± 0.35	≤ 3.82	3
ESO 323-77	2013-07-04T01:15:28	290.B-5113(A)	L'	118	0.32	159.61 ± 9.27	≤ 0.65	0
ESO 323-77	2013-07-04T01:19:36	290.B-5113(A)	$M_{\rm nb}$	118	0.30	119.07 ± 10.12	114.69 ± 39.73	0
ESO 506-27	2013-06-27T02:41:19	290.B-5113(A)	L'	118	0.47	7.89 ± 1.44	≤ 0.62	0
ESO 506-27	2013-06-27T02:45:27	290.B-5113(A)	$M_{\rm nb}$	236	0.36	≤ 4.13	14.73 ± 2.79	0
ESO 506-27	2013-07-06T01:47:44	290.B-5113(A)	L'	118	0.55	10.56 ± 0.87	8.95 ± 3.78	0
ESO 506-27	2013-07-06T01:51:48	290.B-5113(A)	$M_{\rm nb}$	236	0.64	23.32 ± 0.89	≤ 4.32	0
ESO 511-30	2013-07-06T02:10:20	290.B-5113(A)	L'	118	0.73	14.23 ± 0.57	≤ 0.59	0
ESO 511-30	2013-07-06T02:14:28	290.B-5113(A)	$M_{\rm nb}$	236	0.74	13.65 ± 0.66	≤ 4.07	0
Fairall 9	2003-08-17T06:01:03	71.B-0379(A)	$M_{\rm nb}$	1200	0.53	25.74 ± 2.99	25.17 ± 11.49	0
Fairall 49	2013-06-26T07:48:34	290.B-5113(A)	L'	118	0.78	52.25 ± 5.24	75.45 ± 21.23	0
Fairall 49	2013-06-26T07:52:45	290.B-5113(A)	$M_{\rm nb}$	118	0.72	62.60 ± 7.74	87.04 ± 26.79	0
Fairall 51	2013-06-26T08:14:21	290.B-5113(A)	L'	118	0.78	36.03 ± 4.05	53.01 ± 15.93	0
Fairall 51	2013-06-26T08:18:27	290.B-5113(A)	$M_{\rm nb}$	118	0.72	49.31 ± 5.57	38.76 ± 16.41	0
IC 3639	2003-07-05T01:00:12	70.B-0393(B)	L'	590	0.46	0.06 ± 0.01	107.99 ± 15.03	3
IC 3639	2003-07-05T01:17:26	70.B-0393(B)	$M_{\rm nb}$	1180	0.57	0.61 ± 0.07	≤ 145.29	3
IC 3639	2003-07-15T00:48:05	70.B-0393(B)	L'	600	0.47	15.38 ± 0.66	10.88 ± 2.61	0
IC 3639	2003-07-15T01:08:01	70.B-0393(B)	$M_{\rm nb}$	1200	0.55	25.73 ± 1.39	9.14 ± 4.30	0
IC 4329A	2013-07-06T02:00:20	290.B-5113(A)	L'	118	0.73	186.10 ± 7.07	60.91 ± 26.08	0
IC 4329A	2013-07-06T02:04:28	290.B-5113(A)	$M_{\rm nb}$	118	0.74	231.37 ± 9.78	≤ 5.83	0
IC 4518W	2013-07-06T02:53:30	290.B-5113(A)	L'	118	0.73	18.81 ± 1.41	10.98 ± 4.63	1
IC 4518W	2013-07-06T02:57:40	290.B-5113(A)	$M_{\rm nb}$	236	0.74	35.44 ± 1.28	≤ 4.34	1
IC 5063	2001-06-24T10:33:18	67.B-0332(A)	L'	60	0.64	119.87 ± 28.70	231.57 ± 72.47	1
IC 5063	2001-06-24T10:39:23	67.B-0332(A)	L'	600	0.64	259.46 ± 20.78	≤ 1.41	0
IC 5063	2001-07-19T04:23:41	67.B-0332(A)	L'	600	0.83	58.92 ± 2.42	18.26 ± 8.55	0
IC 5063	2001-07-19T04:40:43	67.B-0332(A)	L'	600	0.83	57.60 ± 2.18	22.68 ± 8.54	1
IC 5063	2001-07-19T04:56:37	67.B-0332(A)	$M_{\rm nb}$	480	0.53	49.81 ± 6.29	52.15 ± 20.36	1
IC 5063	2001-08-17T04:32:31	67.B-0332(A)	L'	600	0.41	31.93 ± 2.50	30.11 ± 12.11	0
IC 5063	2001-08-17T04:48:50	67.B-0332(A)	$M_{\rm nb}$	480	0.40	55.95 ± 6.96	≤ 1.99	0
IC 5063	2003-07-14T05:36:14	71.B-0379(A)	L'	600	0.50	33.13 ± 2.25	31.70 ± 10.57	0
IC 5063	2003-07-14T05:56:11	71.B-0379(A)	$M_{\rm nb}$	1200	0.50	53.10 ± 6.33	≤ 1.24	0
IC 5063	2004-10-31T00:06:54	074.B-0166(A)	L'	1534	0.45	16.59 ± 1.92	39.34 ± 6.41	0
IC 5179	2000-08-13T05:14:52	65.P-0519(A)	$M_{\rm nb}$	720	0.63	≤ 2.19	≤ 1.89	3
IRAS 13349+2438	2013-07-02T01:20:04	290.B-5113(A)	L'	118	0.54	133.40 ± 11.12	≤ 0.66	0
IRAS 13349+2438	2013-07-02T01:24:12	290.B-5113(A)	$M_{\rm nb}$	236	0.52	120.27 ± 12.79	110.77 ± 44.54	0
IRASF00198-7926	2003-08-17T05:40:25	71.B-0379(A)	L'	600	0.50	11.10 ± 1.93	22.90 ± 5.89	0
LEDA 170194	2013-07-07T00:25:15	290.B-5113(A)	L'	236	0.46	3.09 ± 0.22	≤ 0.44	0

Table 5 *continued*

Table 5 *(continued)*

Target Name	Obs. Date	Obs. Program	Filter	Exp. Time	PSF FWHM	Nuc. Flux	Ext. Flux	Flag
				sec	"	[mJy]	[mJy]	
LEDA 170194	2013-07-07T00:32:02	290.B-5113(A)	$M_{\rm nb}$	472	0.42	3.09 ± 0.25	≤ 2.60	0
LHS2397A	2013-07-01T00:16:09	60.A-9021(A)	L'	118	0.79	30.11 ± 1.37	≤ 0.68	0
LHS2397A	2013-07-01T00:20:16	60.A-9021(A)	$M_{\rm nb}$	118	0.85	8.74 ± 0.68	≤ 5.44	0
M87	2011-05-18T01:19:07	085.B-0639(A)	L'	118	0.37	6.41 ± 0.24	≤ 0.55	0
M87	2011-05-18T01:23:26	085.B-0639(A)	$M_{\rm nb}$	118	0.34	2.69 ± 0.24	≤ 4.26	0
MCG+2-4-25	2000-11-06T02:56:37	65.P-0519(A)	$M_{\rm nb}$	720	0.46	7.34 ± 1.92	≤ 1.88	0
MCG-0-29-23	2003-06-19T02:04:38	70.B-0393(B)	L'	600	0.54	2.74 ± 0.18	9.36 ± 0.81	0
MCG-0-29-23	2003-06-19T02:27:07	70.B-0393(B)	$M_{\rm nb}$	690	0.63	3.07 ± 0.30	≤ 2.15	0
MCG-0-29-23	2003-07-15T23:22:13	70.B-0393(B)	L'	600	0.58	4.87 ± 0.17	13.48 ± 1.43	0
MCG-0-29-23	2003-07-15T23:42:01	70.B-0393(B)	$M_{\rm nb}$	1200	0.49	6.00 ± 0.48	≤ 1.79	0
MCG-3-34-64	2003-07-15T02:00:36	70.B-0393(B)	L'	600	0.47	23.62 ± 1.68	33.84 ± 8.19	0
MCG-3-34-64	2003-07-15T02:20:20	70.B-0393(B)	$M_{\rm nb}$	1200	0.55	39.81 ± 5.47	58.19 ± 20.87	0
MCG-3-34-64	2013-07-01T00:39:39	290.B-5113(A)	L'	118	0.79	57.09 ± 3.31	≤ 0.61	0
MCG-3-34-64	2013-07-01T00:43:46	290.B-5113(A)	$M_{\rm nb}$	236	0.85	102.12 ± 6.80	≤ 3.96	0
MCG-6-30-15	2013-07-04T01:50:12	290.B-5113(A)	L'	118	0.32	65.23 ± 4.07	≤ 0.57	0
MCG-6-30-15	2013-07-04T01:54:20	290.B-5113(A)	$M_{\rm nb}$	118	0.30	56.78 ± 6.75	54.46 ± 24.78	0
Mrk 331	2000-11-06T23:39:11	65.P-0519(A)	$M_{\rm nb}$	480	0.41	≤ 2.42	3.67 ± 1.32	3
Mrk 463	2003-07-20T01:09:13	70.B-0393(B)	L'	600	0.58	68.53 ± 9.56	102.17 ± 45.35	0
Mrk 463	2003-07-20T01:29:08	70.B-0393(B)	$M_{\rm nb}$	1200	0.49	35.55 ± 7.96	125.28 ± 27.46	0
Mrk 509	2013-07-03T05:25:31	290.B-5113(A)	L'	118	0.41	108.47 ± 4.81	≤ 0.56	0
Mrk 509	2013-07-03T05:29:39	290.B-5113(A)	$M_{\rm nb}$	236	0.42	117.10 ± 5.40	≤ 3.49	0
Mrk 841	2013-07-07T02:37:13	290.B-5113(A)	L'	118	0.46	14.58 ± 1.48	9.97 ± 4.44	0
Mrk 841	2013-07-07T02:41:20	290.B-5113(A)	$M_{\rm nb}$	236	0.42	23.03 ± 1.46	≤ 3.56	0
Mrk 897	2003-06-22T09:25:23	71.B-0379(A)	L'	480	0.69	1.74 ± 0.10	2.79 ± 0.51	1
Mrk 897	2003-06-22T09:44:18	71.B-0379(A)	L'	180	0.69	7.42 ± 0.47	≤ 0.50	1
Mrk 897	2003-06-22T09:51:58	71.B-0379(A)	$M_{\rm nb}$	450	0.66	≤ 6.16	≤ 5.77	1
Mrk 897	2003-06-22T10:11:47	71.B-0379(A)	$M_{\rm nb}$	120	0.66	≤ 9.10	≤ 8.52	3
NGC 63	2000-11-07T00:06:36	65.P-0519(A)	$M_{\rm nb}$	2880	0.41	0.71 ± 0.10	≤ 0.82	2
NGC 253	2000-09-17T07:53:06	65.P-0519(A)	L'	144	0.57	78.77 ± 2.68	82.78 ± 10.98	0
NGC 253	2000-09-17T07:58:33	65.P-0519(A)	$M_{\rm nb}$	288	0.54	119.08 ± 4.88	88.08 ± 41.32	0
NGC 253	2000-09-17T08:09:44	65.P-0519(A)	$M_{\rm nb}$	288	0.54	121.74 ± 4.86	88.80 ± 27.73	0
NGC 253	2003-06-23T09:58:42	71.B-0404(A)	L'	330	0.69	97.21 ± 5.42	44.23 ± 12.19	0
NGC 253	2003-06-23T10:12:21	71.B-0404(A)	L'	330	0.69	95.78 ± 5.13	48.67 ± 12.02	1
NGC 253	2003-06-23T10:24:29	71.B-0404(A)	$M_{\rm nb}$	90	0.35	72.42 ± 5.92	98.43 ± 25.32	1
NGC 253	2003-06-23T10:31:37	71.B-0404(A)	$M_{\rm nb}$	300	0.35	93.98 ± 7.70	102.75 ± 31.10	0
NGC 253	2003-06-23T10:45:17	71.B-0404(A)	$M_{\rm nb}$	300	0.35	68.31 ± 6.68	117.05 ± 21.71	0
NGC 424	2003-08-17T06:54:30	71.B-0379(A)	L'	600	0.50	203.46 ± 7.91	≤ 0.27	0
NGC 424	2003-08-17T07:14:03	71.B-0379(A)	$M_{\rm nb}$	1200	0.53	225.63 ± 8.14	82.03 ± 33.21	0
NGC 520	2000-11-06T03:19:58	65.P-0519(A)	$M_{\rm nb}$	720	0.46	≤ 2.32	8.50 ± 0.62	2
NGC 660	2000-11-05T04:51:21	65.P-0519(A)	$M_{\rm nb}$	960	0.47	≤ 2.09	14.42 ± 0.81	2
NGC 986	2000-09-20T04:22:26	65.P-0519(A)	$M_{\rm nb}$	864	0.91	4.72 ± 0.53	≤ 3.73	3
NGC 1008	2001-07-19T09:30:52	67.B-0332(A)	L'	120	0.58	≤ 0.59	≤ 0.52	3
NGC 1008	2001-08-15T06:32:11	67.B-0332(A)	L'	600	0.60	≤ 0.13	1.69 ± 0.19	2
NGC 1008	2001-08-15T06:48:27	67.B-0332(A)	$M_{\rm nb}$	480	0.59	≤ 2.94	≤ 2.70	3
NGC 1068	2001-08-15T07:04:46	67.B-0332(A)	L'	600	0.60	0.17 ± 0.03	≤ 0.23	2
NGC 1068	2001-08-15T07:25:13	67.B-0332(A)	L'	600	0.60	1940.88 ± 241.52	1876.65 ± 822.79	0

Table 5 *continued*

Table 5 *(continued)*

Target Name	Obs. Date	Obs. Program	Filter	Exp. Time	PSF FWHM	Nuc. Flux	Ext. Flux	Flag
				sec	"	[mJy]	[mJy]	
NGC 1068	2001-08-15T07:41:27	67.B-0332(A)	$M_{\rm nb}$	480	0.59	2687.53 ± 374.86	4267.02 ± 1471.36	0
NGC 1068	2004-10-31T03:10:43	074.B-0166(A)	L'	1534	0.45	886.54 ± 124.82	2272.66 ± 387.63	0
NGC 1097	2003-08-17T08:04:24	71.B-0379(A)	L'	600	0.49	5.55 ± 0.24	8.30 ± 1.40	0
NGC 1097	2003-08-17T08:24:12	71.B-0379(A)	$M_{\rm nb}$	1200	0.53	5.63 ± 0.51	≤ 1.84	0
NGC 1097	2004-10-30T03:50:42	074.B-0166(A)	L'	1534	0.57	6.93 ± 0.28	8.08 ± 1.15	0
NGC 1097	2004-10-31T03:52:44	074.B-0166(A)	L'	1534	0.45	4.40 ± 0.23	8.91 ± 1.17	0
NGC 1125	2003-08-17T09:12:29	71.B-0379(A)	L'	600	0.43	3.51 ± 0.23	5.95 ± 1.25	0
NGC 1125	2003-08-17T09:32:10	71.B-0379(A)	$M_{\rm nb}$	1200	0.53	6.76 ± 0.46	≤ 1.49	0
NGC 1368	2004-10-30T04:53:33	074.B-0166(A)	L'	1534	0.57	0.67 ± 0.06	4.34 ± 0.34	0
NGC 1365	2003-12-02T00:31:01	072.B-0397(A)	L'	590	0.65	196.44 ± 6.58	≤ 0.40	0
NGC 1365	2003-12-02T00:47:54	072.B-0397(A)	$M_{\rm nb}$	944	0.64	152.32 ± 6.74	≤ 1.58	0
NGC 1386	2000-09-17T09:45:17	65.P-0519(A)	$M_{\rm nb}$	576	0.54	29.31 ± 2.29	18.98 ± 8.69	0
NGC 1386	2010-08-25T07:51:23	085.B-0639(A)	L'	118	0.50	18.65 ± 0.98	21.13 ± 4.93	0
NGC 1511	2000-09-17T08:49:45	65.P-0519(A)	$M_{\rm nb}$	1152	0.54	2.44 ± 0.17	≤ 1.41	1
NGC 1566	2004-10-30T06:03:36	074.B-0166(A)	L'	1534	0.57	10.55 ± 0.38	11.02 ± 1.83	0
NGC 1614	2000-09-17T08:25:55	65.P-0519(A)	$M_{\rm nb}$	576	0.54	7.13 ± 0.65	15.58 ± 2.04	0
NGC 1667	2004-10-30T07:07:28	074.B-0166(A)	L'	590	0.57	1.48 ± 0.08	2.03 ± 0.39	0
NGC 1667	2004-10-30T08:14:46	074.B-0166(A)	L'	944	0.57	1.47 ± 0.07	2.87 ± 0.37	0
NGC 1808	2000-09-15T08:37:55	65.P-0519(A)	L'	536	0.44	6.29 ± 0.51	15.65 ± 2.15	0
NGC 1808	2000-09-15T08:50:51	65.P-0519(A)	L'	144	0.44	6.40 ± 0.54	15.28 ± 2.15	0
NGC 1808	2000-09-15T08:56:33	65.P-0519(A)	L'	144	0.44	10.09 ± 0.64	22.79 ± 2.57	0
NGC 1808	2000-09-15T09:08:10	65.P-0519(A)	$M_{\rm nb}$	288	0.47	9.90 ± 0.73	10.01 ± 2.60	0
NGC 1808	2003-12-02T02:39:44	072.B-0397(A)	L'	590	0.65	19.13 ± 0.90	23.88 ± 3.04	0
NGC 1808	2003-12-02T02:56:17	072.B-0397(A)	$M_{\rm nb}$	944	0.64	10.46 ± 0.56	8.94 ± 2.04	0
NGC 3125	2010-06-06T23:43:17	085.B-0639(A)	L'	118	0.33	≤ 0.75	≤ 0.58	3
NGC 3125	2010-06-06T23:47:05	085.B-0639(A)	$M_{\rm nb}$	354	0.37	≤ 3.47	≤ 3.00	3
NGC 3281	2001-06-02T22:52:59	65.P-0519(A)	$M_{\rm nb}$	240	0.57	116.64 ± 5.26	≤ 4.67	0
NGC 3660	2003-06-19T00:26:28	70.B-0393(B)	L'	600	0.54	2.99 ± 0.13	≤ 0.24	0
NGC 3660	2003-06-19T00:49:09	70.B-0393(B)	$M_{\rm nb}$	1200	0.63	1.46 ± 0.15	≤ 1.33	0
NGC 4038/9	2001-06-03T01:51:39	65.P-0519(A)	$M_{\rm nb}$	2130	0.57	2.43 ± 0.26	≤ 1.79	3
NGC 4074	2013-06-30T23:31:45	290.B-5113(A)	L'	118	0.79	12.53 ± 0.84	≤ 0.65	0
NGC 4074	2013-06-30T23:35:56	290.B-5113(A)	$M_{\rm nb}$	236	0.85	10.04 ± 0.72	≤ 4.07	0
NGC 4235	2011-05-18T00:26:00	085.B-0639(A)	L'	118	1.58	17.23 ± 0.94	≤ 0.61	0
NGC 4235	2011-05-18T00:31:15	085.B-0639(A)	$M_{\rm nb}$	118	0.47	5.71 ± 1.15	8.66 ± 2.07	0
NGC 4235	2011-05-18T00:34:53	085.B-0639(A)	L'	118	0.47	14.49 ± 0.97	11.90 ± 3.98	0
NGC 4253	2013-06-30T23:17:03	290.B-5113(A)	L'	118	0.79	23.99 ± 6.38	32.16 ± 15.01	0
NGC 4253	2013-06-30T23:21:10	290.B-5113(A)	$M_{\rm nb}$	236	0.85	39.53 ± 2.28	≤ 4.23	0
NGC 4261	2011-05-18T00:55:02	085.B-0639(A)	L'	118	0.32	0.64 ± 0.06	5.11 ± 0.50	0
NGC 4261	2011-05-18T00:59:17	085.B-0639(A)	$M_{\rm nb}$	118	0.31	≤ 5.83	≤ 4.99	3
NGC 4278	2013-07-05T23:18:17	290.B-5113(A)	L'	236	0.50	≤ 0.57	10.39 ± 0.49	0
NGC 4278	2013-07-05T23:25:00	290.B-5113(A)	$M_{\rm nb}$	708	0.45	≤ 2.65	≤ 2.37	3
NGC 4303	2003-05-29T00:50:21	71.B-0404(A)	L'	590	1.41	4.01 ± 0.19	4.37 ± 0.63	0
NGC 4303	2003-05-29T01:08:30	71.B-0404(A)	$M_{\rm nb}$	600	1.37	≤ 1.89	≤ 1.99	3
NGC 4303	2013-07-06T00:22:55	290.B-5113(A)	L'	354	0.55	1.65 ± 0.13	5.87 ± 0.67	0
NGC 4303	2013-07-06T00:32:36	290.B-5113(A)	$M_{\rm nb}$	472	0.64	≤ 4.07	11.49 ± 2.01	1
NGC 4374	2013-06-27T01:30:13	290.B-5113(A)	L'	472	0.47	0.15 ± 0.05	7.14 ± 0.39	0

Table 5 *continued*

Table 5 *(continued)*

Target Name	Obs. Date	Obs. Program	Filter	Exp. Time	PSF FWHM	Nuc. Flux	Ext. Flux	Flag
				sec	"	[mJy]	[mJy]	
NGC 4374	2013-06-27T01:42:37	290.B-5113(A)	$M_{\rm nb}$	944	0.36	≤ 2.21	≤ 1.92	3
NGC 4374	2013-07-04T00:33:33	290.B-5113(A)	L'	472	0.35	0.33 ± 0.04	7.73 ± 0.39	0
NGC 4388	2013-06-30T23:45:37	290.B-5113(A)	L'	354	0.79	34.11 ± 1.23	≤ 0.41	0
NGC 4388	2013-06-30T23:55:22	290.B-5113(A)	$M_{\rm nb}$	708	0.85	44.11 ± 2.10	≤ 2.39	0
NGC 4418	2013-07-02T01:07:01	290.B-5113(A)	L'	118	0.54	2.03 ± 0.20	1.68 ± 0.78	0
NGC 4418	2013-07-02T01:11:04	290.B-5113(A)	$M_{\rm nb}$	236	0.52	6.26 ± 0.61	≤ 4.17	0
NGC 4438	2013-03-05T08:53:11	290.B-5113(A)	L'	118	0.54	4.04 ± 0.26	12.56 ± 1.45	0
NGC 4438	2013-03-05T08:58:35	290.B-5113(A)	$M_{\rm nb}$	236	0.51	2.20 ± 0.42	≤ 4.84	3
NGC 4457	2013-07-07T00:06:51	290.B-5113(A)	L'	118	0.46	3.00 ± 0.23	15.51 ± 1.23	0
NGC 4457	2013-07-07T00:13:54	290.B-5113(A)	$M_{\rm nb}$	236	0.42	≤ 4.30	≤ 3.62	3
NGC 4472	2013-07-03T23:31:28	290.B-5113(A)	L'	472	0.35	≤ 0.41	4.97 ± 0.32	2
NGC 4472	2013-07-03T23:43:58	290.B-5113(A)	$M_{\rm nb}$	944	0.32	≤ 2.09	≤ 1.79	3
NGC 4501	2003-07-16T00:30:23	70.B-0393(B)	L'	600	0.58	1.50 ± 0.16	13.68 ± 1.17	0
NGC 4501	2003-07-16T00:50:14	70.B-0393(B)	$M_{\rm nb}$	660	0.49	≤ 0.76	≤ 2.26	3
NGC 4507	2013-06-27T02:25:01	290.B-5113(A)	L'	118	0.47	59.67 ± 5.96	51.83 ± 24.55	0
NGC 4507	2013-06-27T02:29:08	290.B-5113(A)	$M_{\rm nb}$	118	0.36	62.07 ± 12.71	≤ 5.72	0
NGC 4507	2013-07-06T01:37:43	290.B-5113(A)	L'	118	0.55	62.47 ± 6.80	57.66 ± 23.97	0
NGC 4507	2013-07-06T01:41:52	290.B-5113(A)	$M_{\rm nb}$	118	0.64	88.16 ± 8.83	60.73 ± 28.93	0
NGC 4579	2011-05-18T01:43:50	085.B-0639(A)	L'	118	0.31	16.91 ± 0.66	17.10 ± 4.35	0
NGC 4579	2011-05-18T01:48:04	085.B-0639(A)	$M_{\rm nb}$	118	0.36	14.99 ± 1.02	7.20 ± 3.27	0
NGC 4593	2013-07-11T00:30:23	290.B-5113(A)	L'	118	0.39	32.31 ± 2.40	22.51 ± 10.48	0
NGC 4593	2013-07-11T00:34:33	290.B-5113(A)	$M_{\rm nb}$	236	0.40	36.16 ± 2.54	25.66 ± 7.17	0
NGC 4594	2013-07-07T01:20:48	290.B-5113(A)	L'	118	0.46	2.74 ± 0.32	38.94 ± 1.97	0
NGC 4594	2013-07-07T01:24:53	290.B-5113(A)	$M_{\rm nb}$	236	0.42	≤ 4.42	≤ 3.73	2
NGC 4746	2013-07-06T00:59:50	290.B-5113(A)	L'	472	0.55	≤ 0.42	0.56 ± 0.25	1
NGC 4746	2013-07-06T01:12:15	290.B-5113(A)	$M_{\rm nb}$	944	0.64	≤ 4.66	≤ 4.34	3
NGC 4785	2013-07-03T01:15:52	290.B-5113(A)	L'	472	0.53	1.11 ± 0.08	3.99 ± 0.56	0
NGC 4785	2013-07-03T01:28:23	290.B-5113(A)	$M_{\rm nb}$	944	0.42	≤ 2.17	≤ 1.90	2
NGC 4941	2003-07-16T01:59:58	70.B-0393(B)	$M_{\rm nb}$	1200	0.49	1.85 ± 0.19	≤ 1.91	0
NGC 4941	2003-07-16T02:39:22	70.B-0393(B)	$M_{\rm nb}$	420	0.49	2.01 ± 0.34	≤ 3.20	0
NGC 4941	2013-07-07T01:33:05	290.B-5113(A)	L'	118	0.46	4.54 ± 0.29	4.20 ± 1.36	0
NGC 4941	2013-07-07T01:37:12	290.B-5113(A)	$M_{\rm nb}$	236	0.42	2.15 ± 0.35	≤ 3.79	0
NGC 4945	2000-06-21T23:22:29	65.P-0519(A)	L'	120	0.50	≤ 2.05	65.02 ± 4.09	0
NGC 4945	2000-06-21T23:26:55	65.P-0519(A)	$M_{\rm nb}$	480	0.60	≤ 2.58	17.69 ± 1.47	3
NGC 4945	2000-06-21T23:38:17	65.P-0519(A)	L'	120	0.50	≤ 1.97	67.52 ± 4.19	0
NGC 4945	2000-06-21T23:42:43	65.P-0519(A)	$M_{\rm nb}$	480	0.60	≤ 2.91	20.34 ± 1.59	0
NGC 4945	2001-06-08T04:20:48	67.B-0332(A)	L'	600	0.65	≤ 2.13	54.70 ± 3.35	0
NGC 4945	2001-06-08T04:36:20	67.B-0332(A)	$M_{\rm nb}$	480	0.57	≤ 4.02	10.93 ± 2.05	2
NGC 5135	2003-07-15T02:59:34	70.B-0393(B)	L'	600	0.47	9.10 ± 0.58	12.31 ± 4.22	0
NGC 5135	2003-07-15T03:19:33	70.B-0393(B)	$M_{\rm nb}$	1200	0.55	15.16 ± 2.40	≤ 1.84	0
NGC 5135	2013-07-04T01:36:30	290.B-5113(A)	L'	118	0.32	12.63 ± 0.70	7.95 ± 3.34	0
NGC 5135	2013-07-04T01:40:36	290.B-5113(A)	$M_{\rm nb}$	236	0.30	19.31 ± 2.75	≤ 3.34	0
NGC 5252	2013-07-11T00:42:28	290.B-5113(A)	L'	118	0.39	16.17 ± 1.20	13.45 ± 4.88	0
NGC 5252	2013-07-11T00:46:33	290.B-5113(A)	$M_{\rm nb}$	236	0.40	25.19 ± 1.31	≤ 4.37	0
NGC 5252	2013-07-24T00:48:30	290.B-5113(A)	L'	118	0.39	≤ 0.94	23.62 ± 1.45	0
NGC 5252	2013-07-24T00:52:35	290.B-5113(A)	$M_{\rm nb}$	236	0.40	≤ 5.00	18.04 ± 2.50	0

Table 5 *continued*

Table 5 *(continued)*

Target Name	Obs. Date	Obs. Program	Filter	Exp. Time	PSF FWHM	Nuc. Flux	Ext. Flux	Flag
				sec	"	[mJy]	[mJy]	
NGC 5363	2013-07-07T01:46:06	290.B-5113(A)	L'	118	0.46	0.97 ± 0.12	8.36 ± 0.67	0
NGC 5363	2013-07-07T01:50:12	290.B-5113(A)	$M_{\rm nb}$	236	0.42	≤ 4.72	≤ 3.98	3
NGC 5427	2013-07-02T01:34:40	290.B-5113(A)	L'	472	0.54	2.95 ± 0.10	≤ 0.31	0
NGC 5427	2013-07-02T01:47:12	290.B-5113(A)	$M_{\rm nb}$	944	0.52	2.09 ± 0.26	≤ 1.90	2
NGC 5506	2003-07-13T23:33:47	71.B-0404(A)	L'	600	0.46	343.79 ± 12.95	124.02 ± 50.48	0
NGC 5506	2003-07-13T23:53:28	71.B-0404(A)	$M_{\rm nb}$	60	0.57	359.44 ± 26.41	150.89 ± 47.07	0
NGC 5548	2013-07-24T00:22:19	290.B-5113(A)	L'	118	0.39	3.29 ± 0.89	59.13 ± 3.82	0
NGC 5548	2013-07-24T00:26:23	290.B-5113(A)	$M_{\rm nb}$	236	0.40	≤ 4.99	51.91 ± 2.65	0
NGC 5643	2013-07-04T02:16:55	290.B-5113(A)	L'	118	0.32	8.56 ± 0.45	10.99 ± 2.42	0
NGC 5643	2013-07-04T02:21:04	290.B-5113(A)	$M_{\rm nb}$	236	0.30	14.11 ± 1.55	≤ 3.35	0
NGC 5728	2013-07-06T02:39:55	290.B-5113(A)	L'	118	0.73	2.89 ± 0.22	2.93 ± 1.12	0
NGC 5728	2013-07-06T02:44:04	290.B-5113(A)	$M_{\rm nb}$	236	0.74	2.76 ± 0.33	≤ 4.33	0
NGC 5813	2013-07-07T01:58:27	290.B-5113(A)	L'	472	0.46	≤ 0.38	6.57 ± 0.34	0
NGC 5813	2013-07-07T02:10:54	290.B-5113(A)	$M_{\rm nb}$	944	0.42	≤ 2.06	≤ 1.74	1
NGC 5953	2001-06-10T02:46:05	67.B-0332(A)	L'	600	0.95	1.60 ± 0.17	2.71 ± 0.59	0
NGC 5953	2001-06-10T03:02:24	67.B-0332(A)	$M_{\rm nb}$	480	0.81	≤ 4.43	≤ 3.91	3
NGC 5953	2003-05-31T05:14:11	70.B-0393(B)	L'	590	1.41	6.01 ± 0.63	≤ 0.26	1
NGC 5953	2003-05-31T05:32:20	70.B-0393(B)	$M_{\rm nb}$	450	1.37	≤ 6.36	≤ 6.69	3
NGC 5953	2003-06-01T05:31:44	70.B-0393(B)	L'	590	1.41	4.39 ± 0.33	3.67 ± 1.07	1
NGC 5953	2003-06-01T05:49:46	70.B-0393(B)	$M_{\rm nb}$	1200	1.37	≤ 1.65	≤ 1.74	3
NGC 5953	2003-07-16T03:18:09	70.B-0393(B)	L'	600	0.58	0.68 ± 0.12	9.63 ± 0.84	1
NGC 5953	2003-07-16T03:37:56	70.B-0393(B)	$M_{\rm nb}$	1200	0.49	≤ 1.59	≤ 1.66	3
NGC 5953	2013-07-07T02:51:22	290.B-5113(A)	L'	472	0.46	0.54 ± 0.09	7.25 ± 0.50	1
NGC 5953	2013-07-07T03:03:48	290.B-5113(A)	$M_{\rm nb}$	944	0.42	≤ 2.29	≤ 1.93	3
NGC 5995	2003-06-19T04:49:17	70.B-0393(B)	L'	600	0.56	60.09 ± 3.02	44.62 ± 13.35	0
NGC 5995	2003-06-19T05:11:47	70.B-0393(B)	$M_{\rm nb}$	1200	0.46	54.06 ± 4.99	53.44 ± 19.25	0
NGC 6000	2000-08-15T00:21:24	65.P-0519(A)	$M_{\rm nb}$	960	0.53	2.72 ± 0.46	13.36 ± 1.71	0
NGC 6221	2013-07-03T04:48:31	290.B-5113(A)	L'	118	0.41	12.53 ± 0.47	12.80 ± 2.95	0
NGC 6221	2013-07-03T04:52:39	290.B-5113(A)	$M_{\rm nb}$	236	0.42	11.30 ± 0.62	≤ 3.67	0
NGC 6240N	2000-07-13T03:00:50	65.P-0519(A)	L'	240	0.99	16.65 ± 0.56	12.41 ± 1.48	0
NGC 6240N	2000-07-13T03:08:55	65.P-0519(A)	$M_{\rm nb}$	720	0.68	18.47 ± 0.68	≤ 1.79	0
NGC 6300	2013-07-02T04:57:16	290.B-5113(A)	L'	118	0.54	31.34 ± 1.73	19.64 ± 8.69	0
NGC 6300	2013-07-02T05:01:22	290.B-5113(A)	$M_{\rm nb}$	118	0.52	49.80 ± 2.54	≤ 5.92	0
NGC 6810	2003-07-14T04:22:03	71.B-0379(A)	L'	150	0.36	7.10 ± 0.56	28.41 ± 2.52	0
NGC 6810	2003-07-14T04:29:43	71.B-0379(A)	L'	600	0.36	10.10 ± 0.55	26.71 ± 2.84	0
NGC 6810	2003-07-14T04:47:59	71.B-0379(A)	$M_{\rm nb}$	1200	0.43	4.85 ± 0.51	10.06 ± 1.98	0
NGC 6814	2000-08-13T04:25:33	65.P-0519(A)	$M_{\rm nb}$	720	0.63	23.15 ± 1.92	≤ 1.76	0
NGC 6814	2013-07-03T05:12:02	290.B-5113(A)	L'	118	0.41	10.57 ± 0.40	5.39 ± 1.44	0
NGC 6814	2013-07-03T05:16:10	290.B-5113(A)	$M_{\rm nb}$	236	0.42	12.04 ± 0.69	≤ 3.35	0
NGC 6860	2013-06-26T08:39:54	290.B-5113(A)	L'	118	0.78	35.24 ± 1.50	15.08 ± 4.98	0
NGC 6860	2013-06-26T08:44:01	290.B-5113(A)	$M_{\rm nb}$	236	0.72	39.72 ± 2.47	≤ 4.07	0
NGC 6890	2003-07-14T06:50:47	71.B-0379(A)	L'	600	0.50	8.12 ± 0.35	6.79 ± 1.56	0
NGC 6890	2003-07-14T07:10:58	71.B-0379(A)	$M_{\rm nb}$	1200	0.50	9.45 ± 0.66	≤ 1.23	0
NGC 6890	2004-10-30T00:07:52	074.B-0166(A)	L'	1534	0.57	6.14 ± 0.61	7.98 ± 2.20	0
NGC 7130	2003-08-12T03:10:03	71.B-0379(A)	L'	600	0.60	6.91 ± 0.30	7.75 ± 1.15	0
NGC 7130	2003-08-12T03:29:58	71.B-0379(A)	$M_{\rm nb}$	1200	0.55	14.39 ± 0.75	≤ 1.80	0

Table 5 *continued*

Table 5 *(continued)*

Target Name	Obs. Date	Obs. Program	Filter	Exp. Time	PSF FWHM	Nuc. Flux	Ext. Flux	Flag
				sec	"	[mJy]	[mJy]	
NGC 7172	2001-06-09T09:38:20	67.B-0332(A)	L'	210	0.95	37.80 ± 7.16	46.56 ± 19.09	1
NGC 7172	2001-06-09T09:48:16	67.B-0332(A)	L'	600	0.95	54.89 ± 3.02	37.55 ± 11.43	1
NGC 7172	2001-06-09T10:03:39	67.B-0332(A)	$M_{\rm nb}$	480	0.81	61.82 ± 3.30	≤ 3.30	1
NGC 7172	2004-10-30T01:27:32	074.B-0166(A)	L'	1534	0.57	48.96 ± 1.92	31.79 ± 7.59	0
NGC 7213	2000-08-13T05:44:26	65.P-0519(A)	$M_{\rm nb}$	240	0.72	≤ 3.39	≤ 2.98	3
NGC 7314	2000-08-13T04:53:57	65.P-0519(A)	$M_{\rm nb}$	480	0.63	18.47 ± 0.83	≤ 2.39	0
NGC 7314	2004-10-31T01:17:55	074.B-0166(A)	L'	1534	0.45	7.94 ± 0.43	6.82 ± 1.46	0
NGC 7479	2004-10-30T02:40:56	074.B-0166(A)	L'	1534	0.57	12.84 ± 0.58	10.03 ± 2.48	0
NGC 7496	2003-08-12T04:49:44	71.B-0379(A)	L'	90	0.60	4.20 ± 0.36	4.86 ± 1.35	0
NGC 7496	2003-08-12T04:59:19	71.B-0379(A)	L'	600	0.60	6.59 ± 0.26	4.67 ± 1.12	0
NGC 7496	2003-08-12T05:19:17	71.B-0379(A)	$M_{\rm nb}$	1200	0.55	6.89 ± 0.64	≤ 2.10	0
NGC 7552	2000-06-15T08:36:37	65.P-0519(A)	$M_{\rm nb}$	1440	0.78	≤ 1.66	2.44 ± 0.42	0
NGC 7552	2000-07-13T05:46:58	65.P-0519(A)	$M_{\rm nb}$	1404	0.55	≤ 2.13	≤ 1.86	0
NGC 7582	2000-08-13T05:55:46	65.P-0519(A)	$M_{\rm nb}$	240	0.72	69.95 ± 4.49	92.92 ± 21.84	0
NGC 7582	2001-07-19T08:06:45	67.B-0332(A)	L'	600	0.58	196.65 ± 7.49	59.53 ± 26.95	0
NGC 7582	2001-07-19T08:22:58	67.B-0332(A)	$M_{\rm nb}$	480	0.39	91.64 ± 5.08	81.68 ± 21.87	0
NGC 7582	2001-08-17T05:06:52	67.B-0332(A)	L'	600	0.40	107.81 ± 3.99	84.13 ± 22.80	0
NGC 7582	2001-08-17T05:23:17	67.B-0332(A)	$M_{\rm nb}$	480	0.37	96.60 ± 5.08	80.12 ± 24.98	0
NGC 7582	2003-08-17T04:30:43	71.B-0379(A)	L'	600	0.50	111.83 ± 8.31	88.53 ± 39.71	0
NGC 7582	2003-08-17T04:50:28	71.B-0379(A)	$M_{\rm nb}$	1200	0.53	101.52 ± 5.43	96.47 ± 26.76	0
NGC 7582	2004-10-31T02:27:17	074.B-0166(A)	L'	1534	0.45	85.10 ± 5.22	101.69 ± 28.71	0
NGC 7590	2003-07-15T06:11:02	71.B-0379(A)	L'	600	0.58	0.68 ± 0.05	3.99 ± 0.29	0
NGC 7590	2003-07-15T06:30:44	71.B-0379(A)	$M_{\rm nb}$	1200	0.49	≤ 1.79	≤ 1.62	3
NGC 7679	2003-06-23T09:14:46	71.B-0379(A)	$M_{\rm nb}$	600	0.35	≤ 2.84	≤ 2.36	3
PG 2130+099	2013-06-27T09:42:30	290.B-5113(A)	L'	118	0.68	17.64 ± 3.15	20.29 ± 9.73	0
PG 2130+099	2013-06-27T09:46:41	290.B-5113(A)	$M_{\rm nb}$	236	0.66	42.59 ± 1.76	≤ 4.37	0
PG 2130+099	2013-06-29T09:41:27	290.B-5113(A)	L'	118	0.78	30.34 ± 2.23	≤ 0.56	3
PG 2130+099	2013-06-29T09:48:09	290.B-5113(A)	$M_{\rm nb}$	236	0.80	39.94 ± 2.89	≤ 4.13	0
PG 2130+099	2013-06-29T09:58:29	290.B-5113(A)	L'	118	0.78	41.19 ± 2.51	≤ 0.62	0
PG 2130+099	2013-06-29T10:02:41	290.B-5113(A)	$M_{\rm nb}$	236	0.80	39.00 ± 2.61	≤ 3.99	0
PG 2130+099	2013-06-30T09:42:35	290.B-5113(A)	L'	118	0.78	42.95 ± 1.29	≤ 0.64	0
PG 2130+099	2013-06-30T09:46:46	290.B-5113(A)	$M_{\rm nb}$	236	0.80	44.28 ± 1.44	≤ 3.97	0
PKS 1417-19	2013-07-06T02:24:43	290.B-5113(A)	L'	118	0.73	6.20 ± 0.22	≤ 0.63	0
PKS 1417-19	2013-07-06T02:28:50	290.B-5113(A)	$M_{\rm nb}$	236	0.74	3.04 ± 0.40	≤ 4.02	2
PKS 1814-63	2013-07-02T05:22:22	290.B-5113(A)	L'	472	0.54	3.71 ± 0.12	≤ 0.36	0
PKS 1814-63	2013-07-02T05:34:51	290.B-5113(A)	$M_{\rm nb}$	944	0.52	2.09 ± 0.19	≤ 2.08	0
PKS 1932-46	2013-06-26T09:06:59	290.B-5113(A)	L'	472	0.78	≤ 0.33	≤ 0.29	3
PKS 1932-46	2013-06-26T09:19:25	290.B-5113(A)	$M_{\rm nb}$	944	0.72	≤ 2.02	≤ 1.94	3
Superantennae S	2003-06-19T08:22:54	71.B-0379(A)	L'	600	0.56	16.72 ± 0.81	9.34 ± 2.82	0
Superantennae S	2003-06-19T08:45:13	71.B-0379(A)	$M_{\rm nb}$	60	0.46	36.60 ± 1.69	≤ 5.93	0
Superantennae S	2003-06-21T08:19:13	71.B-0379(A)	$M_{\rm nb}$	780	0.66	30.18 ± 2.02	≤ 1.96	0
Superantennae S	2003-06-21T08:53:44	71.B-0379(A)	$M_{\rm nb}$	600	0.66	28.62 ± 1.78	19.23 ± 6.46	0
Superantennae S	2003-06-23T07:42:39	71.B-0379(A)	$M_{\rm nb}$	630	0.49	26.91 ± 1.52	17.36 ± 4.87	0
Superantennae S	2003-06-23T08:06:49	71.B-0379(A)	$M_{\rm nb}$	630	0.35	19.43 ± 2.37	23.88 ± 8.28	0
UGC 2369 S	2000-11-05T04:27:27	65.P-0519(A)	$M_{\rm nb}$	720	0.47	1.18 ± 0.11	≤ 1.85	3
Z 41-20	2013-07-03T00:47:57	290.B-5113(A)	L'	118	0.53	2.87 ± 0.13	≤ 0.66	0

Table 5 *continued*

Table 5 *(continued)*

Target Name	Obs. Date	Obs. Program	Filter	Exp. Time	PSF FWHM	Nuc. Flux	Ext. Flux	Flag
				sec	"	[mJy]	[mJy]	
Z 41-20	2013-07-03T00:52:05	290.B-5113(A)	M_{nb}	236	0.43	2.18 ± 0.34	≤ 3.92	2

NOTE—Epochs marked in bold are used in the analysis above, typically because of better seeing conditions. Flags: 0, no issue; 1, possible error in the reduction; 2, likely error in reduction (chopping/nodding); 3, failure in full chop/nod reduction.

A.1. *Special Cases*

A.1.1. *Arp 220 – A Known Double Nucleus*

Special care was taken for Arp 220 (a.k.a. IC4553) which is known to have a double nucleus (e.g., Soifer et al. 1999; Aalto et al. 2009). This is the only galaxy in which we fit three elliptical Gaussians to the emission, rather than the usual two; one for each nucleus, and one for any background/extended emission. We report the flux of each nucleus separately in Table 2.

A.1.2. *NGC 7552 – An AGN with a Starburst Ring*

This (possibly dormant) AGN is located at the center of a bright starburst ring (Forbes et al. 1994). To avoid fitting starburst regions rather than the AGN, we limit the fit to within the central 1" of the galaxy.

A.1.3. *Faint Sources*

There were 13 sources which are marginal detections with our two-Gaussian approach, but which are clear detections "by-eye." To reduce the number of free parameters and increase the flux significance of the results, we fit the following with only one Gaussian. The FWHM of this Gaussian is set equal to that of the PSF calibrator closest in time, as in the two-Gaussian case. The AGN: 3C321, 3C327, 3C424, ESO 323-32, M87, NGC 63, NGC 986, NGC 3660, NGC 4038/9, NGC 5427, PKS 1814-63, UGC 2369 S, Z 41-20.

B. CALIBRATION STRATEGY

As we took many of these sources from archival programs with various setups, we had to define a consistent calibration strategy. While most of the calibrators chosen have L magnitudes in the catalog of van der Bliek et al. (1996), many do not have M magnitudes, and none have M_{nb}. We therefore first make the assumption that $M - M_{nb} = 0$. Secondly, we investigate the relationships between the L–M_{nb} color, Lmagnitude, and spectral type of the calibrator, shown in Fig 10 . We find that for stars of type O, B, A, and F the color L–$M_{nb} \approx 0$ with very little scatter ($\sigma_{L-M} \lesssim 0.05$). This results in the calibration strategy below:

function CALIBRATE TARGETS
  for each *targ* observation **do**
    for each *band* $\in$ [L, M_{nb}] **do**
      1) Find the calibrator (*calib*) observed closest in time which
        a) was observed within 6hrs of the target
        b) (has both L' and M band catalog values) $\vee$ (is spectral type $\in$ [O, B, A, F])
      2) Read $F_{calib,real}$ from *band* or calculate from $\neg$*band* if necessary
      3) Compute $F_{\rm targ,cal} = F_{\rm targ,raw}/F_{\rm calib,raw} \times F_{calib,real}$
      4) Compute the error from the relative errors on the individual fits
    end for
  end for
end function

where catalog values refers to the NIR catalog of ESO calibrators from van der Bliek et al. (1996); and $F_{\rm targ,raw}$ and $F_{\rm calib,raw}$ are the fitted integrated fluxes in counts for the target and calibrator, respectively. Finally, we list each target and its calibrator in Table A.1.

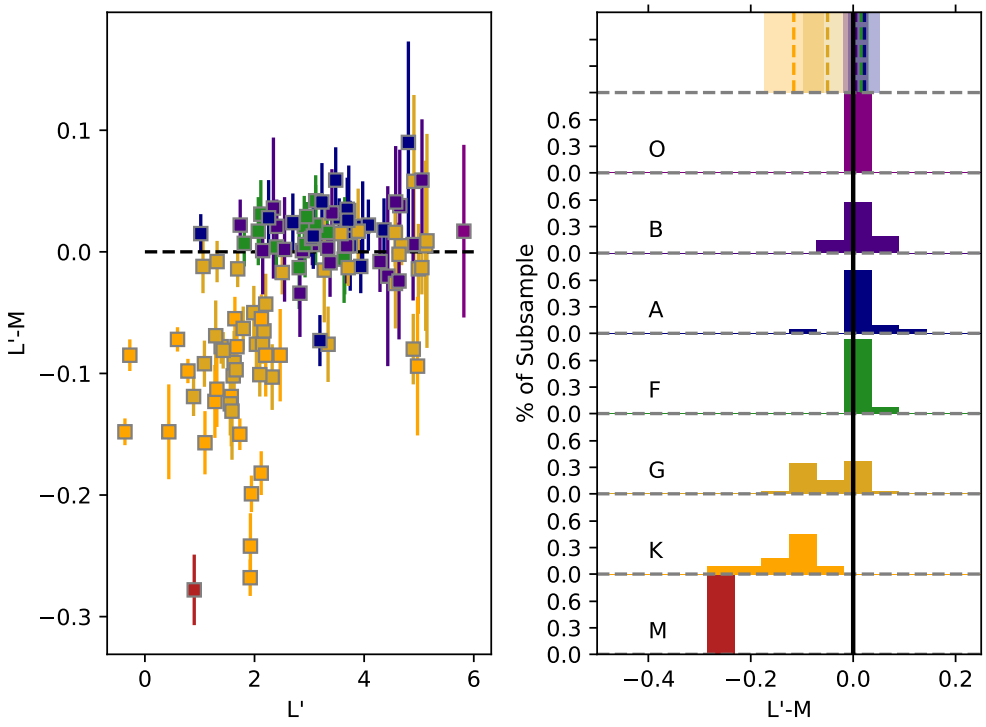

Figure 10. The L-M colors for all calibration stars in van der Bliek et al. (1996), separated by spectral type. For stars of type earlier than G, we find that L-M$\approx$ 0. Bins are spaced every 0.05 mag.

C. SOURCE CUTOUTS

Here we present the cutouts of all sources included in this work in each band. We present each image with "slices" across the image to show the quality of the model fits.

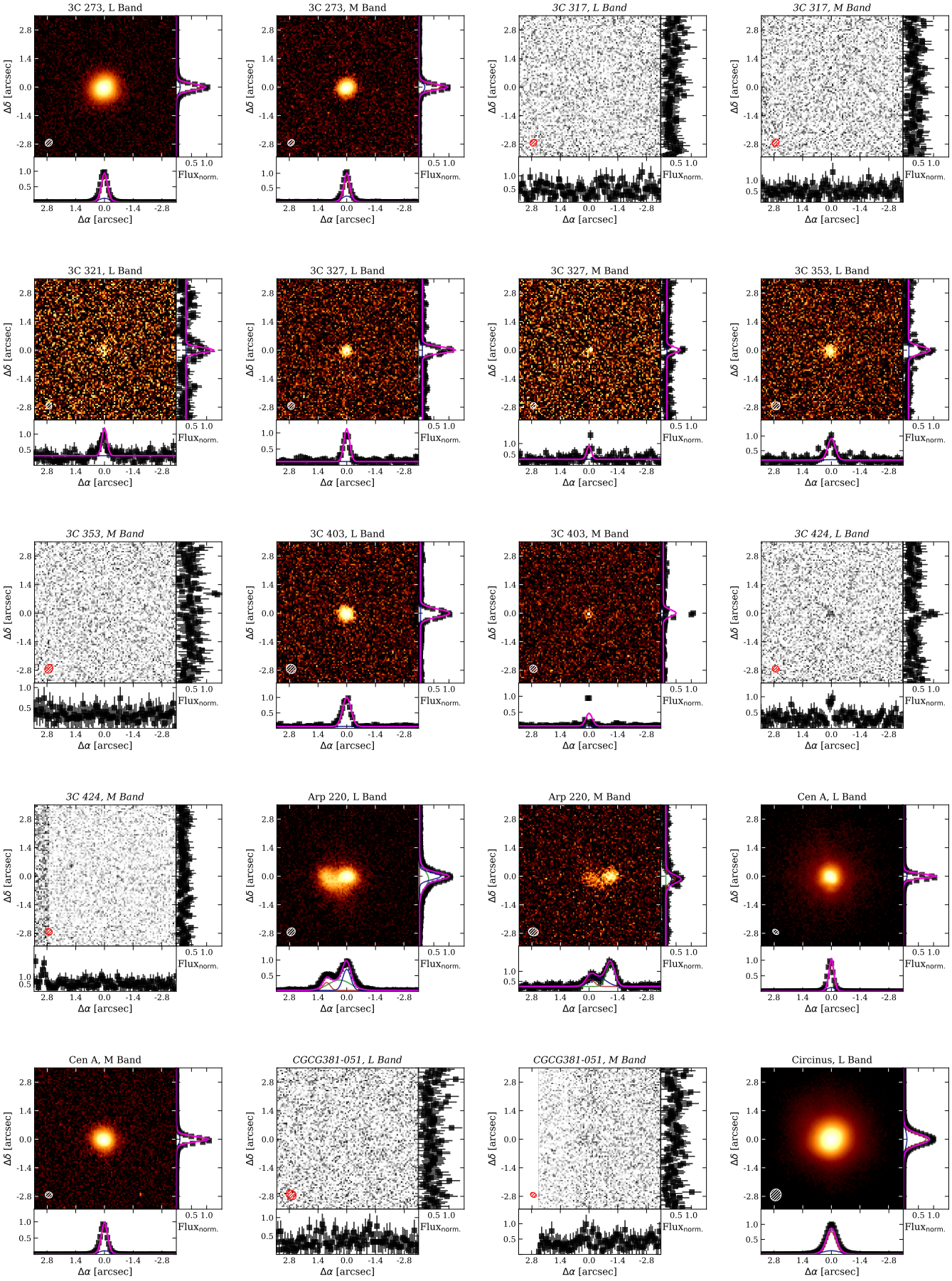

Figure 11. As Fig 3 but for all sources.

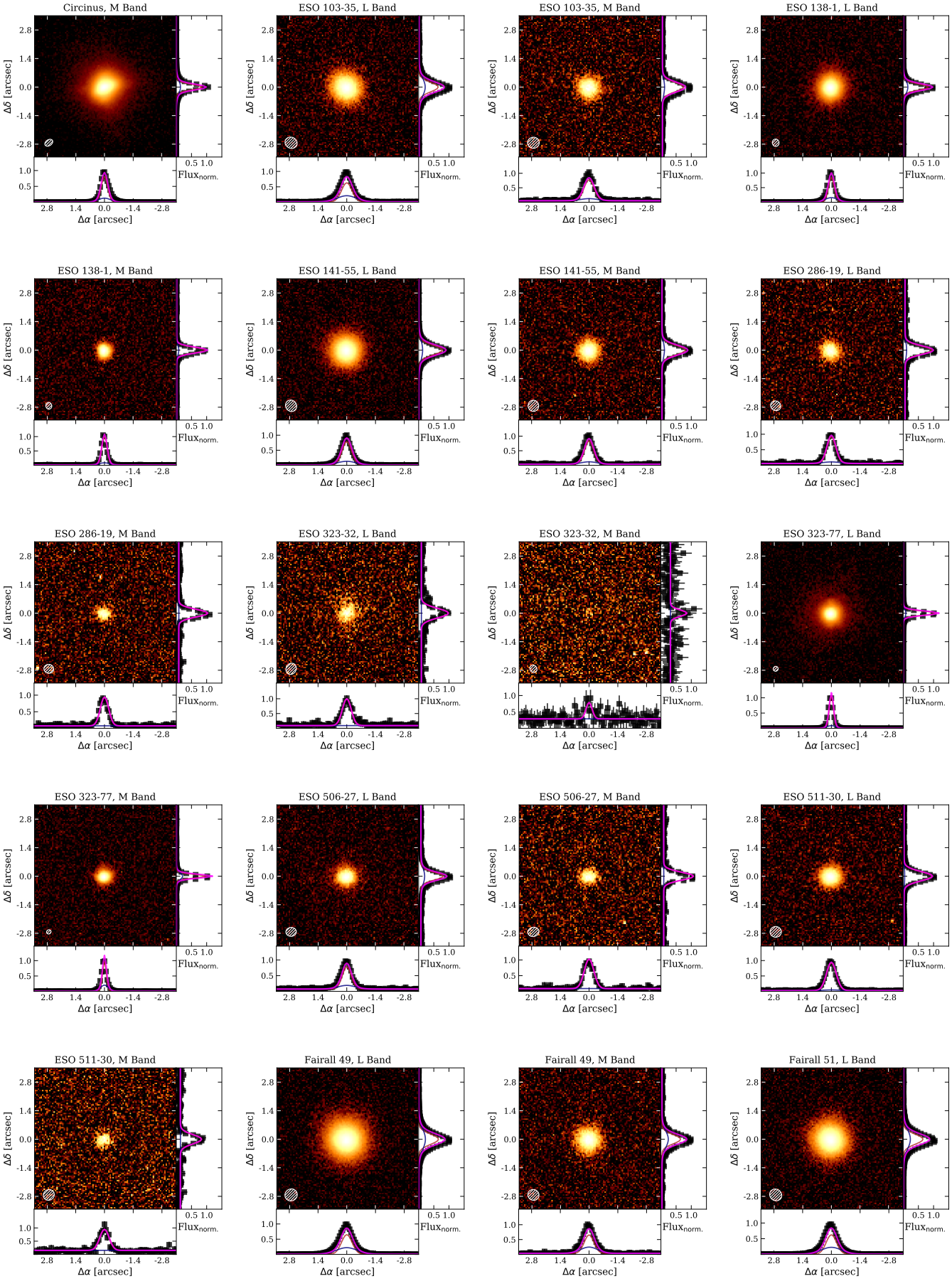

Figure 12. As Fig. 3.

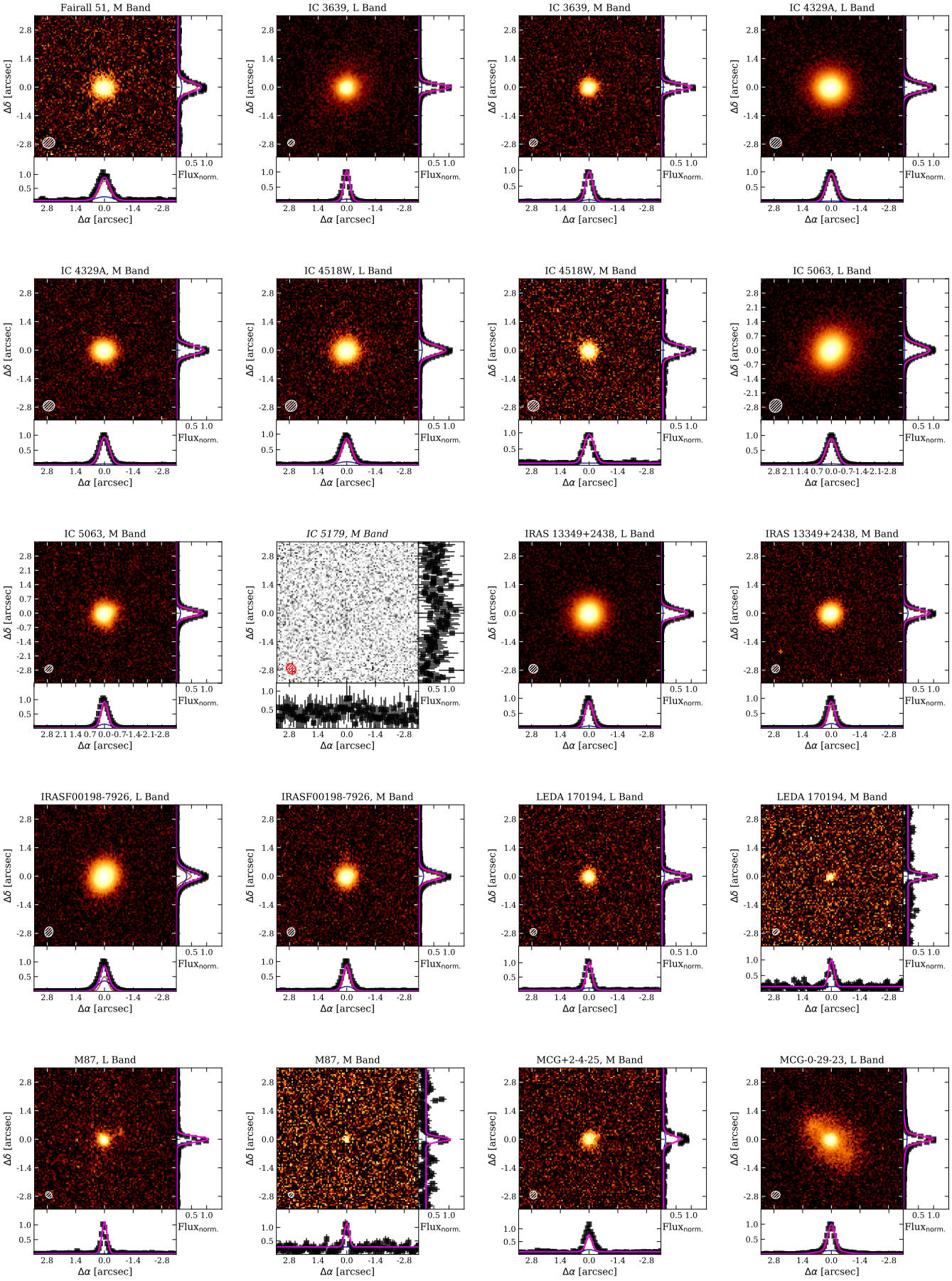

Figure 13. As Fig. 3.

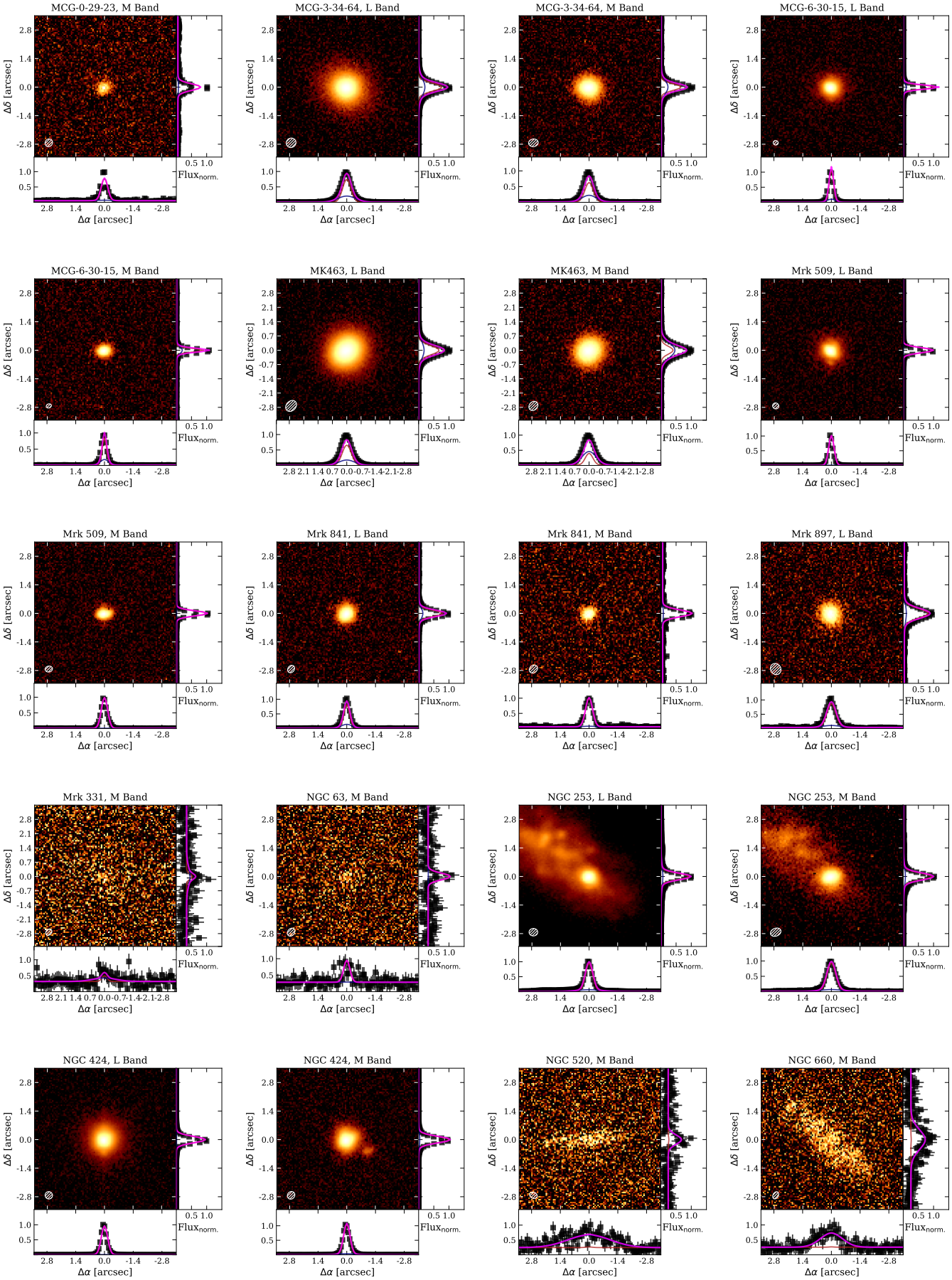

Figure 14. As Fig. 3.

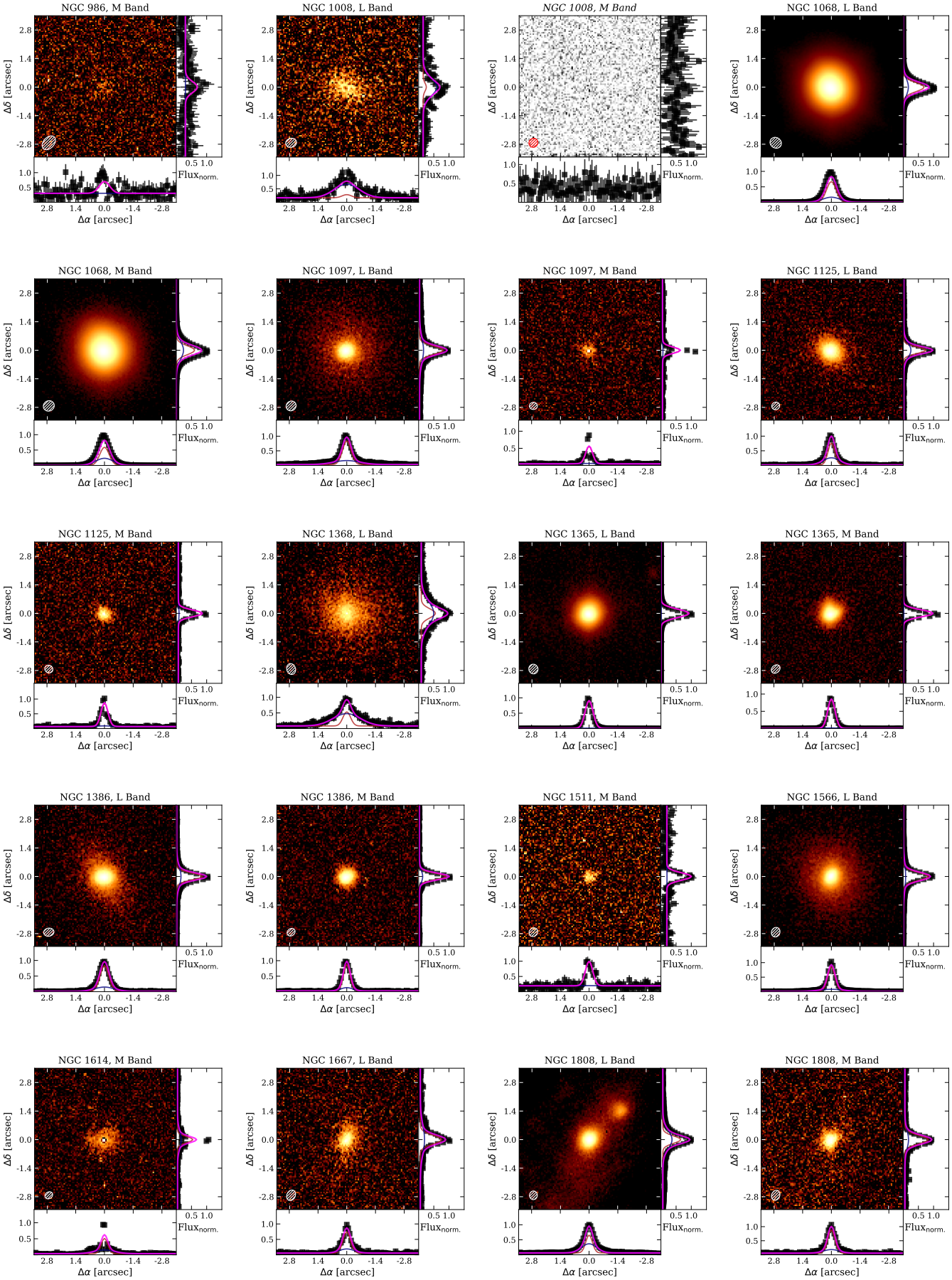

Figure 15. As Fig. 3.

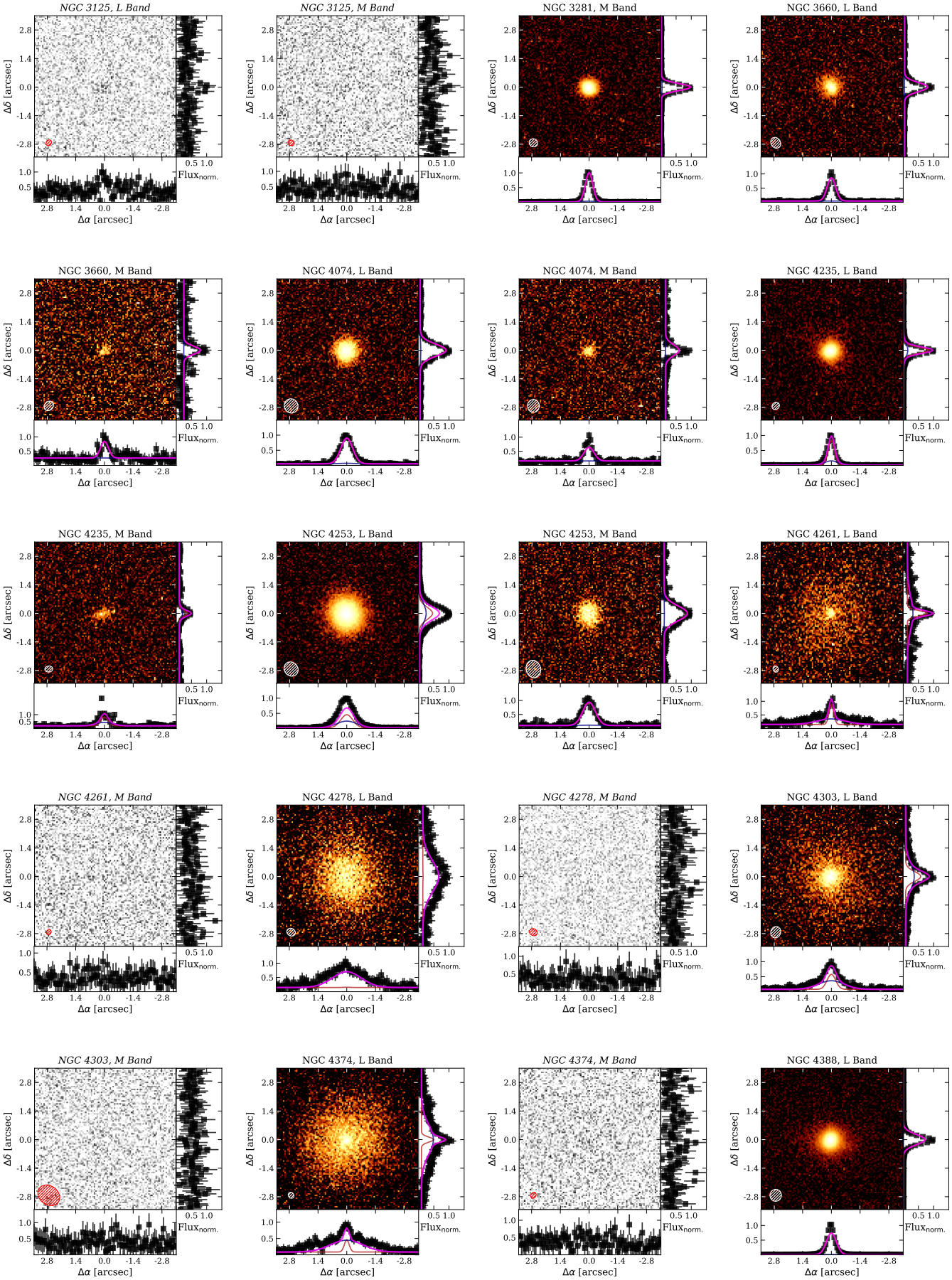

Figure 16. As Fig. 3.

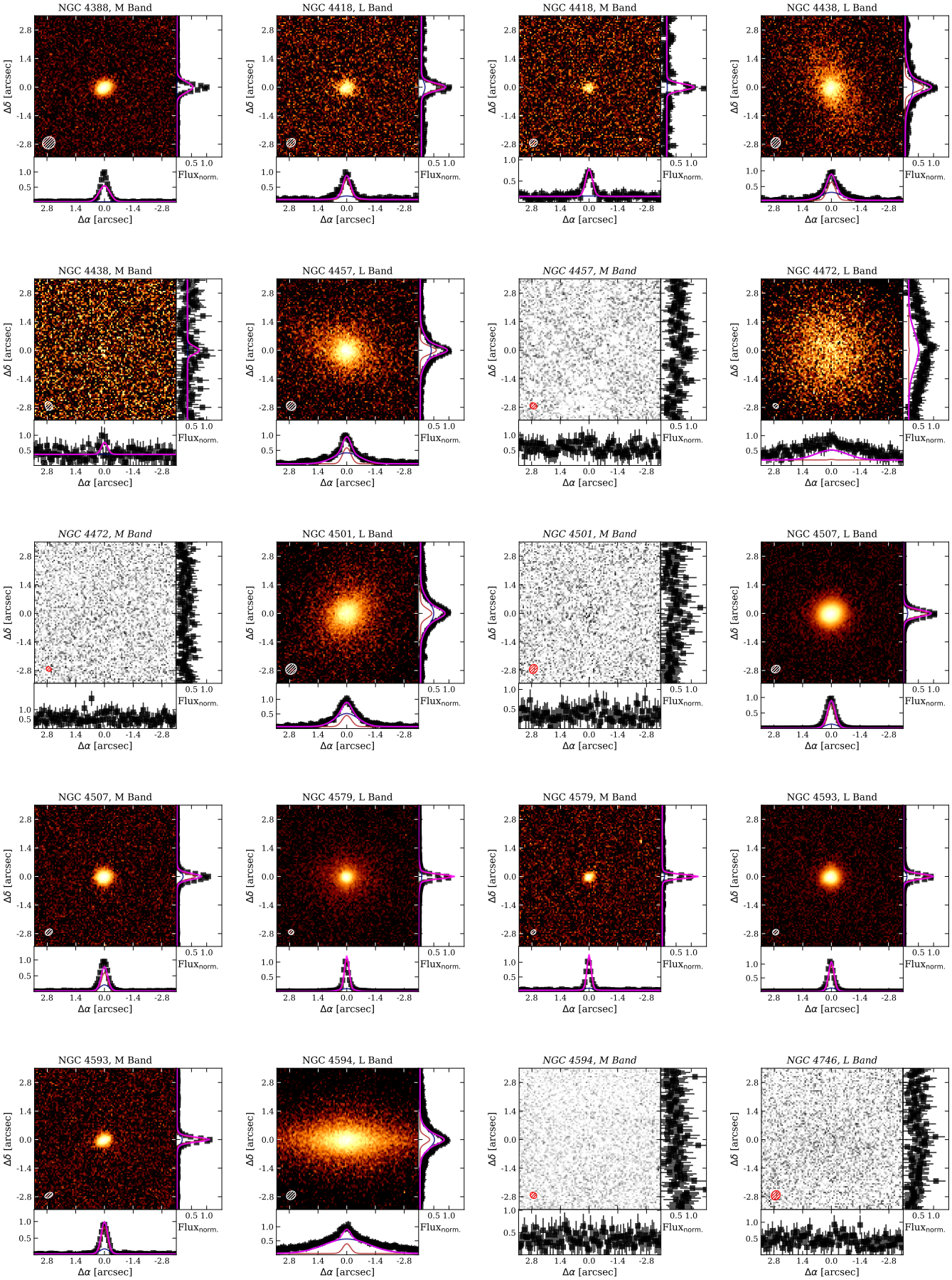

Figure 17. As Fig. 3.

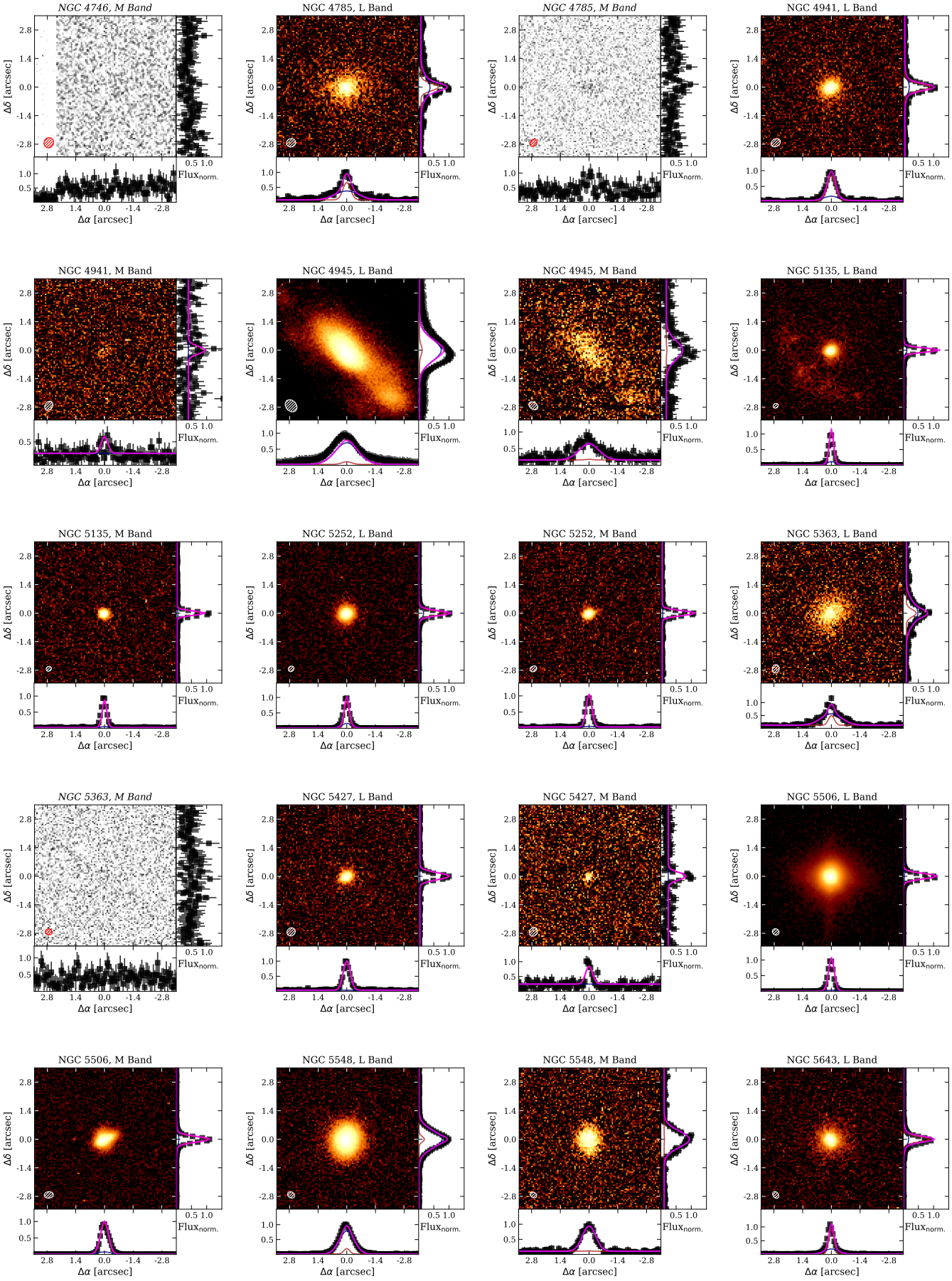

Figure 18. As Fig. 3.

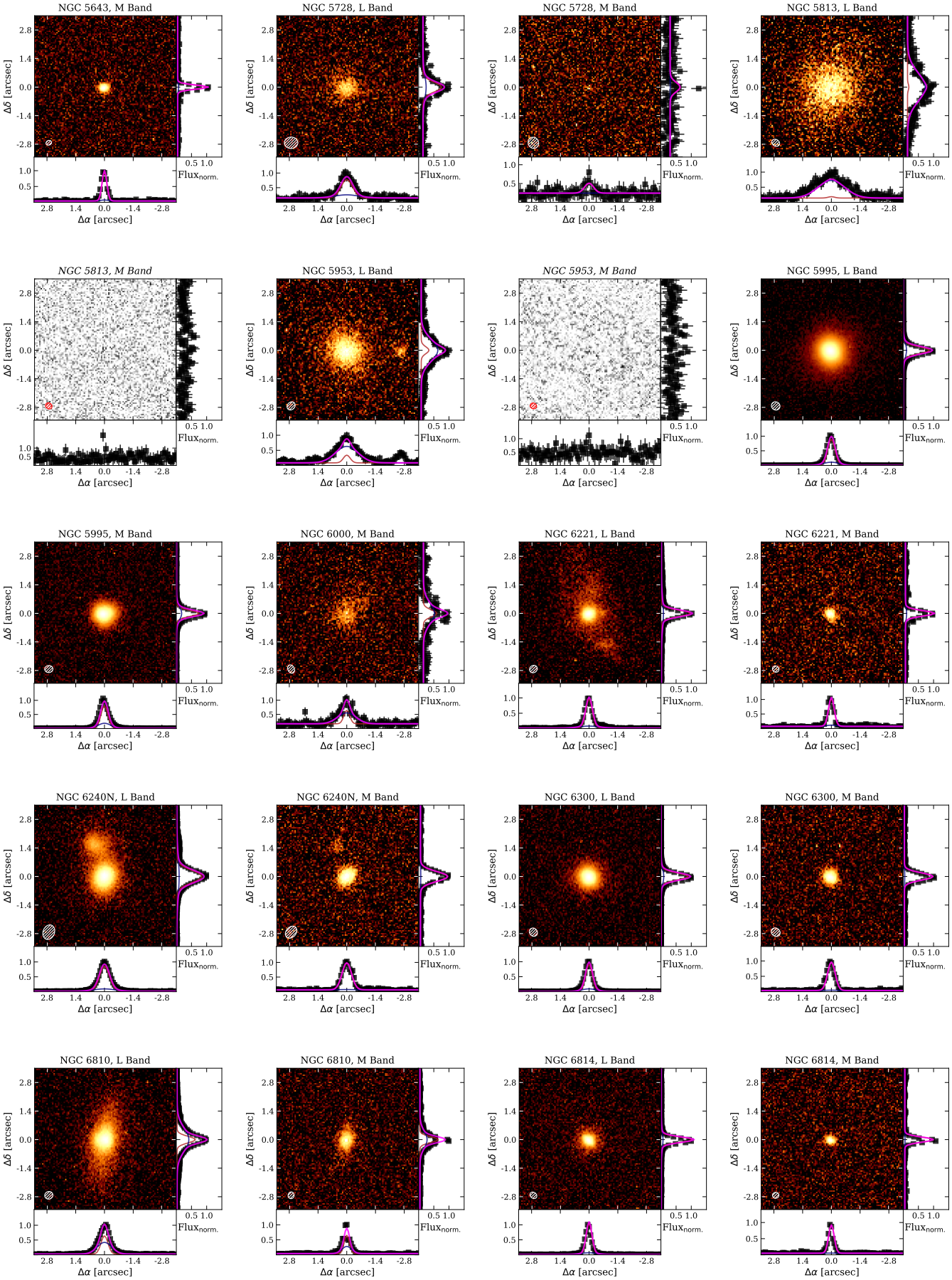

Figure 19. As Fig. 3.

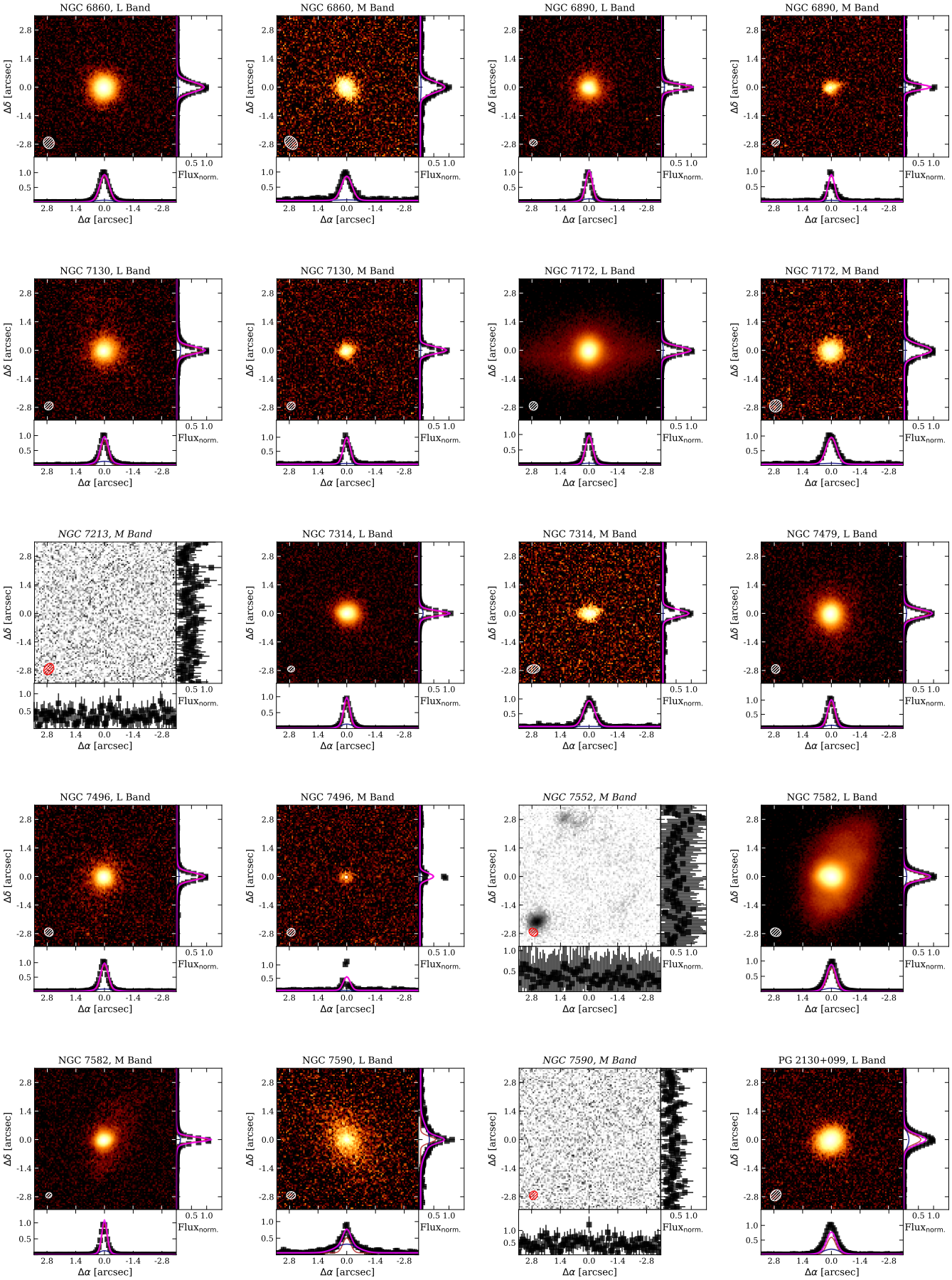

Figure 20. As Fig. 3.

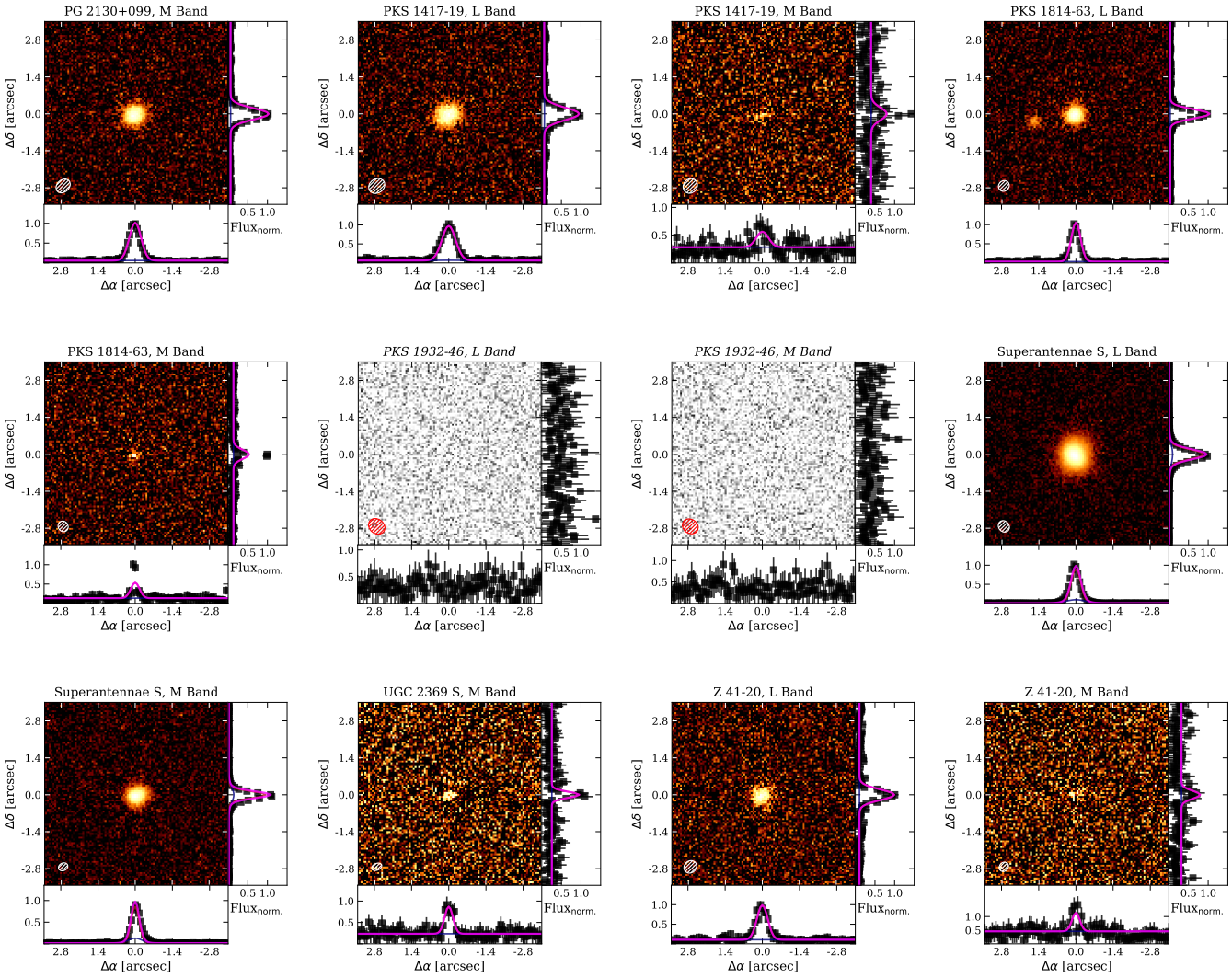

Figure 21. As Fig. 3.